ALMA MATER STUDIORUM · UNIVERSITÀ DI BOLOGNA

Scuola di Scienze
Corso di Laurea Magistrale in Fisica del Sistema Terra

Analysis of airborne measurements from paragliders to detect thermal structures in the mountain atmospheric boundary layer

Relatrice:
Prof.ssa Silvana Di Sabatino

Presentata da:
Arianna Coppola

Correlatori:
Prof. Dino Zardi
Dott. Mattia Marchio
Dott. Francesco Barbano

Sessione IV
Anno Accademico 2019/2020

Abstract

A field campaign was conducted in September 2019 on Monte Avena, south-eastern Italian Alps, to assess the feasibility and quality of an innovative measurement technique for the study of thermal structures in the atmospheric boundary layer over mountains. Paragliders were equipped with non-conventional instruments for airborne measurements of meteorological variables, such as air temperature, relative humidity, atmospheric pressure, and wind intensity and direction. The work aims at testing to what extent the instrumented paraglider can represent a valid method for acquiring physical information on thermal structures.

The paraglider presents a combination of properties that make it extremely useful for the detection of thermals, compared to other flying vehicles adopted for airborne measurements such as aeroplanes and gliders. A new method for identifying thermals, based on the engine-free property of the paraglider, is proposed and the results suggest its reliability.

Measurements have been analysed by means of vertical profiles and horizontal and vertical maps of temperature, virtual potential temperature, water vapour mixing ratio and vertical wind speed. Agreement was found between in-flight measurements and data from soundings and local surface weather stations. Even though the adopted instruments have shown several issues in measuring the atmospheric variables, the new method of collecting atmospheric data by means of an instrumented paraglider has turned out to be promising, both for the identification and characterisation of thermal structures in the mountain boundary layer, and for the study of the basic state of the atmosphere.

Sommario

Una campagna di misura è stata condotta nel settembre 2019 sul Monte Avena (Alpi italiane sud-orientali), per valutare la fattibilità e la qualità di una nuova tecnica di misurazione per lo studio delle strutture termiche nello strato limite atmosferico in ambiente montano con strumenti non convenzionali. Tre coppie di strumenti di volo, normalmente utilizzati nelle competizioni e prestati da un'azienda italiana (Compass Srl), sono state installate a bordo di altrettanti parapendii. Durante sette giornate tra il 17 e il 30 settembre, sono state condotte misurazioni in volo di variabili meteorologiche come temperatura dell'aria, umidità relativa, pressione atmosferica e intensità e direzione del vento.

L'obiettivo del lavoro è testare in che misura il parapendio, così equipaggiato, possa rappresentare un metodo valido per acquisire informazioni fisiche sulle strutture termiche in atmosfera.

Il parapendio è un velivolo senza motore, impiegato per il cosiddetto *volo libero*, che presenta una combinazione di caratteristiche estremamente funzionali allo studio delle termiche. Infatti esso è naturalmente in grado di rilevare la presenza di strutture convettive in quanto se ne serve per mantenersi in volo: all'interno di una massa d'aria ascendente, la vela viene sollevata ad altitudini più elevate dalla massa d'aria stessa. Se questo guadagno di quota rispetto al suolo viene misurato da un ricevitore GPS o da un sensore di pressione barometrica, la termica può essere localizzata. Diversamente dagli alianti, tuttavia, il parapendio presenta range di velocità e raggi di virata che consentono un'analisi atmosferica a più piccola scala, mentre una maggiore portabilità permette maggiore elasticità logistica. Nel lavoro viene quindi proposto un nuovo metodo per identificare le termiche da misurazioni in parapendio. L'analisi dei primi risultati a disposizione fornisce indicazioni promettenti riguardo alla rappresentatività e all'affidabilità delle misure.

Il Capitolo 1 introduce i concetti fondamentali sulle strutture termiche e le tecniche di misurazione precedentemente adottate.

Nel Capitolo 2 vengono descritti i dettagli sulla campagna di misure e sulla metodologia, insieme ad una descrizione dei voli effettuati e delle condizioni sinottiche presenti nei giorni di misura. Vengono messe in luce le caratteristiche necessarie per scegliere un luogo di misura ed un setup strumentale che soddisfino le esigenze di

misurazione delle variabili atmosferiche e le peculiarità della tecnica del parapendio.

Nel Capitolo 3 viene presentata l'elaborazione dei dati acquisiti dagli strumenti e vengono discussi le caratteristiche positive e gli svantaggi degli stessi. Gli strumenti non convenzionali adottati hanno mostrato diverse problematiche nel misurare correttamente le variabili atmosferiche, sia in termini di valori attesi, sia di elevato tempo di aggiustamento dopo il decollo e di problemi di calibrazione. Tuttavia, una spiegazione o una soluzione è stata proposta per ciascuno dei problemi. La risoluzione degli strumenti e la loro sensibilità nel misurare piccole oscillazioni delle grandezze misurate suggeriscono che una volta risolti i problemi di cui sopra, gli strumenti potrebbero rappresentare una valida scelta per misure raccolte in volo da parapendio.

Il Capitolo 4 descrive il metodo adottato per localizzare le strutture termiche. Vengono identificate 10 "sezioni termiche", di cui viene presentata un'analisi introduttiva. Le misurazioni sono state analizzate mediante profili verticali e mappe orizzontali e verticali di temperatura, temperatura potenziale virtuale, rapporto di mescolamento del vapore acqueo e componente verticale del vento. C'è un buon accordo tra le misure in volo e i dati provenienti da radiosondaggi, lanciati dagli aeroporti di Milano Linate e Udine Rivolto, e dalle tre stazioni meteorologiche a terra più vicine al sito di misura.

Il nuovo metodo di raccolta di dati atmosferici mediante un parapendio strumentato si è rivelato promettente in base ai risultati ottenuti, sia per l'identificazione e la caratterizzazione delle strutture termiche nello strato limite montano, sia per lo studio dello stato di base dell'atmosfera. Utilizzi futuri potranno riguardare campagne di misura dedicate, dove si potrà aumentare il numero di voli effettuati e di velivoli contemporaneamente in volo, oppure ricognizioni preliminari che sfruttino l'elevata mobilità del mezzo, per individuare le zone e le condizioni ideali dove utilizzare successivamente strumenti convenzionali di più impegnativa e stabile installazione.

Contents

4

Introduction

The purpose of this thesis is the evaluation of a novel airborne technique to measure atmospheric data in the atmospheric boundary layer over mountains, i.e. a paraglider equipped with instruments for the measurement of meteorological variables such as air temperature, relative humidity, atmospheric pressure, and wind intensity and direction. In particular, the thesis aims at testing to what extent the instrumented paraglider is a valid method for acquiring physical information on thermal structures that develop in the convective boundary layer over complex terrain.

The paraglider belongs to a class of not engine-powered flying vehicles, usually referred to as *free flight* vehicles. This characteristic is one of the properties that can make the paraglider extremely useful for the study of thermals. Indeed, it can naturally probe the presence of convective structures: inside an ascending air mass, it is lifted to higher altitudes by the air mass itself. If this ascent above ground is measured by a GPS receiver, or a barometric pressure sensor, the thermal can be potentially localized. To stay inside a thermal, pilots follow spiralling trajectories, and can keep a radius of curvature smaller than that required by all the other free flight vehicles. This makes the paraglider unique to probe the narrowest thermals.

An instrumented paraglider has several further advantages for the collection of airborne measurements in comparison with flying vehicles sometimes used at this scope. It is a foot-launched and easily portable vehicle (it can be folded in a backpack), which can simplify the organisation of a possible field campaign. Take-off is performed from a mountain hillside, thus atmospheric variables can be measured directly from the take-off, and there is no need for an airport. On the other hand, the proper take-off site and mountain hillside have to be accurately chosen to allow a safe flight. The paraglider usually flies at rather low speeds with respect to air (between approximately $7\,\mathrm{m\,s^{-1}}$ and $14\,\mathrm{m\,s^{-1}}$), allowing a slower sampling of meteorological variables if compared to faster vehicles. Also, it can approach the slope at shorter distance (even a few metres), which can be useful to probe the lower surface layer.

A field campaign involving 11 paraglider pilots was conducted during September

2019 on Monte Avena, south-eastern Italian Alps, to assess the feasibility and quality of this measurement technique.

The harness of each paraglider was equipped with a pair of non-conventional instruments: in order to satisfy basic requirements, such as portability and lightness, specifically designed flight instruments were adopted.

Chapter 1 introduces the fundamental concepts about thermal structures and previous airborne measurements techniques.

In Chapter 2 the details on the field campaign and the methods are described, along with a description of the flights performed.

Data acquired by the instruments and the post-processing techniques applied to them are presented in Chapter 3, where advantages and drawbacks of the instruments are also discussed.

Chapter 4 presents the method adopted to localise thermal structures, and an introductory analysis of them is presented.

Chapter 1

State of the art on thermals in the atmosphere

This chapter presents an overview of the literature about thermal structures in the atmospheric boundary layer. The measurements collected by the instrumented paragliders interested the part of the boundary layer including the surface layer and the mixed layer, up to about $1500\,\mathrm{m}$ a.s.l. and $1200\,\mathrm{m}$ above the surface.

In Section 1.1, general properties of thermals are illustrated. Some methods commonly adopted for the identification of updraft from airborne measurements are presented in Section 1.2, while different classifications of thermals are described in Section 1.3. Section 1.4 presents two example of works related to the fine structure of thermals and to wind drift computations, that could be useful as further development of the thesis.

1.1   General properties of thermals

Within the atmospheric boundary layer, thermals can be defined as parcels or plumes of rising buoyant air in the convective mixed layer, that develop above a surface considerably warmer than the overlying air (Lenschow and Stephens, 1980; Stull, 1988). A more restricted definition is provided in Turner (1973), referring to thermals as "isolated volumes of buoyant fluid which lose their connection with the surface as they rise".

Thermals are able to transport heat, momentum, moisture and turbulent kinetic energy from the surface to upper levels and are the main cause of turbulent mixing in the convective mixed layer (Lenschow and Stephens, 1980).

Over horizontal terrain, the vertical extent of a thermal is roughly equal to the mixed layer depth (Stull, 1988), while the horizontal scale of the convective circulation, including both the thermal updraft and associated downdraft (see below),
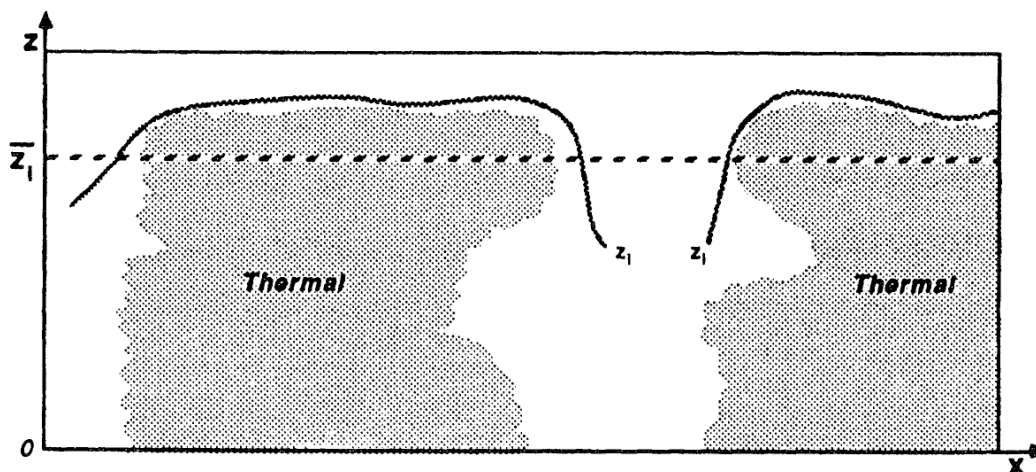
Figure 1.1: Idealized vertical cross section showing thermals. The local and average mixed layer tops are z_i and $\overline{z_i}$, respectively (Stull, 1988).

is approximately 1.5 times the mixed layer depth z_i (Caughey and Palmer, 1979). Thermals' diameter, instead, usually varies according to the time of day, from about $50\,\text{m}$ in the early morning, when convection has just started, to the order of $1000\,\text{m}$ by late afternoon, when convection is fully developed (Stull, 1988). Figure 1.1 conceptually depicts vertical cross sections of the mixed layer showing thermals.

Surrounding the updraft of a thermal plume, environmental air has usually negative vertical velocities: the mixed layer tipically comprises a limited number of thermal updrafts and a large number of interthermal downdrafts (Stull, 1988), as shown in Figure 1.2. The convective circulation also comprises zones of horizontal convergence under thermals, and divergence above. The time scale of the process is of the order of the ratio between the mixed layer depth z_i and the convective velocity scale w_*, approximately between $5\,\text{min}$ and $15\,\text{min}$ (Stull, 1988; Young, 1988).

Common updraft velocities range between $1\,\text{m}\,\text{s}^{-1}$ and $2\,\text{m}\,\text{s}^{-1}$, while stronger updrafts can reach $5\,\text{m}\,\text{s}^{-1}$ or more (Stull, 1988). Downdrafts are generally weaker, reaching vertical velocities of $-2\,\text{m}\,\text{s}^{-1}$.

Thermals generally originate from the differential solar heating of the ground, that presents regions warmer than others (for example, cemented areas with respect to vegetated surfaces). This makes the mass of air above more heated regions warmer itself, thus increasing its internal instability and acquiring buoyancy (Oke, 1987). When "hot spots" exist on land surfaces, thermals predominantly form there, but they can form also over ocean in the abscence of hot spots (Smolarkiewicz and Clark, 1985). Thermals developed over moist and vegetated surfaces are often moister than their environment, and usually more turbulent (Stull, 1988).
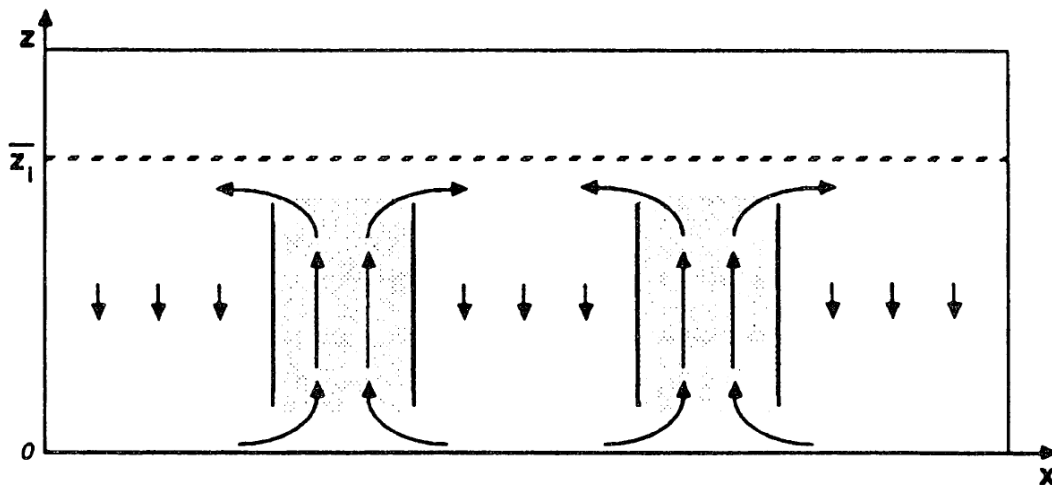
9

Figure 1.2: Exaggerated idealization showing thermals with strong updrafts covering a relatively small fraction of the area, with weak downdrafts in between (Stull, 1988).

Once the air parcel has acquired enough energy, it starts detaching from the surface and rising into the boundary layer, forming a thermal structure. Along its ascent, the thermal diameter increases with the height (Stull, 1988), as a result of entrainment of colder environmental air that is mixed horizontally into it: this type of entrainment, that occurs at the lateral boundaries of thermals, is often referred to as *intromission* (Crum et al., 1987). In addition to increasing the structure dimensions, intromission also decelerates the rise of the thermal as the buoyancy force is decreased by colder air from outside.

While the intromission zone has varying thickness, so that the edges of the thermal are not well defined, the center of the thermal is instead a relatively undiluted core (Stull, 1988).

There are different views about the shape of thermals: for example, Oke (1987) describes them as buoyant bubbles, while Stull (1988) depicts them as finite lenght columns persisting for some time, that can be twisted by wind, meandering horizontally and bifurcating and merging as they rise. They have an intrinsically anisotropic nature, with most of their energy in the vertical (Stull, 1988).

Thermals are trapped within the mixed layer: once the thermal plume reaches the top of the mixed layer and rises into the statically stable air of the entrainment zone, it becomes negatively buoyant. The thermal plume thus decelerates and eventually sinks back down into the mixed layer (Stull, 1988). This process is sometimes called *penetrative convection* (Deardorff et al., 1969; Scorer, 1957; Stull, 1973) and causes entrainment of free atmosphere air into the mixed layer and further mixing with surrounding air, resulting in the growth of the mixed layer thickness (Stull, 1988).

Even though the above description gives general information on thermals, they are extremely variable phenomena and depend on many factors in addition to the existence of hot spots on the ground: their recent history, their position with respect to adjacent thermals, the wind profile, the surface degree of roughness and its topography (Williams and Hacker, 1992).

Different techniques have been used in past years to measure and study thermals. Direct measurements have been collected by means of instrumented aircraft or gliders (Crum et al., 1987; Lenschow and Stephens, 1980; Oney and Aslan, 1987), tethered balloons and meteorological towers (Grossman, 1984; Khalsa and Greenhut, 1985), and visual observations of flight pattern of sea gulls (Woodcock, 1940, 1975). Remote sensing data by lidar (Hooper and Eloranta, 1985) and Doppler sodars (Taconet and Weill, 1983) have also been analysed.

Some recent studies focus on providing statistics on probable hot spots for the formation of thermals, based on data extracted from online repositories of gliders and paragliders flights tracks (Sigrist, 2006; von Kaenel et al., 2011), but they mainly aim at creating thermal probability maps rather than investigating their physical properties.

Many laboratory studies and numerical simulations were carried out mainly regarding anabatic upslope flows, as Hocut et al. (2015); Hunt et al. (2003); Schumann (1990); Serafin and Zardi (2010).

1.2 Identification of thermals

A common way to sort experimental data into thermal or non-thermal categories (i.e. the process called *conditional sampling* (Stull, 1988)) is to set a minimum threshold value of temperature or humidity, (Lenschow and Stephens, 1980; Stull, 1988). As a matter of fact, thermals display a temperature and humidity excess with respect to environmental air (Lenschow and Stephens, 1980), and this excess is typically considerably larger than the level of turbulent fluctuations of temperature or humidity within or outside of a thermal (Manton, 1977; Warner and Telford, 1967).

Lenschow and Stephens (1980) choose humidity as thermal indicator as, differently from temperature, it continues to be greater inside a thermal both in the lower part of the boundary layer, and in the upper part: at the top of the mixed layer, the entrainment process usually tends to warm and dry the mixed layer air. While the humidity difference between thermals and the environment is accentuated, the temperature difference is weakened as the downward-moving environmental air, that consists mainly of air from dissipated thermals, can become on average warmer than

thermal air (Arnold, 1976; Stull, 1988). After analysing thermals over the ocean, Lenschow and Stephens (1980) found that above half of the mixed-layer depth, the temperature inside a thermal is less than that of the environment.

The criterion adopted by Lenschow and Stephens (1980) to identify a thermal requires that humidity be equal to or greater than half the standard deviation of humidity itself, calculated from an entire flight section. They warn the reader that the procedure may exclude some actual portions of thermals, especially the lateral edges where entrainment reduces humidity. They found that the humidity excess decreases with height in the surface layer and increases with height in the upper half of the mixed layer, remaining always positive, in contrast to temperature excess.

Williams and Hacker (1992) instead identified as thermal a section with virtual potential temperature exceeding a certain threshold, as it is a direct measurement of buoyancy of air parcels, and select only the parts of the data time series with a positive vertical air velocity.

Vertical velocity and turbulence intensity have also been used as indicators of thermals (Stull, 1988), but their turbulent fluctuations both within and outside of thermals may be larger than the mean thermal updraft velocity (Manton, 1977), thus making updraft velocity and turbulence intensity less useful indicators of a thermal, unless some sort of averaging is adopted (Lenschow and Stephens, 1980).

1.3   Types of thermals

Two main types of thermal structures are distinguished by Williams and Hacker (1992) into surface layer plumes and mixed layer thermals. The former develop in the lowest tenth of the convective boundary layer, which is characterized by a superadiabatic lapse rate and strong wind shear, have horizontal dimensions of the order of 100 m and are transported in the mean wind direction at speeds roughly equal to that of the mean wind at their mid-height (Wilczak and Tillman, 1980). The analysis of measurements collected by a motorglider over Eyre Peninsula (South Australia) suggested Williams and Hacker (1992) that surface layer plumes increase their dimensions with height, have strong entrainment at the sides and upwind of the central updraft, and present a microfront at the upstream side between the warm and slow air from below and the faster and cooler air the plume rises through.

Mixed layer thermals appear in Williams and Hacker (1992) as larger structures than surface layer plumes, containing anyway air originated in the surface layer, and occasionally showing a slow clockwise rotation in the horizontal wind field of the updraft flow and its environment. Both plumes and thermals data show that updraft velocity increases from the lateral sides of the structure to its core (see

Figure 1.3).

Downdraft regions are larger, slower and more uniform structures than thermals, with little exchange of air with thermals themselves, except a small amount of turbulent entrainment at their edges (Williams and Hacker, 1992).
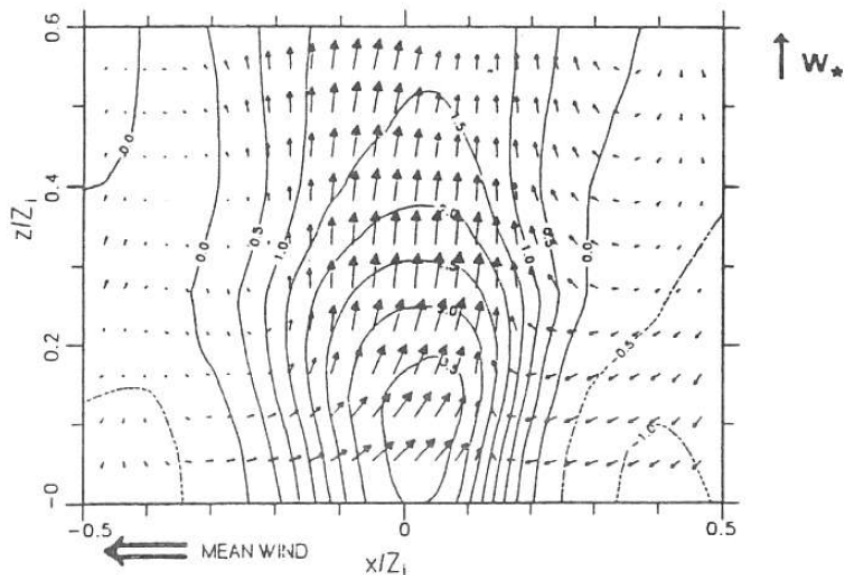

Figure 1.3: Vertical cross-section in the along-wind direction of a mixed-layer thermal. Arrows are wind deviations, i.e. the difference between the actual wind at a given location and the average wind of all the air at that level, scaled with w_*. Contours are θ/θ_*, where θ is the potential temperature deviation and θ_* is the potential temperature scale (Williams and Hacker, 1992).

A different classification of thermal structures is proposed by Konovalov (1970): the analysis of thermal measurements by means of a glider and a light aircraft, conducted around the town of Rapla and the city of Oryol (USSR), resulted in the identification of two types of convective structures. The first is a single-core thermal with vertical velocity of air showing a pronounced maximum and increasing from the periphery to the center (type ⟨b⟩). The second consists in a region comprising several updraft cores with downdrafts in between (type ⟨a⟩). Thermals with two pronounced maxima were occasionally found, and they could be the result of the fusion between two one-core thermals. Structures with horizontal dimensions below 150 m were excluded from the analysis. Type ⟨a⟩ thermals seem to have stronger updrafts, larger dimensions and be more turbulent than type ⟨b⟩ thermals. The frequency of type ⟨a⟩ thermals seems to increase with the absolute value of the air temperature vertical gradient in the lowest 300 m of the atmosphere, while type ⟨b⟩ frequency seems to decrease: the latter seems to represent the original element of convection, while type ⟨a⟩ structure may form from fusion of type ⟨b⟩ thermals when

13

the convective conditions improve.

Figure 1.4 shows the vertical air velocity profiles with respect to horizontal dimensions of the two types of thermals identified by Konovalov (1970). Data are also classified into three classes as proposed by Chernov (1965), depending on the ratio between the maximum thermal diameter l_{max} and the maximum vertical air velocity $U_{y_{max}}$ in the thermal. "Wide thermals" satisfy $l_{max}/U_{y_{max}} \geq 500\,\mathrm{s}$, "narrow thermals" satisfy $l_{max}/U_{y_{max}} \leq 100\,\mathrm{s}$ and "normal thermals" have values in between.

Waibel (2013) proposed a third different model of thermal, the *hat* type thermal, characterized by a flat or even impressed large core with nearly uniform vertical air velocity.
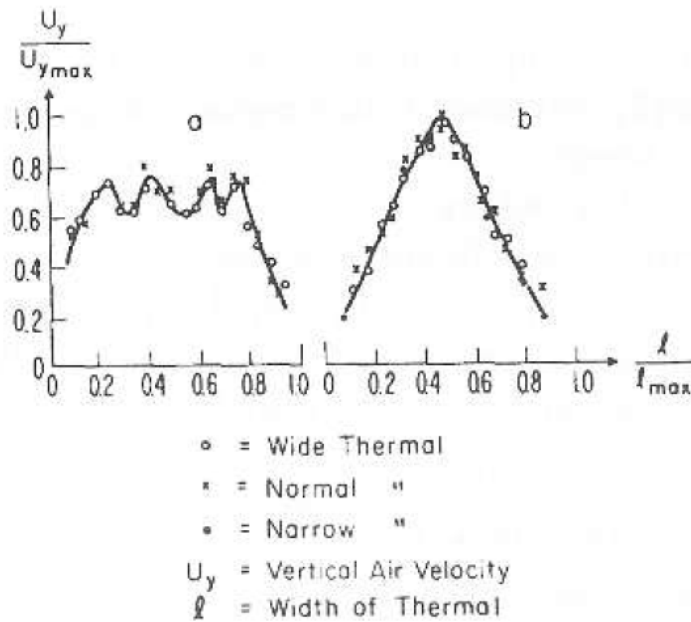
Figure 1.4: Vertical velocity profiles of thermal types ⟨a⟩ and ⟨b⟩, based on 377 flight traverses. Type ⟨a⟩ has multiple, type ⟨b⟩ single, core. (Konovalov, 1970). The classification into wide, normal and narrow thermals follows Chernov (1965).

1.4   Fine structure of thermals and wind drift computation

Ultsch (2012) analysed the fine structure of thermals (i.e. the properties found inside thermals, rather than their differences with respect to downdraft or calm air) investigating the relationship between thermal radius and air vertical velocity by means of measurements collected by gliders, exploiting Global Positioning System

(GPS) data recorded by flight instruments during competitions. He proposed a metholodogy based on wind drift subtraction from spiral trajectories in thermals, that allows to observe the dependence of updraft on the estimated radius of the thermal. In order to probe the region surrounding the thermal core, he exploited measurements from paragliders as well, as they are less affected by increasing sink rate effects due to steep turning angles with respect to gliders.

Wind drift computation was also performed by Allen and Lin (2007), who estimated the mean motion of the centers of open circles that form a typical spiral trajectory followed by an autonomous soaring Unmanned Aerial Vehicles (UAV) in thermals. The wind drift can be considered as a rough estimate of the horizontal wind in thermals.

These two works could represent a useful starting point for further developments of the thesis on the fine structure of thermals, and on the computation of wind drift that generally characterises upslope flows.

Chapter 2

Field campaign

This chapter presents the field campaign carried out at Monte Avena (BL) between 17 and 30 September 2019. In the first part of the chapter, paragliding materials and piloting technique are briefly illustrated, and the reasons for the choice of the location and the instruments are explained. Details on paragliding technique given below will be recalled throughout the thesis. Also, they are necessary to highlight the peculiarities of the measurement method and the several aspects that have to be taken into consideration to plan a field campaign of this type.

The second part of the chapter is devoted to the measurements acquisition method, with a day by day description of the performed flights and of the synoptic meteorological conditions.

2.1 Paragliding

The paraglider wing (Figure 2.1) is a fabric structure composed of two surfaces held together by vertical membranes (Teppa, 2012). The surfaces are sewn together at the rear part of the canopy (*trailing edge*), while the front (*leading edge*) is open to let the airflow enter and inflate the wing. The inflated wing has an arc shape, and the aerofoil, necessary for the flight aerodynamics, is maintained by the vertical partitions (*ribs*) that divide the structure into *cells*, and by large openings in the ribs allowing air passage inside the canopy, between the cells. Lift is generated by the difference of static pressure between the airflow under the bottom surface of the wing and the airflow above the top surface.

The pilot is supported underneath the wing by a network of *suspension lines* that are attached at one end to the bottom surface of the canopy and at the other end to the *risers*. The latter are connected to the pilot's harness by carabiners. Special lines are the brakes, as they are the main mean of control of the paraglider. They are attached to the trailing edge of the wing and end with two handles, located at the sides of the pilot's head, that holds them in hand: by pulling or releasing the
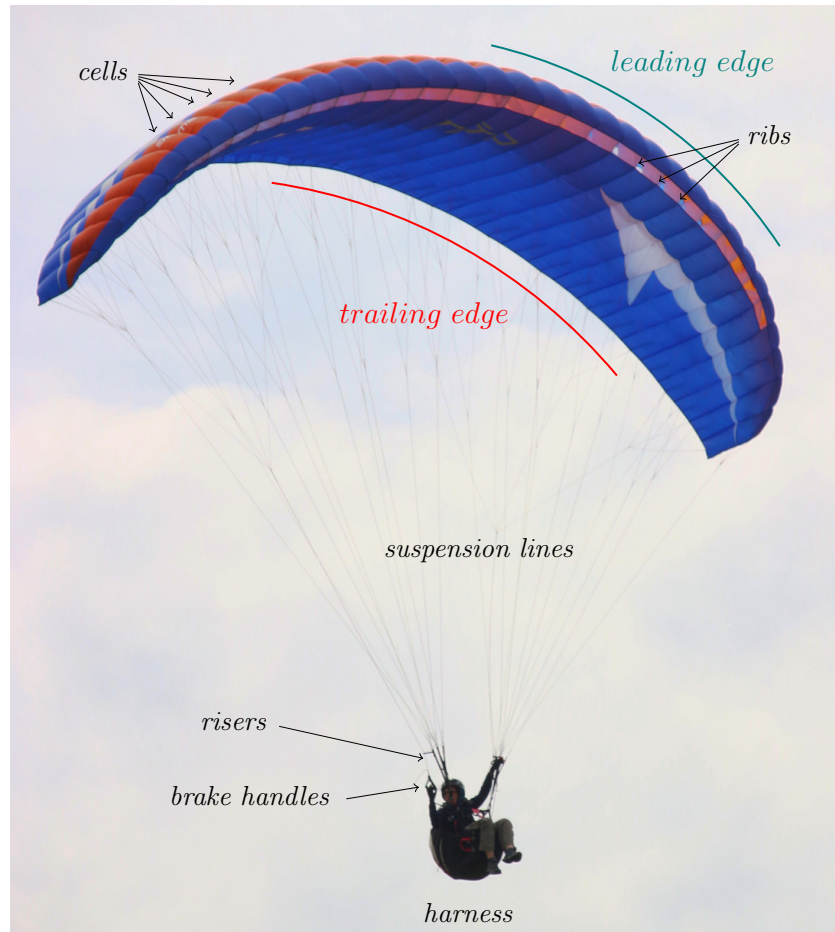
Figure 2.1: The paraglider wing and its main components. The pilot is sitting on an upright harness. (Pilot: Arianna Coppola. Picture by: Giacomo Roversi).
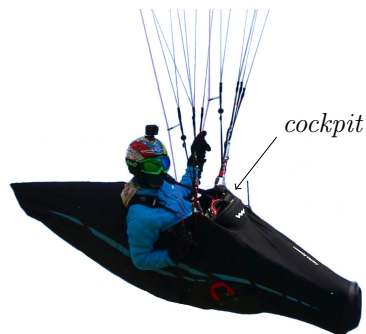

Figure 2.2: Pilot lying in a pod harness. The cockpit, i.e. the slot for instruments, is also indicated. (Pilot: Samuele Carazzai. Picture by: Giacomo Roversi).

handles, the trailing edge profile is modified allowing the wing to change velocity and direction. Also, some manoeuvres are performed by acting on the risers, as well as shifting the pilot's body weight sideways in the harness.

Beginners usually sit on an *upright* harness (Figure 2.1), while experienced pilots usually prefer reclined *pods* (Figure 2.2), that offer more comfort and performance during long flights, keeping the pilot warmer and reducing air drag.

Due to their different shapes, the two types of harness are likely to perturb in a different way the airflow surrounding the pilot and the instruments recording data. The type of harness used by each pilot has been registered within the flight metadata, as its effects on airflow perturbation could be analysed with further investigations, not performed in the present work.

Also, the upwash effect caused by lift generation, that generally affects airborne wind measurements (Crawford et al., 1996; Garman et al., 2008) is not considered here: it affects the wing, while the instruments are located on the harness, some metres below the wing.

The deflated wing can be folded into a bag and easily stored or carried with the harness in a large backpack. Some types of harness can also be turned inside out to become themselves a backpack able to contain the wing. This makes the paraglider an incredibly portable aircraft if compared to other air vehicles, as gliders and aeroplanes, sometimes adopted for airborne measurements.

The paraglider does not have an engine, thus the velocity needed to maintain aerodynamics sustenance (i.e. lift generation) is reached by losing height with respect to air, and this does not require any particular piloting: in calm air, the wing flies itself losing height at a characteristic sink rate that mainly depends on how much the brakes are pulled (see Section 3.3.7 for further details). This flight mode is called *gliding*.

The second main flight mode is *thermalling*: in order to fly for a longer time, pilots can gain height thanks to the rising plumes of buoyant air that are generally called thermals (see Section 1.1). Pilots look for them by means of their experience, the knowledge of the location and its circulation patterns, the help of flight instruments and the observation of cumulus clouds, birds of prey, and other paragliders, hang-gliders or gliders nearby. Once the thermal has been found, the pilot starts a spiralling trajectory to stay inside the rising column of air. Depending on weather conditions and pilot's experience, one can climb hundreds of metres (even above 5000 m a.s.l., depending on the place) prolonging the flight duration. It has to be highlighted that, when flying in a thermal, the wing is still losing height with respect to air (i.e. it has a downward vertical velocity with respect to air) in order to generate the required lift to glide, but at the same it rises with respect to ground

thanks to the ascent of buoyant air mass within which it is flying.

Take-off and landing are very peculiar moments of a paragliding flight, and the modalities they are performed with heavily influence the organization of a field campaign for collecting airborne measurements from paragliders, including the choice of a suitable location, described in Section 2.2.

Take-off is generally performed at the top or on a side of a mountain or hill. A typical take-off site is a grassy meadow on a slight slope, without trees, shrubs or boulders, and large and long enough for the take-off procedures (Teppa, 2012). Usually, a windsock indicating wind direction and intensity is present, as the take-off should be done into a light breeze, since the inflation requires a frontal airflow. The wing is inflated with a few running steps along the slope. Lift is progressively generated on the wing until the pilot takes off.

As for the take-off, a suitable landing area should be large and long enough and without close obstacles that could potentially put the pilot in danger (e.g. transmission lines). The landing is done again into the wind, in order to slow down the wing, and the presence of a windsock is even more important than at take-off, since the pilot should know the wind direction and intensity from high above the ground, where its evaluation is more difficult, to plan the correct landing manoeuvres.

2.2   Choice of the location

Monte Avena is a non-isolated mountain topping 1454 m a.s.l., located in the province of Belluno (Veneto, northern Italy). It overlooks the Feltre valley, that separates it from the Monte Grappa massif and the Belluno Prealps. The southernmost range of the Dolomites (Vette Feltrine) rises north of it (see Figure 2.3).

Monte Avena is very much frequented by paragliding pilots, especially since the Paragliding World Championship held there in July 2017, as it is appreciated for the wide range of possibilities it offers for flying.

The main reasons that have guided the choice of Monte Avena as the location for the field campaign are explained below.

Hillside features The mountain has quite uniform, gentle hillside slopes. The eastern side has been evaluated as quasi-ideal, because of its slope (about 20°) and its good exposure to solar radiation in the central hours of the day. Its land cover (grass at the top, forest along the sides) helps to limit non-homogeneity effects in the atmospheric structure of the surface layer, that could derive from more heterogeneous ground, made for example of a mix of bare, rocky
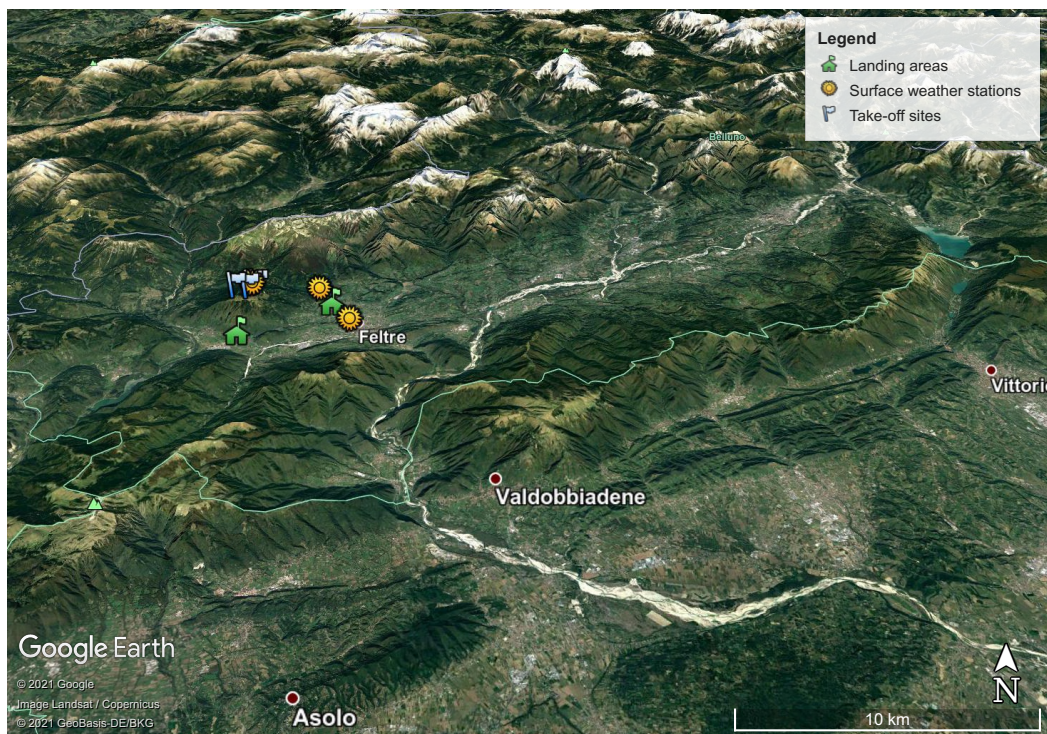
Figure 2.3: Google Earth overview of the location area and its surroundings. Monte Avena is located in the upper-left part of the image and different markers identify the position of take-off and landing sites, as well as the surface weather stations considered for the present work (see also Figure 2.4).

and wooded soils, and could affect upper layers as well.

Easy flight conditions Weather conditions on Monte Avena are generally very good to fly, with weak-moderate winds and moderate development of cumulus clouds, making it possible to fly almost every time of the year. Both weak (usually at the eastern side) and strong (usually at the south-western side) thermals develop according to the particular conditions of the day (generally between 10 am and 4 pm in the spring-summertime), allowing both easy flights with modest height gain and duration, and long "cross-country" flights with considerable thermal activity and distance covered. However, compared with other flight sites located more internally in the Dolomites, very strong convective conditions that require a high level of piloting experience and technique are not likely to occur on Monte Avena, making the place also suitable for the activity of paragliding schools and licence exams.

Many excellent take-offs On the meadows at the top of the mountain three take-offs are present, each oriented in a different direction: respectively towards east, south and west (see Figure 2.4). In addition to the three main ones, two

secondary take-offs are often used by pilots: the first is located just outside Malga Campet, overlooking the east side of the mountain about 50 m above the main east take-off (useful in case of weak wind conditions); the second (called Pra di Mezzo, not used in the field campaign) is a steep meadow located on the eastern side at 1050 m a.s.l. (useful in winter when snow or ice prevent the pilots from reaching the top).

The number and different orientations of the take-offs offer the possibility to choose the best take-off according to the weather conditions on the day of the flight (in particular, the prevailing wind direction is the primary factor as the pilot should take off against the wind – see Section 2.1), thus with a low probability of cancelling the flight due to the lack of suitable take-offs, which could happen in other locations where only one take-off is available. Only a north-facing take-off is missing, but a northerly wind is typically associated on Monte Avena with strong convective conditions that make the flight unsafe.

Also, the three main take-offs are very much appreciated as they are far from the trees, covered by low grass, and slightly sloped towards the valley (see Section 2.1). W and S take-offs are also wide enough to simultaneously unfold a great number of paragliders (up to 50-60 and 100 respectively). All the three take-offs are equipped with a windsock, not always present at other flight sites. S take-off is the most used one, as usually in the central hours of the day the prevailing wind blows from the south (see Section 2.4 for further details). E and W take-offs are mainly used respectively in the early morning and in the late afternoon, according to the development of upslope flows following the Sun's position.

All the take-offs are easily reachable by car and by the shuttle made available by the local flight club (Para&Delta Club Feltre). The journey from the base to the top of Monte Avena takes about 20 min, thus being very convenient if compared with other flight sites reachable only by cable cars or on foot. If necessary, it is also possible to reach one take-off from another on foot along the unpaved level road visible in Figure 2.4. At a short distance from the main take-offs are also two mountain huts (Malga Campet and Malga Campon), useful as rest stops.

Excellent landing areas Two grass lawns in the valley of Feltre are used as official landing areas. The main one is located in the sport area of Boscherai, between the towns of Pedavena and Teven, while the second is placed in the industrial area of Arten (see Figure 2.4). Both the landing areas are wide and level enough to land safely, the grass is cut frequently and more than one windsock show the direction of the wind at ground, that is generally weak-
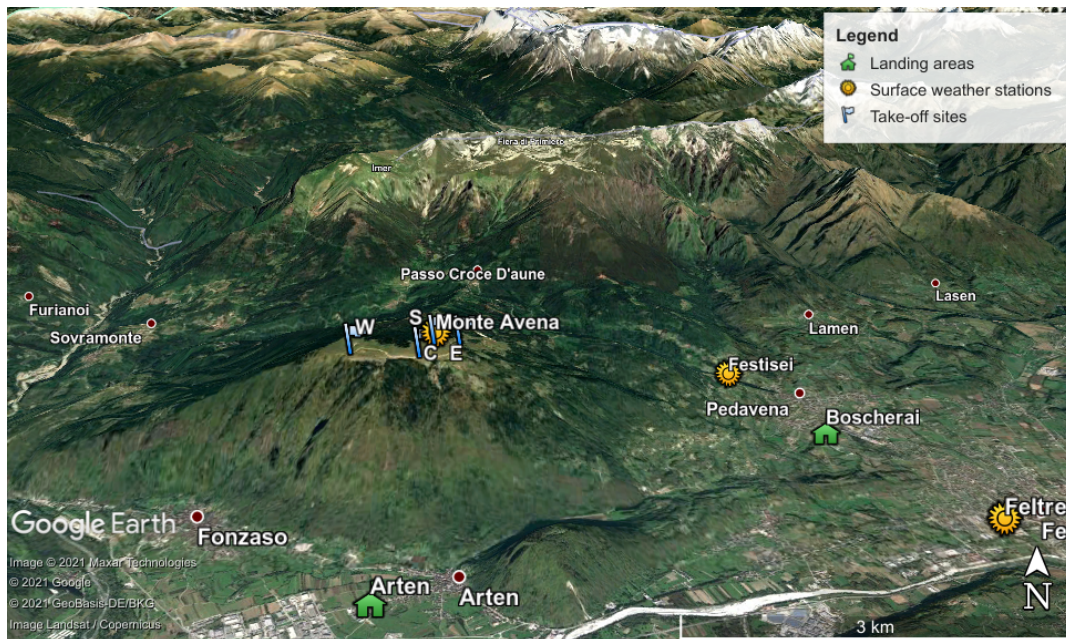
Figure 2.4: Google Earth image of Monte Avena. Blue-flag markers indicate the four take-offs at the top of the mountain (E: east take-off, 1355 m a.s.l., S: south take-off, 1410 m a.s.l., W: west take-off, 1425 m a.s.l., C: Malga Campet take-off, 1405 m a.s.l.). Green-house markers identify the two landing areas (Boscherai, 359 m a.s.l. and Arten, 308 m a.s.l.). Yellow-sun markers indicate the three considered surface weather stations (see Section 2.5).

moderate. The Boscherai landing area is reserved for paragliding pilots only, while landing is forbidden to gliders and hang-gliders. The newly built house of the local flight club is the usual meeting place for pilots before leaving for the take-offs and is a useful rest stop.

Between Boscherai and Arten many meadows and fields can be used as additional landing areas in case of emergency.

Known place and pilots The mountain, its take-offs and landings are very well known to me, as I learned to paraglide attending the Monte Avena flight school and keep flying mainly in this area. I am thus familiar with many pilots and instructors there, making it simple to get in touch for any reason concerning the flight and the coordination of the field campaign.

The eastern side of Monte Baldo (at the boundary between Veneto and Trentino Alto Adige, overlooking Lake Garda on its western side) was the first place considered as the location for the measurements campaign, but it presented many problems related to accessibility and flight logistics. Monte Avena has represented a more suitable location for the advantages explained above.

2.3 Choice of the instruments

The choice of the instruments has been made considering first of all the meteorological variables they are able to measure and that are needed for the study of thermal structures. Also, their weight and portability on board the paraglider, and their cost or the possibility to borrow them have been evaluated. Due to the nature of the measurement technique, instruments that are specifically designed for paragliding, commonly used during recreational flights or competitions, have the major advantage of statisfying the requirements of being small and light, being easy to be secured to the pilot's harness and working in an automatic mode once turned on.

However, a vast spectrum of instruments for flight exists, as they differ in measured quantities, dimensions, cost. A typical flight instrument consists in a Global Navigation Satellite System (GNSS) receiver that tracks the flight trajectory and altitude, combined with a variometer to sense the velocity of vertical movements associated with ascent or descent air flows, and usually a barometric altimeter, a compass, a gyroscope and an accelerometer (Free Aero, 2016). All instruments are provided with a screen showing all the measured quantities, in order to help the pilot interpret the weather conditions; the only exception are acoustic variometers, that only indicate ascent or descent motion only with an acoustic signal. Not all the instruments, however, have the function of storing collected data in memory to analyse them after the flight (usually only GNSS tracks are recorded), while for the field campaign a storing device was obviously needed. Also, a few anemometers are available on the market: consting usually of rotational or pressure anemometers, they can generally be secured to the wing risers or hung from a cable below the pilot (Teppa, 2012).

After examining the instruments available on the market (Free Aero, 2016), C-Pilot EVO and C-Probe produced by Compass Srl were chosen, especially because they are able to record the trajectory and altitude of the flight, together with air temperature and humidity, atmospheric pressure and velocity of the pilot with respect to air. Compass Srl is a small company with its offices in Castelfranco Veneto (TV, Italy), pioneer in designing flight instruments which are currently used by competition pilots. C-Pilot EVO (Figure 2.5a) – hereafter referred to as C-Pilot – is a flight computer that integrates a GPS receiver, a barometer and a variometer, while C-Probe (Figure 2.5b) is a Pitot tube provided with temperature, humidity and pressure sensors, as well as a gyroscope, an accelerometer and a magnetic compass. Two alternative anemometers (produced by Flymaster and by Skytraxx respectively) were considered for wind measurements, but they are equipped only with a temperature sensor and would need an external GPS receiver to combine meteorological with position data. The two Compass instruments, instead, form

an integrated stand-alone couple of measuring devices, thanks to a BlueTooth connection sending data from the probe to the computer. Also, C-Probe integrates a patent-pending automatic calibration system and wind computation algorithm, that takes into account and compensates for effects such as the distorted airflow around the harness and pilot (details on the wind measurement are given in Section 3.3.7). The probe has been tested by Compass Srl at the wind tunnel of Tolosa, belonging to ISAE-SUPAERO (Institut Supérieur de l'Aéronautique et de l'Espace), which has decided to adopt it among its instruments. After a couple of visits to Compass Srl offices to discuss the project, they have gently agreed to borrow three C-Pilot and three C-Probe, that have been used during the field campaign and then returned.

C-Pilot (Figure 2.5a) is a $150\,\mathrm{mm} \times 134\,\mathrm{mm} \times 30\,\mathrm{mm}$ and $539\,\mathrm{g}$ flight computer with a touchscreen display (showing flight data in real time), with a long-life battery (up to about $18\,\mathrm{h}$, definitely longer than a typical flight duration). It integrates a single-frequency, single-constellation Quectel L80 GPS receiver with 22 tracking/66 acquisition channels, supporting Differential GPS (DGPS) and Satellite Based Augmentation Systems (SBAS) functions.
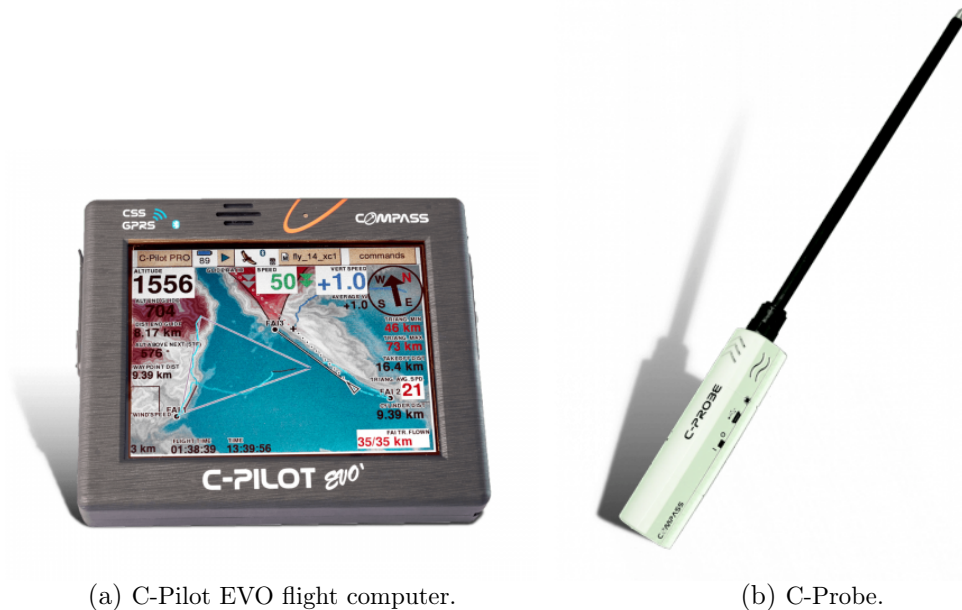
(a) C-Pilot EVO flight computer.   (b) C-Probe.

Figure 2.5: Compass flight instruments chosen for the field campaign. Images source: Compass Srl.

C-Probe (Figure 2.5b) is formed by a $124\,\mathrm{mm} \times 30\,\mathrm{mm} \times 27\,\mathrm{mm}$ white parallelepiped unit containing the temperature and relative humidity sensors with four air intakes, one for each side, as well as a pressure sensor and an inertial measurement unit composed of a three-axis gyroscope, a gyroscope-stabilized magnetic compass,

and a three-axis accelerometer. Joined to the main body is a 271 mm long Pitot tube, with a total pressure port at the tip of the tube and four static pressure ports around the tube, close to the tip. Also C-Probe has a long-life battery (up to 30 h with BlueTooth connection to C-Pilot). Datasheet specifications of the instruments are summarised in Table 2.1.

The couple of instruments can be placed on the harness cockpit, that is the typical slot for instruments, integrated in the pod harnesses or added to upright ones, positioned on the pilot's lap (see Figure 2.2). The instruments can be secured to the cockpit with velcro strips, lines and carabiners. The positioning of C-Probe is fundamental for correct measurements: the air intakes should not be covered – Compass Srl recommends positioning them outside of the cockpit and leaving at least 1.5 cm of empty space around the sides of the white unit – and the tube should be bent to align it to the relative airflow (i.e. along the flight trajectory) with a tolerance of 30°. The bending is possibile thanks to the semi-rigid material of the tube and should not be done between the static ports and the tip.

In addition to Compass instruments, pilots have flown with their personal instruments and data from them have been used for a brief comparison with GPS measurements collected by C-Pilot (see Sections 3.1.2 and 3.1.3).

The field campaign project originally included also the use of a ceilometer, but technical issues after its installation at the Boscherai landing area made it impossible to retrieve its data.

2.4   Method of acquisition and measurements overview

The field campaign was conducted between 17 and 30 September 2019, with a total of seven days effectively spent collecting measurements.

The pilots participated in the project on a voluntary basis. They are instructors of the Monte Avena flight school and experienced pilots of the Para&Delta Club Feltre, as well as the author of the present work herself.

Unsuitable meteorological conditions or unavailability of pilots made it difficult to organise the flight activity on all of the days. During each measurement day, up to three simultaneous flights have been carried out (since three is the number of instruments couples), and on 20 September two groups of flights, one in the morning and one in the afternoon, have been performed. Section 2.6 describes the flights on each day.

The flight schedule was agreed before each flight: pilots were asked to fly over the mountain slope, following S-shaped trajectories with long straight segments con-

Variable Sensor manufacturer, model	Datasheet specifications
Position measurements (C-Pilot EVO)	
Latitude and Longitude Quectel, L80	Acquisition frequency: 5 Hz Resolution: 0.0001′ Horizontal Accuracy: < 2.5 m CEP[a] Timing Accuracy: 10 ns Reacquisition time: < 1 s
Altitude Quectel, L80	Acquisition frequency: 5 Hz Resolution: 0.1 m Timing Accuracy: 10 ns Reacquisition time: < 1 s
Meteorological measurements (C-Probe)	
Temperature Sensirion AG, SHT21	Acquisition frequency: 10 Hz Range: −40 °C to 120 °C Resolution: 0.1 °C Accuracy[b]: ±0.3 °C to ±0.7 °C Response time[d]: 5 s to 30 s
Relative humidity Sensirion AG, SHT21	Acquisition frequency: 10 Hz Range: 0 % to 100 % Resolution: 0.1 % Accuracy[c]: ±2 % to ±3 % Response time[d]: 8 s
Pressure Measurement Specialties, MS5611-01BA01	Acquisition frequency: 10 Hz Range: 10 mbar to 1200 mbar Altitude resolution: 10 cm Accuracy[e]: ±1.5 mbar Error band[f]: ±2.0 mbar Response time: < 100 ms
Differential pressure AMSYS GmbH & Co. KG, AMS 5915	Acquisition frequency: 10 Hz Range: 0 mbar to 10 mbar Resolution: 0.1 Pa Accuracy[g]: ±2.0 %FSO Response time: < 200 ms

Table 2.1: Datasheet specifications of the main direct measurements of interest recorded by the two Compass instruments C-Pilot EVO and C-Probe.

[a] CEP = Circular Error Probability. In military science, it is defined as the radius of a circle such that the probability that an impact point falls inside it is equal to 50 % (Liu et al., 2018). Here, it means that the probability that a GPS measurement of horizontal position falls inside a circle centered on its true value, of radius 2.5 m, is 50 %.
[b] The given range is valid for temperature values measured during flights (about 6 °C to 24 °C). In this range, accuracy values increase with decreasing temperature.
[c] The given range is valid for temperature and relative humidity values measured during flights (about 6 °C to 24 °C and 42 % to 90 %). In this range, accuracy values increase with decreasing temperature and relative humidity.
[d] Time for achieving 63 % of a step function, valid at 25 °C and 1 m s^{-1} airflow. For temperature, it depends on heat conductivity of the sensor substrate.
[e] Valid at 25 °C and 750 mbar.
[f] Valid at 0 °C to 50 °C and 450 mbar to 1100 mbar.
[g] Valid at −25 °C to 85 °C. This is total accuracy, i.e. the overall error across the entire temperature range, including the adjustment error (offset and span), nonlinearity, pressure hysteresis and repeatability. FSO is the Full Span Output and equals 10 mbar.

necting the opposite sides of the slope, in order to cover as much as possible the area above it. At the same time, they were required to look for thermals, and in this case the trajectory should have been a spiral to stay inside the ascending air as long as possible. Once left the slope, the trajectory over the valley had to be straight towards the landing site. In this way, during straight trajectories over the slope and the valley, the dominant boundary layer structure could have been probed, while the spiral trajectories allowed to take measurements inside, or likely inside, convective plumes. To limit additional flux distortions to those naturally provided by the harness and, to a lesser extent, by the wing, pilots were asked to avoid special manoeuvres, with the exception of take-off and landing procedures, possibly conducting a smooth flight. This would have helped also to keep the sink rate as costant as possible, that has been useful for the computation of the vertical component of the wind in Section 3.3.7. Safety was obviously the first requirement to be satisfied and the choice of experienced pilots was done also in this sense. Trajectories differed sometimes from the planned ones, for safety reasons or particular weather conditions (see Section 2.6).

At take-off, the calibration of the magnetic compass of C-Probe was performed, as suggested in the user manual: after securing the probe and the other instruments to the cockpit, the cockpit was rotated 360° around the three main axes of C-Probe. Other devices that could cause magnetic interference, such as the radio or the smartphone, were placed if possible on or inside the cockpit, to undergo the same rotation, or as distant as possible from C-Probe (e.g. inside the harness).

A calibration to correctly remove the offset of the differential pressure measurement by the Pitot tube was instead performed inside, every morning before the flights, placing C-Probe on a table, protected from the wind, and starting the automatic calibration procedure with a command on C-Pilot.

In addition, an automatic system operates a continuous calibration during the flight on the scale of the differential pressure measurement. Since the system in patent-pending, at the request of the company details on this operation cannot be disclosed.

A total of 19 flights were performed throughout the field campaign, as listed in Table 2.2. The 11 involved pilots are referred to by a number (1, 2, ..., 11), while the three couples of instruments by a letter (a, b, c). Take-off and landing times (local time, that is UTC+2) are approximated times from those evaluated in Section 3.3.2, and the take-off sites are indicated with the same letters of those in Figure 2.4. Simultaneous flights are grouped in lines of the same colour (white or grey). The last column specifies the type of harness used, upright (Figure 2.1) or pod (Figure 2.2.)

flight	date	take-off	landing	pilot	instruments	harness
1	17/09/2019	15:18, E	15:37, Boscherai	1	*a*	pod
2	17/09/2019	15:18, E	15:36, Boscherai	2	*c*	pod
3	17/09/2019	15:18, E	15:36, Boscherai	3	*b*	pod
4	20/09/2019	13:00, S	—/—, Boscherai	4	*b*	pod
5	20/09/2019	13:00, S	13:36, Boscherai	2	*c*	pod
6	20/09/2019	13:01, S	13:37, Boscherai	5	*a*	pod
7	20/09/2019	15:44, C	17:02, Boscherai	5	*a*	pod
8	20/09/2019	16:12, E	16:33, Boscherai	6	*c*	upright
9	21/09/2019	12:37, E	13:01, Boscherai	7	*c*	pod
10	21/09/2019	12:37, E	13:08, Boscherai	4	*a*	pod
11	24/09/2019	15:00, W	15:57, Boscherai	8	*c*	pod
12	24/09/2019	15:09, W	15:34, Boscherai	3	*a*	pod
13	24/09/2019	15:37, W	15:57, Boscherai	2	*b*	pod
14	26/09/2019	14:19, S	14:42, Boscherai	7	*a*	pod
15	26/09/2019	14:30, S	14:45, Boscherai	9	*c*	upright
16	26/09/2019	16:32, S	16:55, Arten	6	*a*	upright
17	27/09/2019	14:51, S	15:06, Boscherai	10	*a*	pod
18	27/09/2019	14:51, S	15:08, Boscherai	11	*c*	pod
19	30/09/2019	15:27, E	15:59, Boscherai	6	*c*	upright

Table 2.2: Overview of the flights. Simultaneous flights are grouped in rows of the same colour (white or grey).

2.5   Surface weather stations

To complement airborne measurements, data from the three nearest surface weather stations were collected. Two of them are operated by Agenzia Regionale per la Prevenzione e Protezione Ambientale del Veneto (ARPAV) and are located respectively in Feltre and on the top of Monte Avena. The third is a Davis Vantage Pro 2 included in the amateur network operated by the association MeteoNetwork and is placed at the base of the mountain. Their position is indicated by yellow-sun markers in Figure 2.4.

Details on the recorded measurements can be found in Table 2.3. Available data are given every 5, 10 or 15 min, according to the station and the variable, during the period 17-30 September 2019. ARPAV stations unfortunately do not include a pressure sensor, while Festisei station does not record the solar radiation.

Temperature, relative humidity, pressure and wind data have been used in Chapter 3 and Chapter 4 as a reference for airborne measurements.

Station	Position	Measured quantities
ARPAV Monte Avena	46.03144 N, 11.82736 E 1415 m a.s.l.	prec., 5 min wind dir. and speed at 5 m, 10 min temp. at 2 m, 15 min rel. hum. at 2 m, 15 min global solar rad., 15 min no pressure
ARPAV Feltre	46.01553 N, 11.89484 E 264 m a.s.l.	same as Monte Avena
MeteoNetwork Festisei	46.042 N, 11.869 E 465 m a.s.l.	prec., 5 min wind dir. and speed, 5 min temp., 5 min rel. hum., 5 min pressure, 5 min no solar rad.

Table 2.3: Details on the three considered surface weather stations.

2.6   Description of flights and synoptic conditions

A day by day description of the flights is reported below, along with a brief overview of the synoptic conditions on the base of soundings data and synoptic charts. Also, photographs and video frames documentation (not shown) have helped to contextualise the atmospheric conditions, and Google Earth images show the trajectory of the flights on each day.

Soundings diagrams and data are those made available by the Department of Atmospheric Science of the University of Wyoming, USA (`http://weather.uwyo.edu/upperair/sounding.html`), for the stations located at Rivolto Airport (UD) (station number and identifier: 16045, LIPI) and at Milano Linate Airport (station number and identifier: 16080, LIML), for each day at 12Z (14:00 local time). Their position is shown in Figure 2.6.

The synoptic charts considered here are the surface analysis by Deutscher Wetterdienst (DWD, the German national weather service) and the CFS 500 hPa reanalysis by the National Centers for Environmental Prediction of NOAA (NCEP), available at the Wetterzentrale website (`https://www.wetterzentrale.de`). They are both referred to 12:00 UTC (14:00 local time). Insights into the CFS (Climate Forecast System) model can be found in Saha et al. (2014).

Soundings data are also used in Chapter 4 for comparisons with flight data.

Figure 2.6: Google Earth image of Northern Italy. The blue, black and grey markers respectively indicate the position of Monte Avena, LIPI (Rivolto) and LIML (Milano) sounding stations.

2.6.1   17 September

A modest trough from Northern Europe associated with a cold front, suggested by surface isobars in Figure 2.7a and by geopotential height contours in Figure 2.7b, interested the northern regions of Italy bringing relative low pressure (about 1015 hPa at the surface), but no precipitations on Monte Avena. The weather was partially sunny, with cumulus clouds.

Figure 2.8a and Figure 2.8b indicate a relative moist atmosphere in the lower boundary layer, highlighted by temperature and dew point soundings rather close to each other. The lowest temperature inversions appear to be approximately at 1000 m and 2030 m in Rivolto (LIPI), and at 800 m and 1000 m in Milano (LIML) – these data are derived from the data files of each station.

The Lifting Condensation Level (LCL) and the Level of Free Convection (LFC) result respectively 927.3 hPa, 919.9 hPa (LIPI) and 890.9 hPa, 756.1 hPa (LIML). The Convective Inhibition Energy (CINE) and the Convective Available Potential Energy (CAPE) are respectively $-0.4\,\mathrm{J\,kg^{-1}}$, $-134.4\,\mathrm{J\,kg^{-1}}$ (LIPI) and $312.7\,\mathrm{J\,kg^{-1}}$, $211.2\,\mathrm{J\,kg^{-1}}$ (LIML).

The low LCL explains the formation of cumulus clouds at altitude levels even

below the top of Monte Avena, thus preventing the pilots from reaching elevated heights, as flight inside clouds is generally unsafe. From the soundings and the synoptic conditions, the atmosphere is expected not to produce relevant updrafts at the altitude levels of the flights, as observed during the flights #1, #2 and #3 performed on this day. Three pilots simultaneously took off from the E take-off in the early afternoon (see Table 2.2 for take-off and landing times), and probed the eastern side of Monte Avena with S-shaped trajectories until they reached the valley (Figure 2.9), from which they continued with straight trajectories to land at the Boscherai landing area. None of them encountered ascending air during the flight.
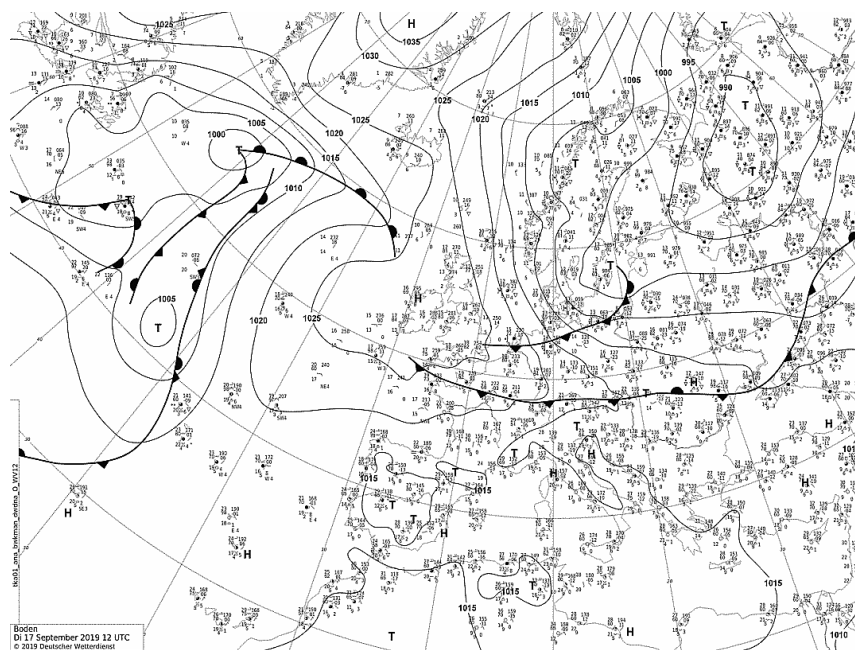
(a) Surface analysis at 12:00 UTC. Source: Deutscher Wetterdienst.
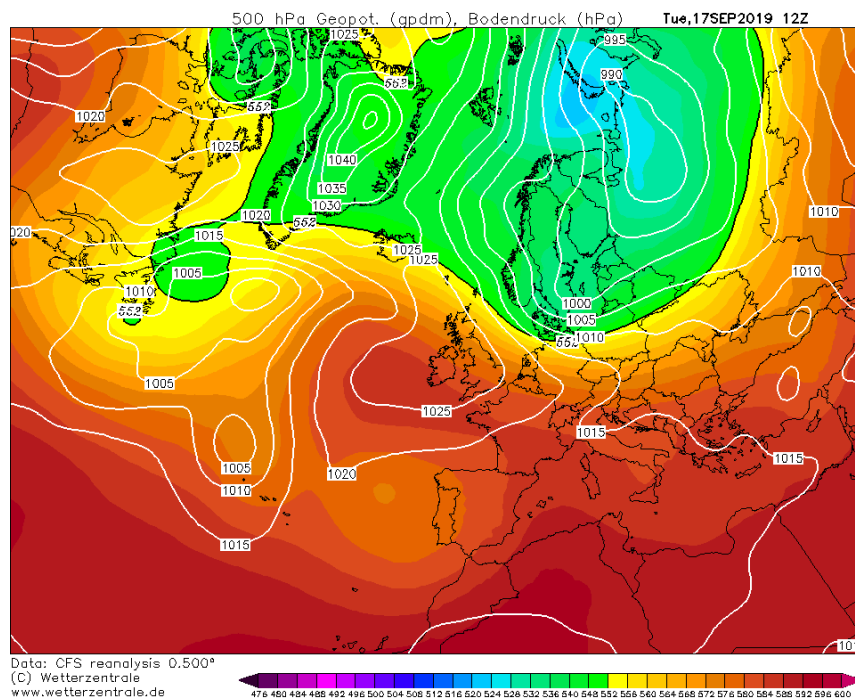
(b) CFS 500 hPa reanalysis at 12:00 UTC. Source: Wetterzentrale.

Figure 2.7: Synoptic charts on 17 September.
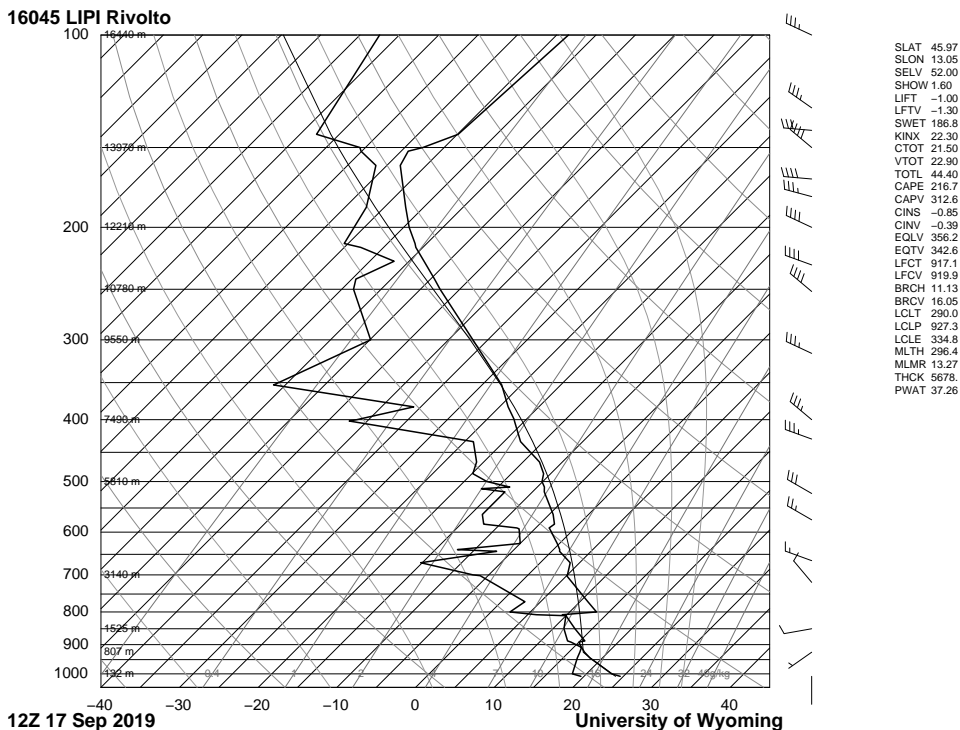
(a) Rivolto (LIPI) sounding.
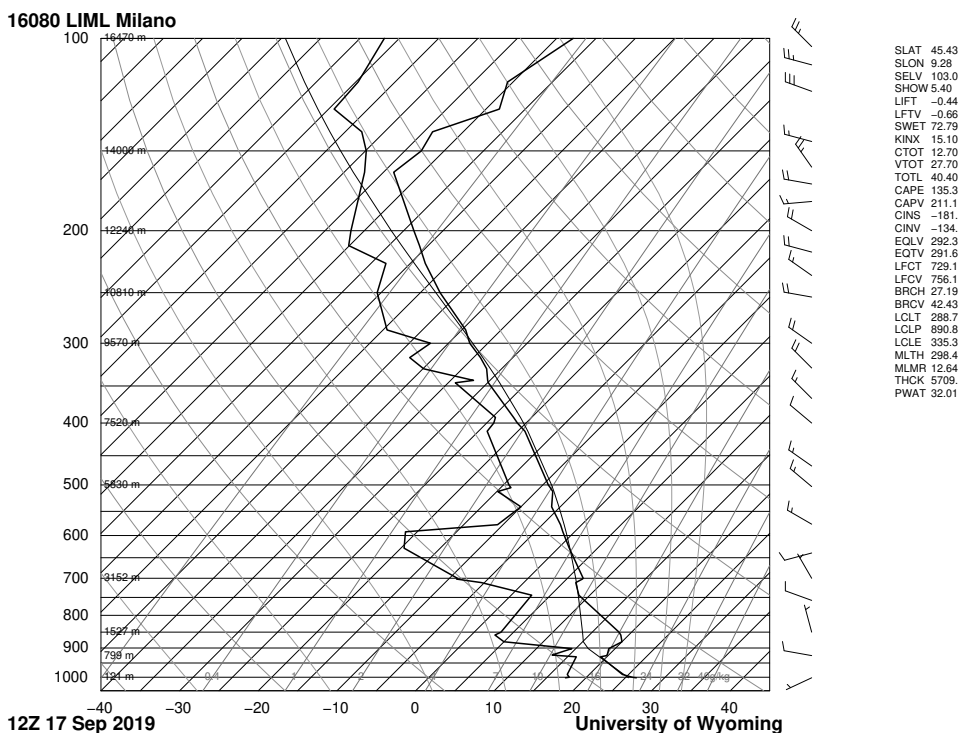
(b) Milano (LIML) sounding.

Figure 2.8: Skew-T log-P diagrams with soundings data on 17 September at 12:00 UTC, for the stations in Rivolto (LIPI) and Milano (LIML). Source: University of Wyoming.
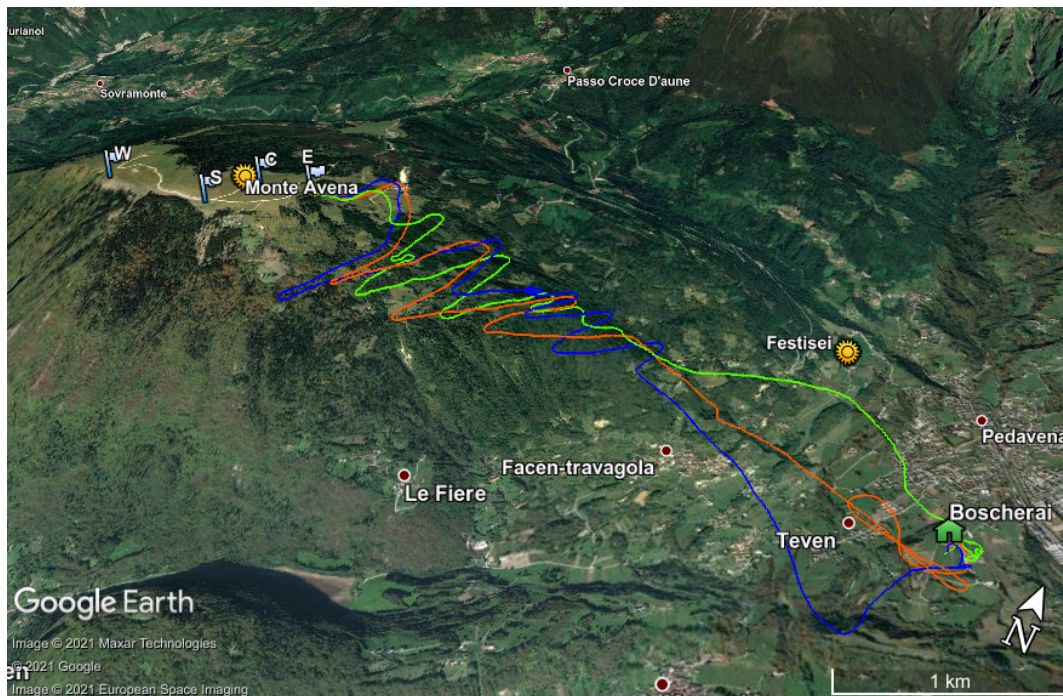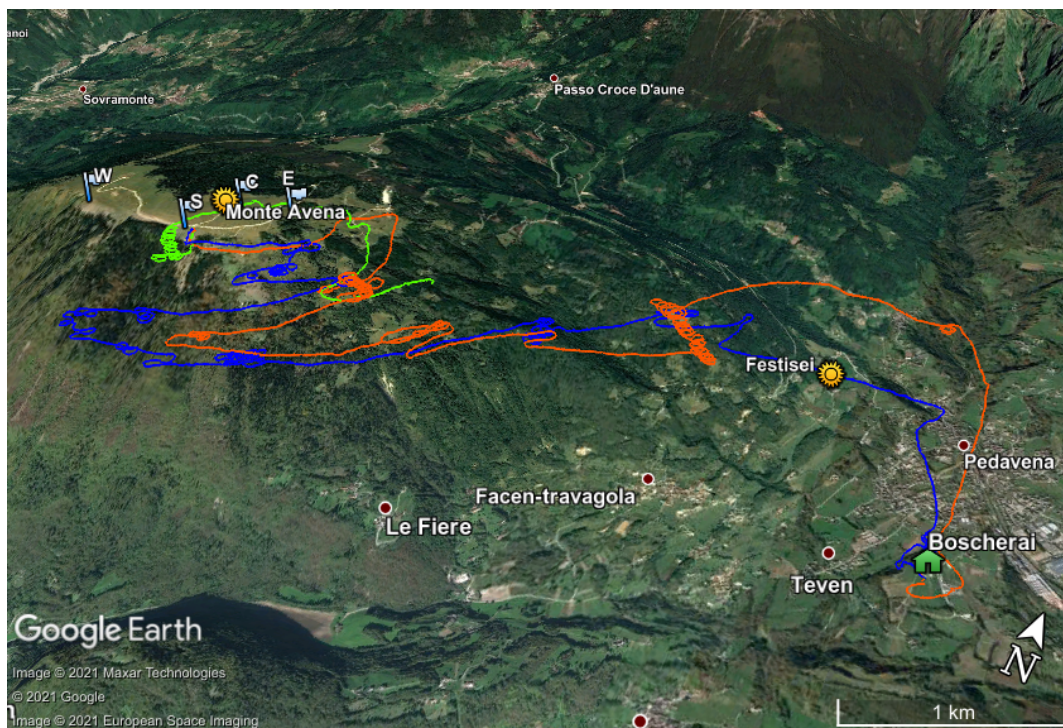
Figure 2.9: Google Earth image of the trajectories of flights #1 (blue), #2 (orange) and #3 (green) performed on 17 September.

2.6.2   20 September

20 September started with a cloudy morning, but developed as a bright, sunny day from the early afternoon. Synoptic charts in Figure 2.10 suggest a pronounced ridge of high pressure interesting Europe and Northern Italy, with geopotential height around 5800 gpdm. Soundings data in Figure 2.11 show ideal atmospheric conditions for flying: drier with respect to 17 September (temperature and dew point soundings are rather distant) and stable conditions, with the lowest temperature inversion above 1570 m with LCL at 814.5 hPa (about 1900 m) in Rivolto (LIPI), and above 2000 m with LCL at 871.8 hPa (about 1800 m) in Milano (LIML). Zero CAPE values suggest that the development of thunderstorms is highly inhibited.

Two groups of flights were performed: the first one approximately at 1 pm (flights #4, #5, #6), and the second one in the afternoon (flights #7, #8) – see Table 2.2. Flight trajectories are shown in Figure 2.12 and Figure 2.13. The take-off chosen for the first group of flights was the S take-off, as that time of the day presented meteorological conditions typically found at Monte Avena, with southerly upslope wind at the top generated by sun exposure of its southern side. Indeed, the pilots found ascending air both under and above the take-off, marked respectively by green and blue spiral trajectories. Pilot #2 instead headed directly towards the eastern

side, where he found ascent air at two different altitude levels.

The green trajectory stops in the middle of the slope, since C-Pilot shut down unexpectedly at that moment. The pilot was not able to turn it on again, thus this flight, for reasons concerning the successive correction of GPS altitude (Section 3.1.3), has not been considered for further analysis.

In the afternoon, the pilots took off from the eastern side, at C (flight #7) and E (flight #8) take-offs. While flight #8 interested the eastern side of the mountain with modest ascent found, the pilot of flight #7 covered a greater distance in the south and north directions, efficiently flying inside three significant updraft zones (blue spiral sections of the trajectories). For reasons explained in Section 3.3.6, also flight #8 has been excluded from the following analysis of Chapter 4.
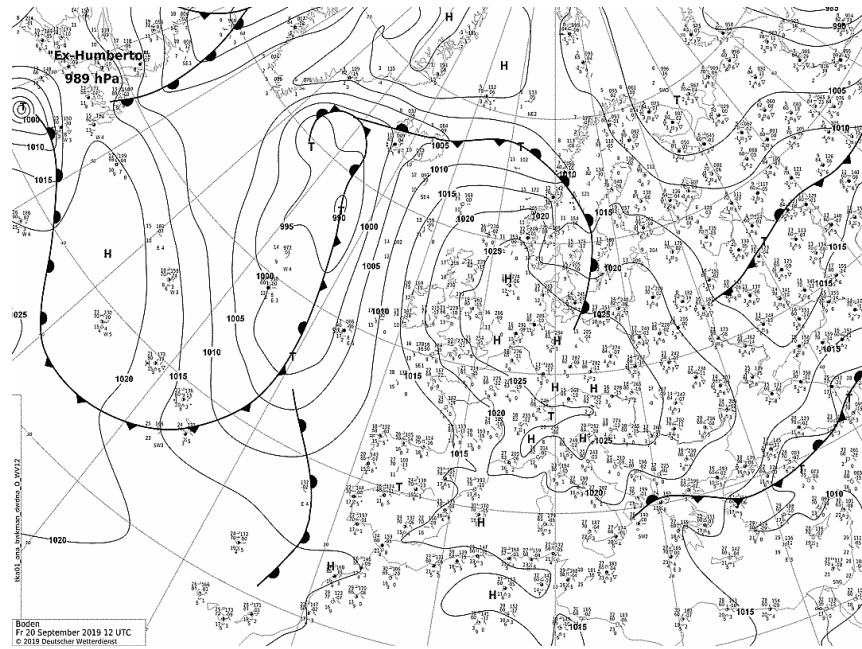
(a) Surface analysis at 12:00 UTC. Source: Deutscher Wetterdienst.
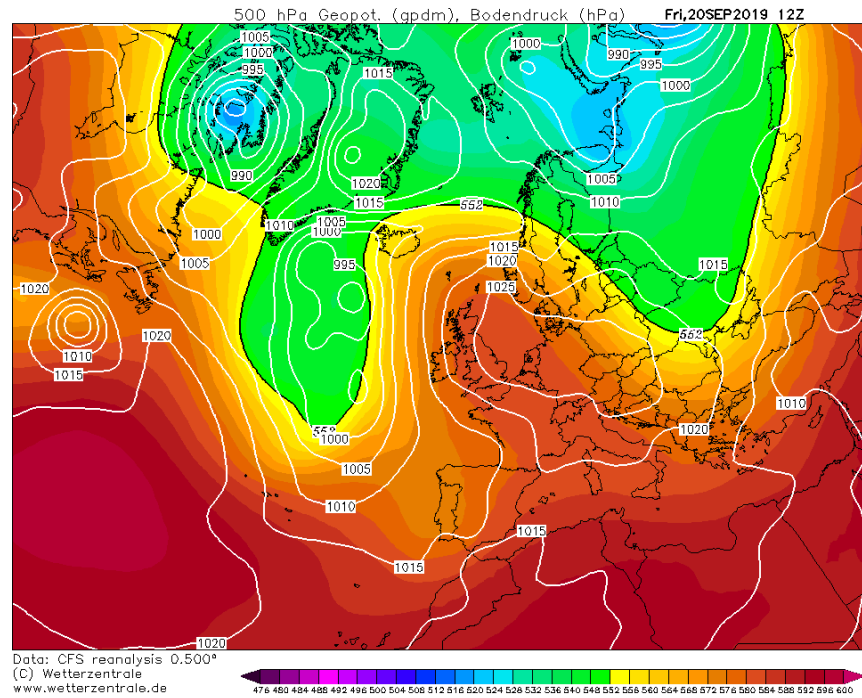
(b) CFS 500 hPa reanalysis at 12:00 UTC. Source: Wetterzentrale.

Figure 2.10: Synoptic charts on 20 September.
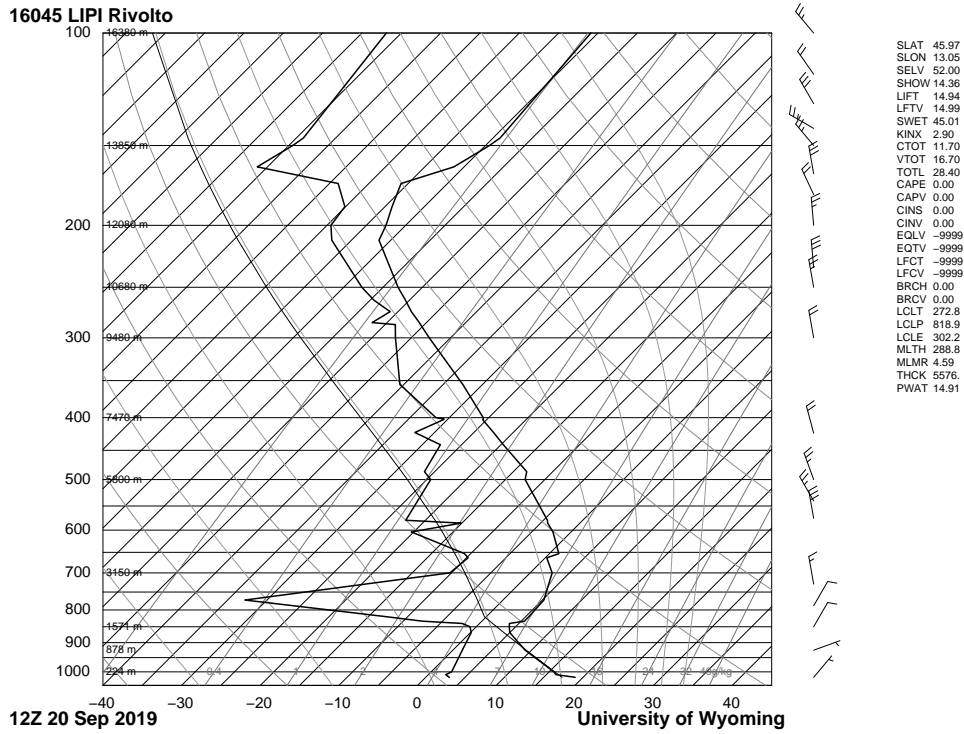
(a) Rivolto (LIPI) sounding.
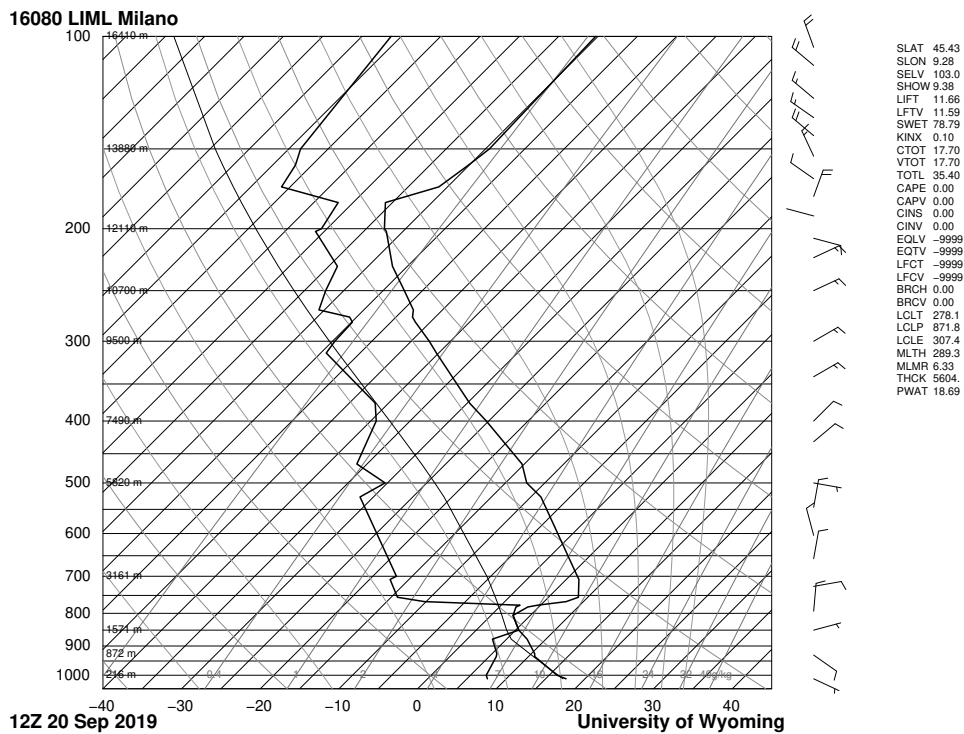
(b) Milano (LIML) sounding.

Figure 2.11: Skew-T log-P diagrams with soundings data on 20 September at 12:00 UTC, for the stations in Rivolto (LIPI) and Milano (LIML). Source: University of Wyoming.

Figure 2.12: Google Earth image of the trajectories of flights #4 (green), #5 (orange) and #6 (blue) performed on 20 September, early afternoon.
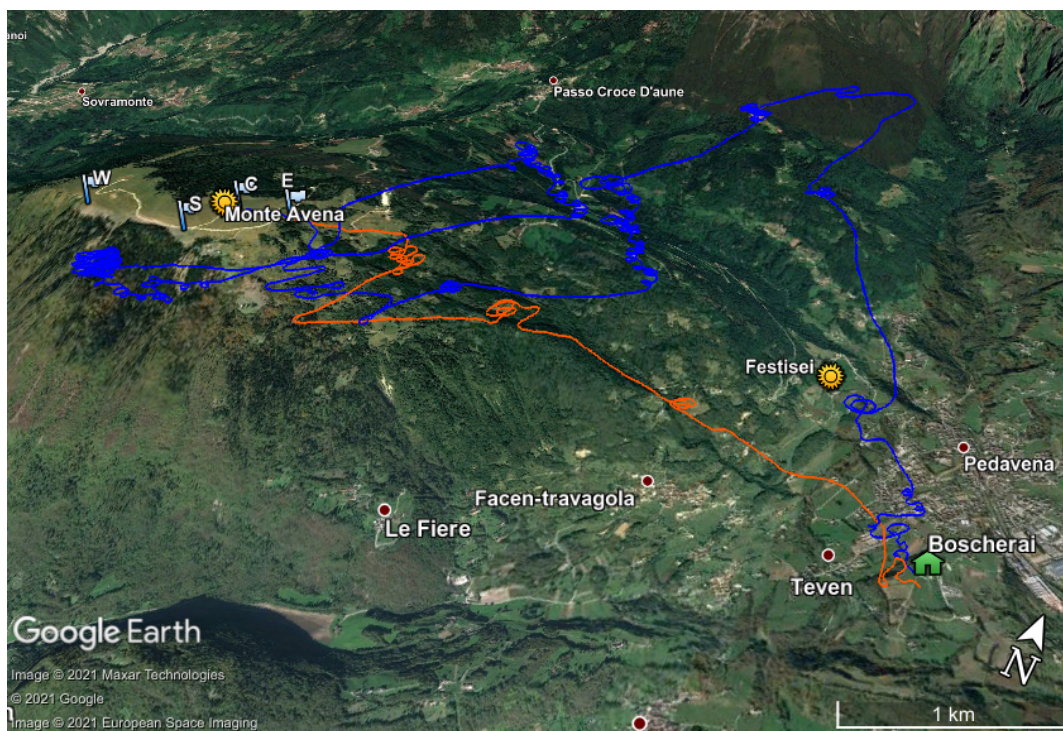
Figure 2.13: Google Earth image of the trajectories of flights #7 (blue) and #8 (orange) performed on 20 September, afternoon.

2.6.3   21 September

The synoptic and meteorological conditions on 21 September were very similar to those of the previous day: again, a ridge of high pressure brought sunny weather and dry, stable conditions good for flying, with the lowest temperature inversion above 1500 m, and LCL at 814.5 hPa (about 1917 m, LIML) and 772.5 hPa (about 2200 m, LIPI). Zero CAPE values resulted on this day too.

Two simultaneous flights (#9 and #10) were performed in the late morning, lasting about half an hour (see Table 2.2 for take-off and landing times) on the eastern side of Monte Avena (see Figure 2.16). The pilots took off from the E take-off and followed S-shaped trajectories until they found ascending air inside which, with spiral trajectories, they gained height climbing the slope. Once outside the upward flow, they headed towards the Boscherai landing area.
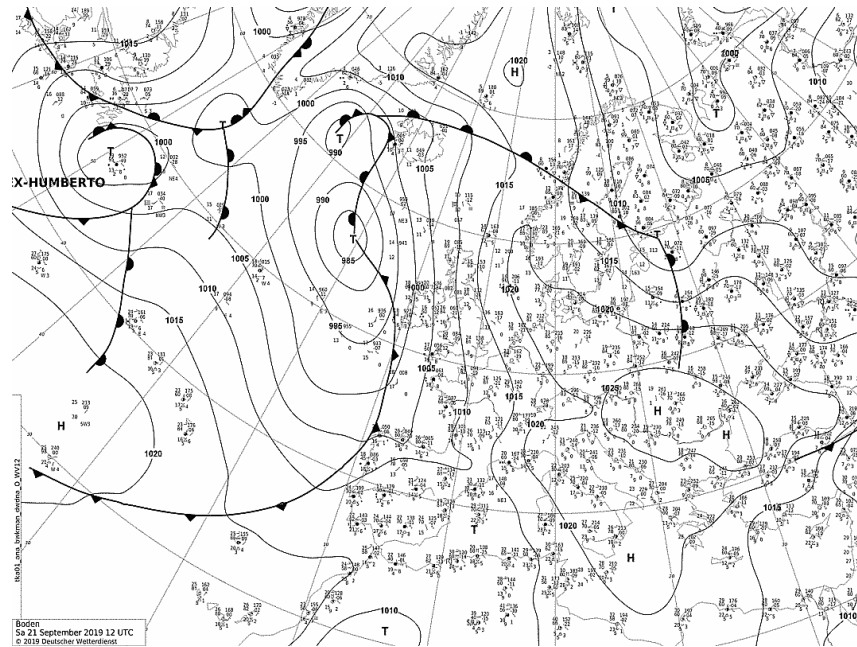
(a) Surface analysis at 12:00 UTC. Source: Deutscher Wetterdienst.
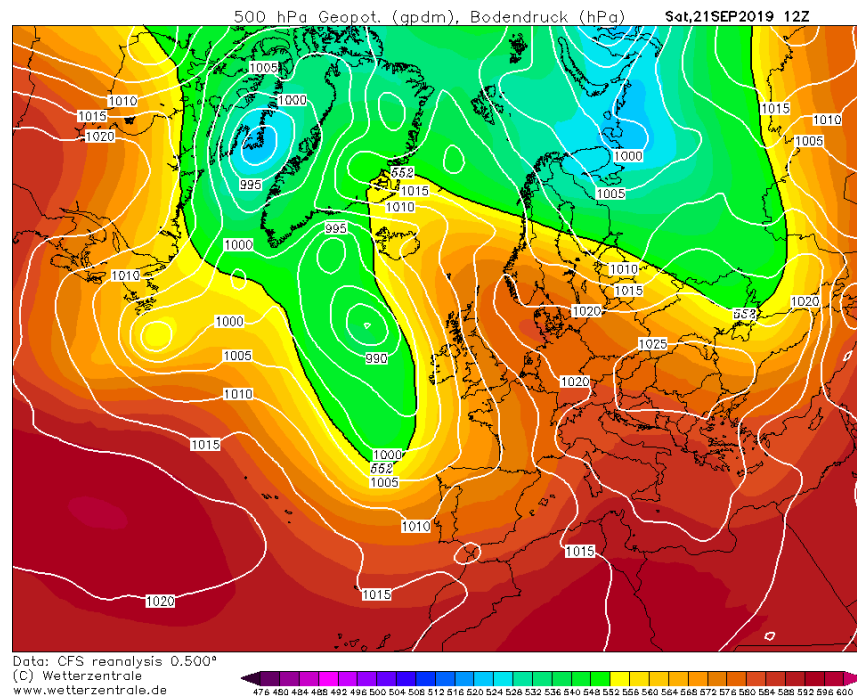
(b) CFS 500 hPa reanalysis at 12:00 UTC. Source: Wetterzentrale.

Figure 2.14: Synoptic charts on 21 September.
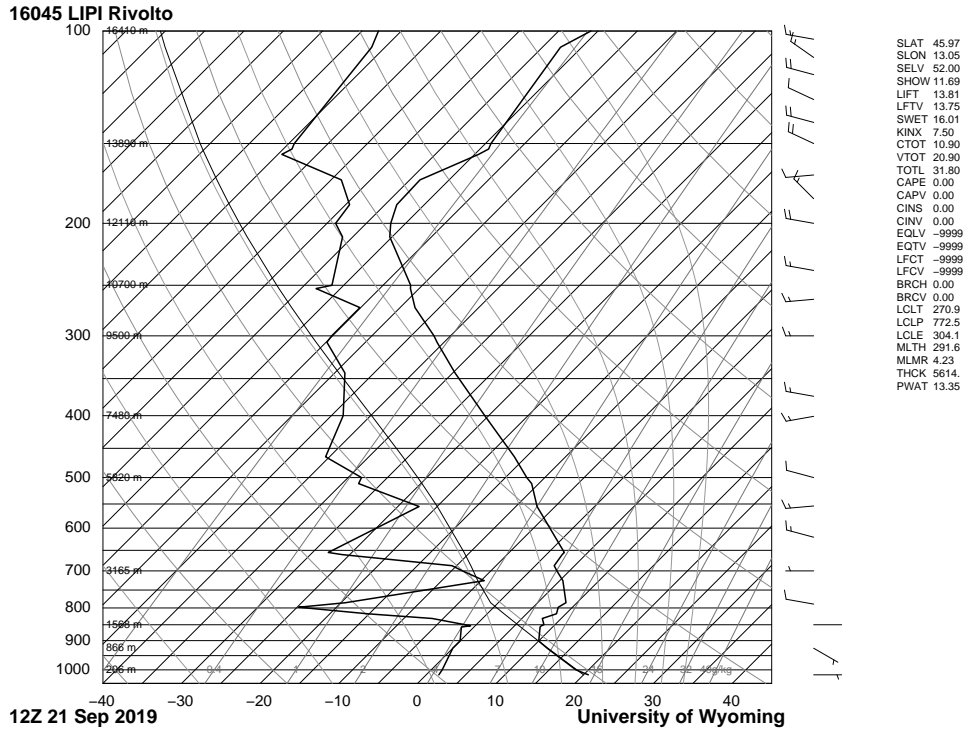
(a) Rivolto (LIPI) sounding.
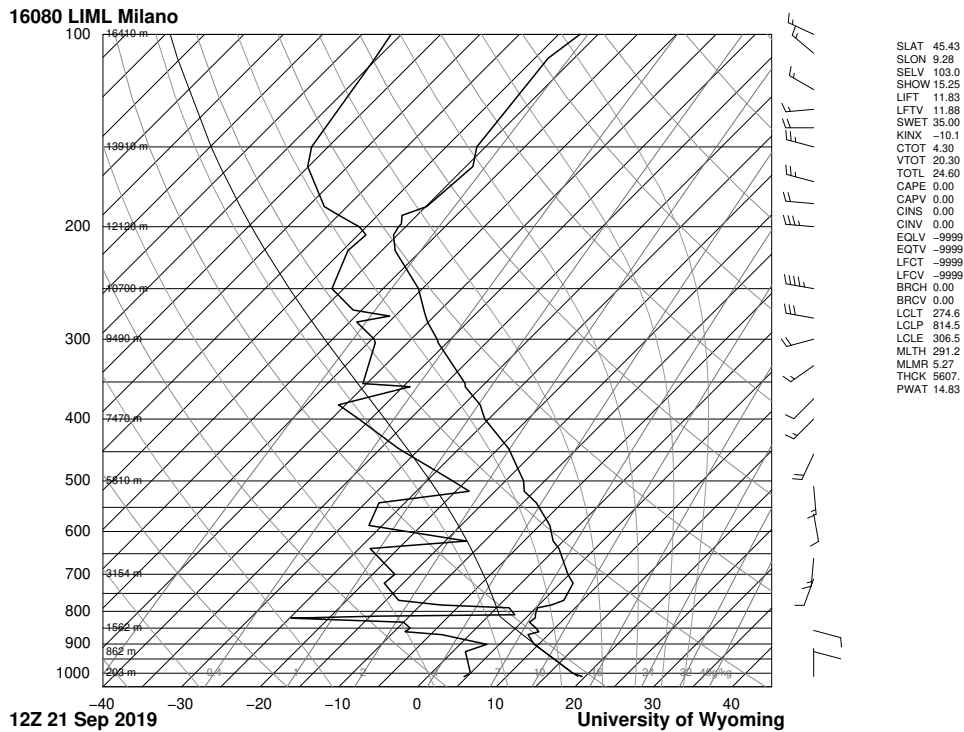
(b) Milano (LIML) sounding.

Figure 2.15: Skew-T log-P diagrams with soundings data on 21 September at 12:00 UTC, for the stations in Rivolto (LIPI) and Milano (LIML). Source: University of Wyoming.
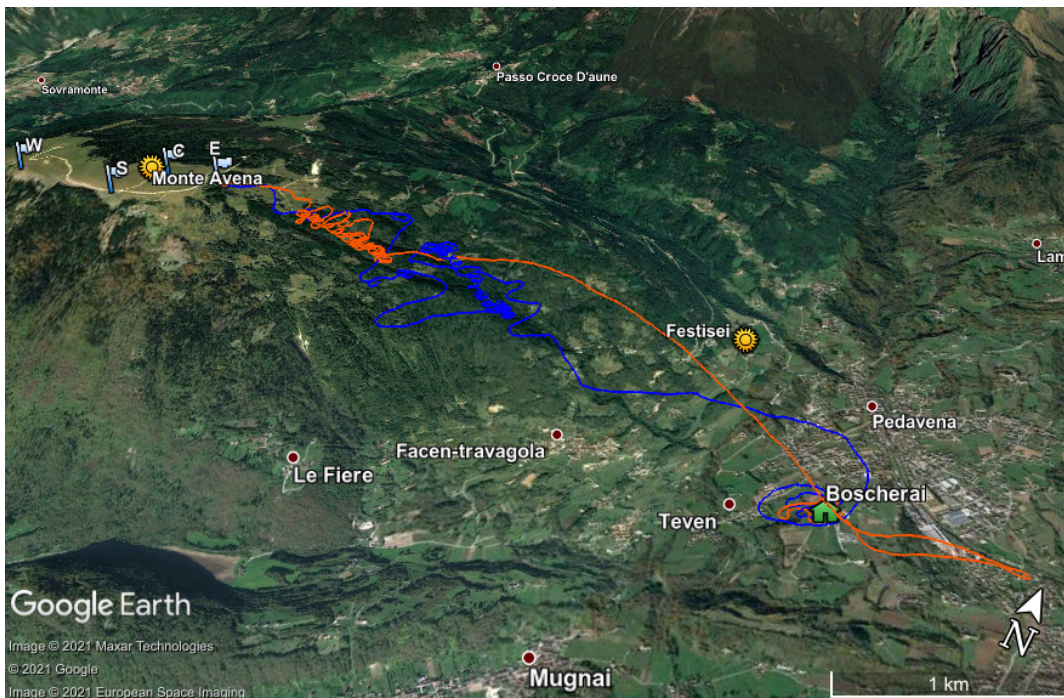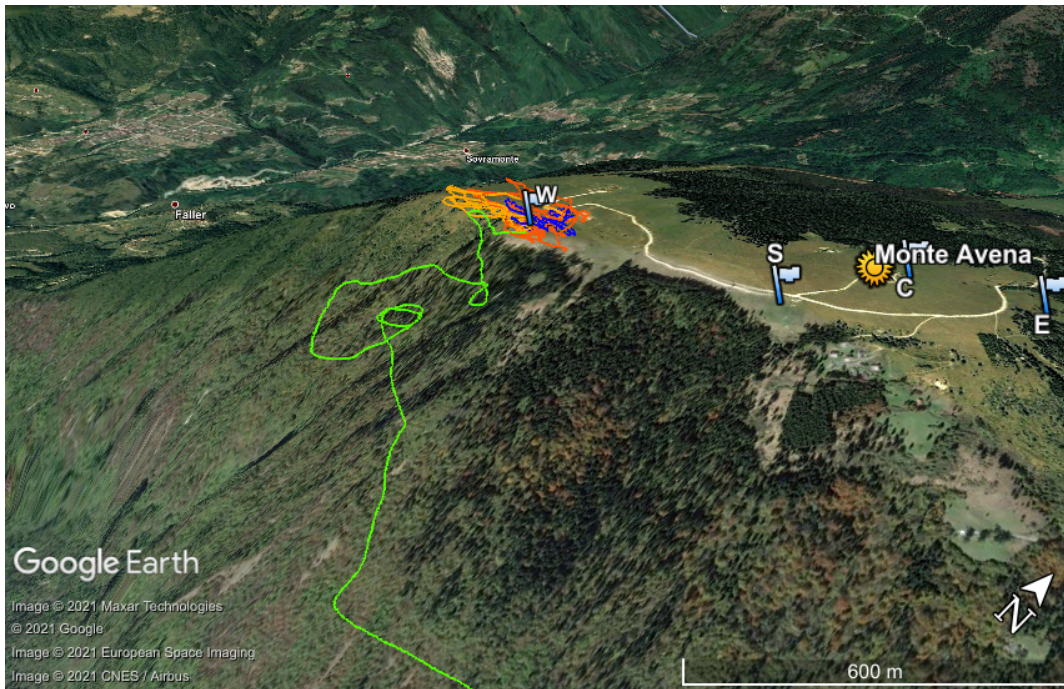
Figure 2.16: Google Earth image of the trajectories of flights #9 (orange) and #10 (blue) performed on 21 September.

2.6.4   24 September

24 September was a cloudy (mainly stratocumulus clouds) and windy day. A modest ridge and colder air than on the previous days, with geopotential height about 5720 gpdm, were found in the area of Monte Avena (Figure 2.17). Soundings in Figure 2.18 show the lowest temperature inversion at about 1000 m with LCL at 862 hPa (LIPI), and at about 900 m with LCL at 902 hPa (LIML), making it difficult to find convective structures at the altitude of the take-offs (about 1400 m). CAPE presented irrelevant values: $3.7 \, \mathrm{J\,kg^{-1}}$ (LIPI) and $1.0 \, \mathrm{J\,kg^{-1}}$ (LIML).

A moderate wind was blowing from west, thus the corresponding take-off site was chosen. No thermal structures were found, but instead the three pilots (flights #11, #12 and #13) were able to fly above the take-off without losing height, sustained by the wind: it was likely associated with synoptic conditions rather than thermal activity. Since the pilots, before heading towards the landing site Boscherai, performed the so-called "top landing" – they landed at take-off –, flights #11 e #12 have been divided respectively in three and two parts. Flight #11 - parts 1 and 2, and flight #12 - part 1 start with take-off and end with top-landing, while flights #11 - part 3, #12 - part 2 and #13 normally start at take-off and end at Boscherai. Figure 2.19 and Figure 2.20 respectively show the trajectories of each part. After leaving the W take-off, the meteorological conditions did not allow to find convection along the

hillsides of Monte Avena, as shown by the gliding trajectories in Figure 2.20.
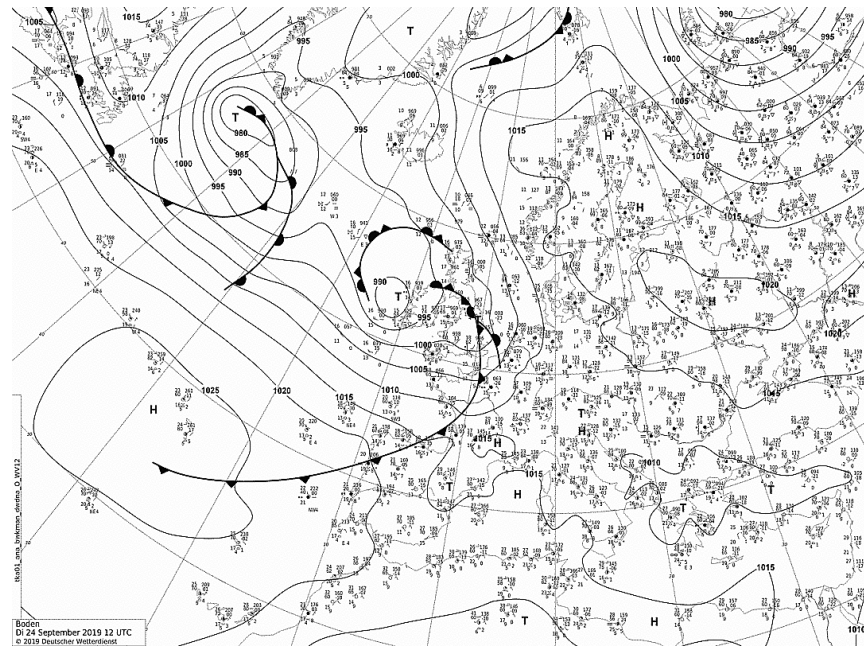

(a) Surface analysis at 12:00 UTC. Source: Deutscher Wetterdienst.
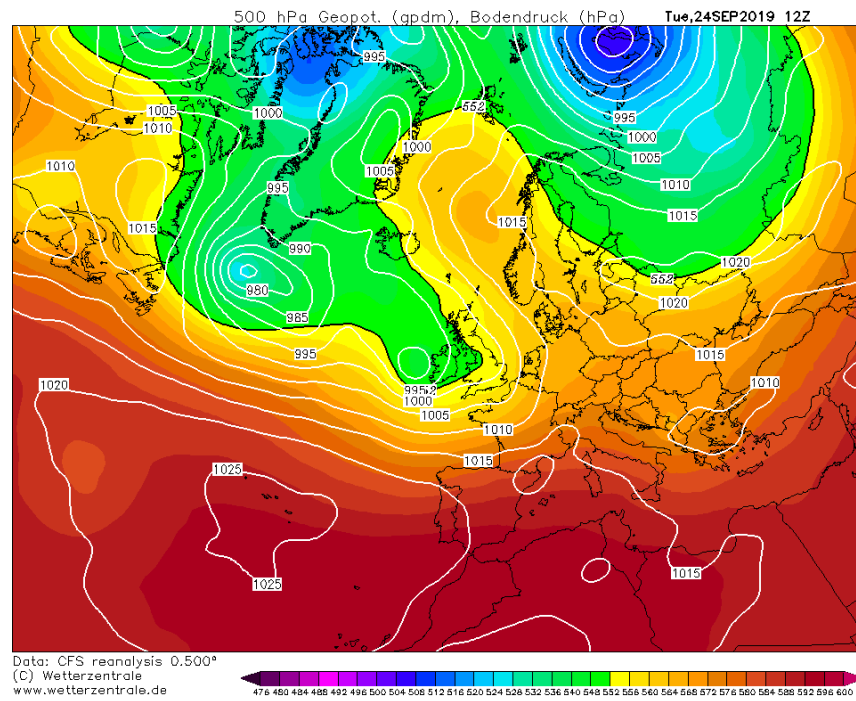
(b) CFS 500 hPa reanalysis at 12:00 UTC. Source: Wetterzentrale.

Figure 2.17: Synoptic charts on 24 September.
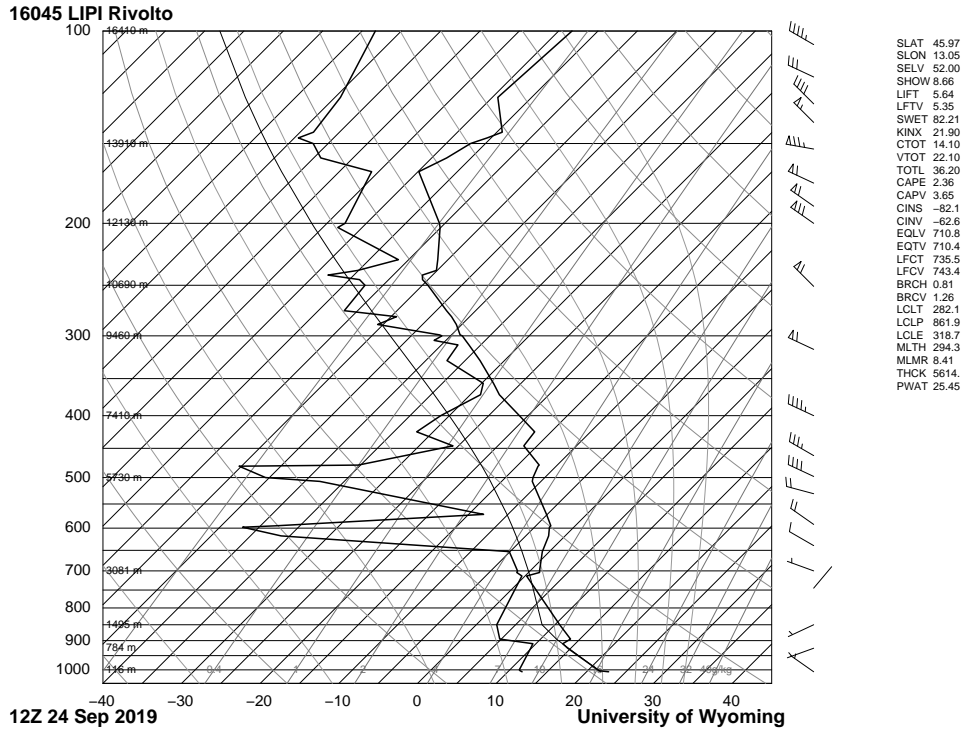
(a) Rivolto (LIPI) sounding.
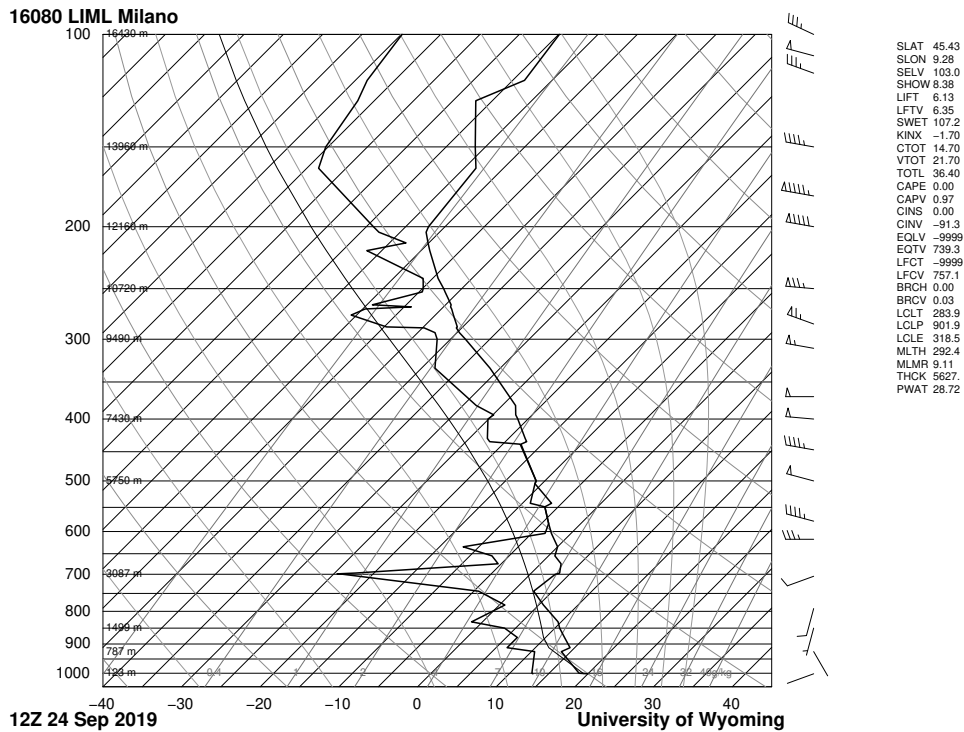
(b) Milano (LIML) sounding.

Figure 2.18: Skew-T log-P diagrams with soundings data on 24 September at 12:00 UTC, for the stations in Rivolto (LIPI) and Milano (LIML). Source: University of Wyoming.
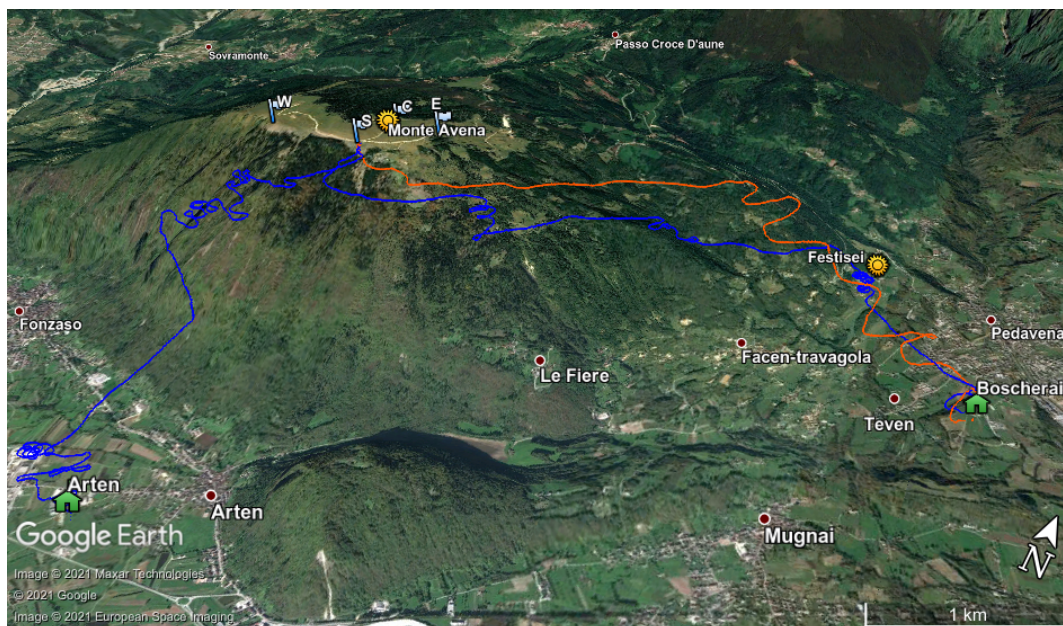
Figure 2.19: Google Earth image of the trajectories of flights #11 - parts 1 and 2 (orange and yellow), #12 - part 1 (blue) and #13 (green) performed on 24 September.
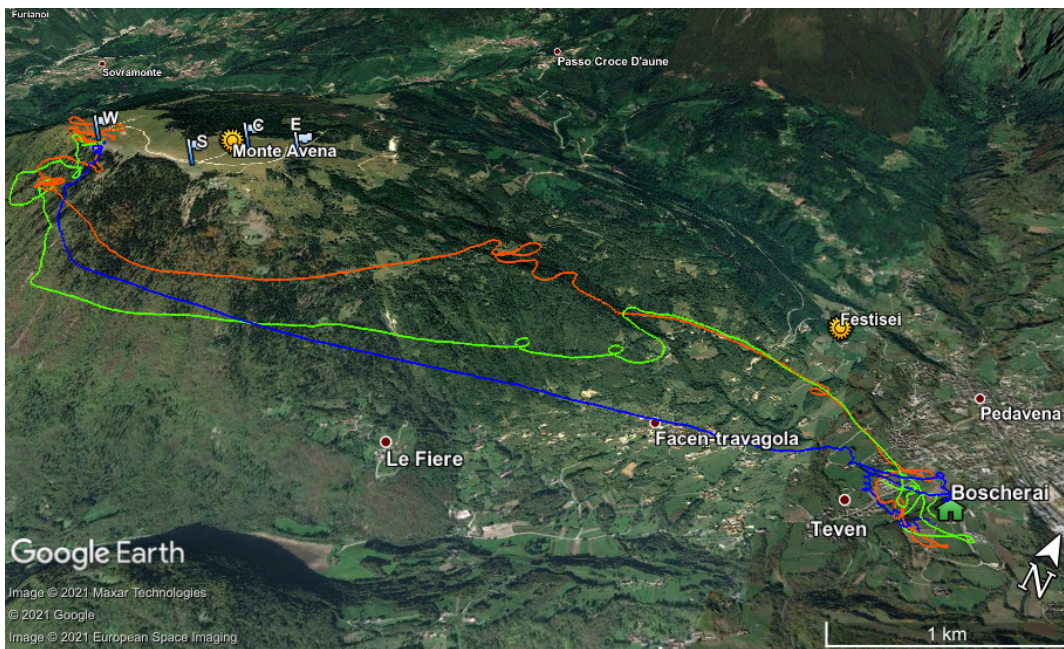
Figure 2.20: Google Earth image of the trajectories of flights #11 - part 3 (orange), #12 - part 2 (blue) and #13 (green) performed on 24 September.

2.6.5   26 September

Synoptic conditions on 26 September were similar to those on 24 September, with a modest ridge over Northern Italy and geopotential height of about 5720 gpdm (Figure 2.21). The weather, however, was mostly sunny with some cirrus and cumulus clouds. Soundings in Rivolto and Milano show a rather stable atmosphere (Figure 2.22), with CAPE values near zero: $0 \, \mathrm{J \, kg^{-1}}$ (LIPI) and $13.4 \, \mathrm{J \, kg^{-1}}$ (LIML). The lowest temperature inversion resulted between $1500 \, \mathrm{m}$ and $1900 \, \mathrm{m}$ (LIPI) and about $1000 \, \mathrm{m}$ (LIML).

Two flights (#14 and #15) were performed in the early afternoon (see Table 2.2 for take-off and landing times), from S take-off and landing at Boscherai. A third pilot (flight #16) instead took off from S take-off and sounded the W side of the mountain, landing at Arten (Figure 2.23). For all the cases, no relevant areas with ascent air were found.
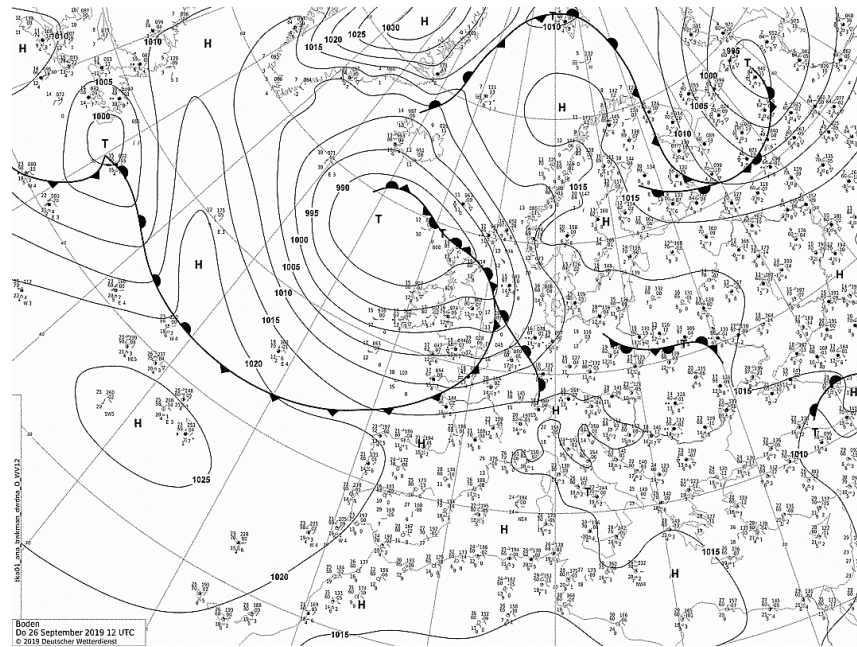
(a) Surface analysis at 12:00 UTC. Source: Deutscher Wetterdienst.
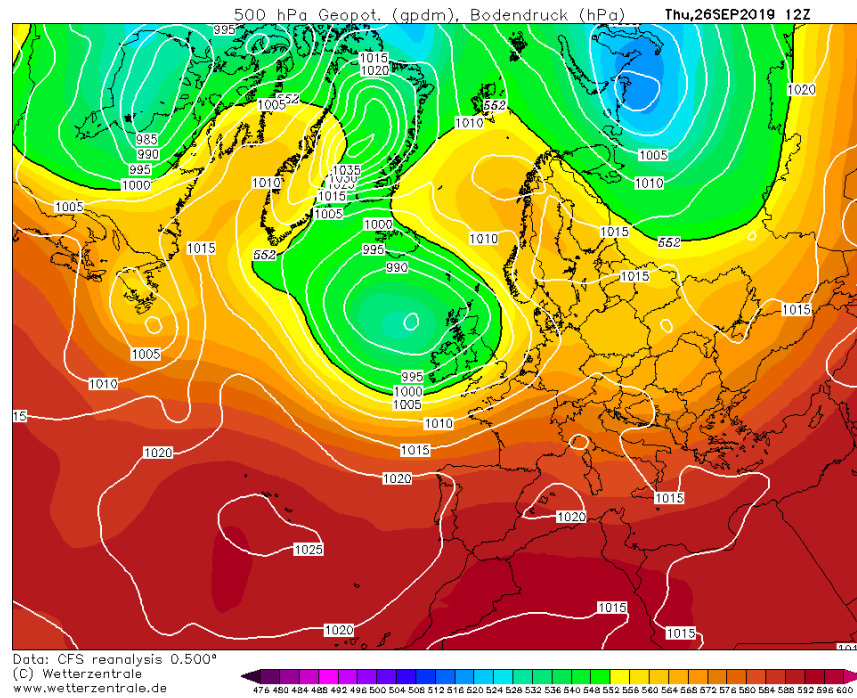
(b) CFS 500 hPa reanalysis at 12:00 UTC. Source: Wetterzentrale.

Figure 2.21: Synoptic charts on 26 September.
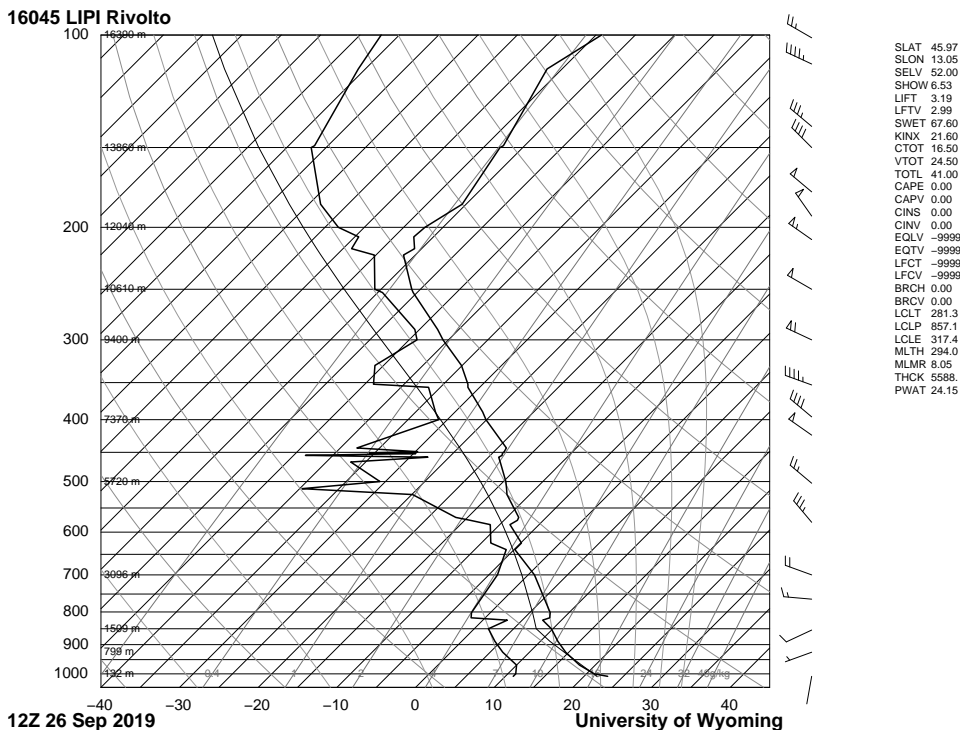
(a) Rivolto (LIPI) sounding.
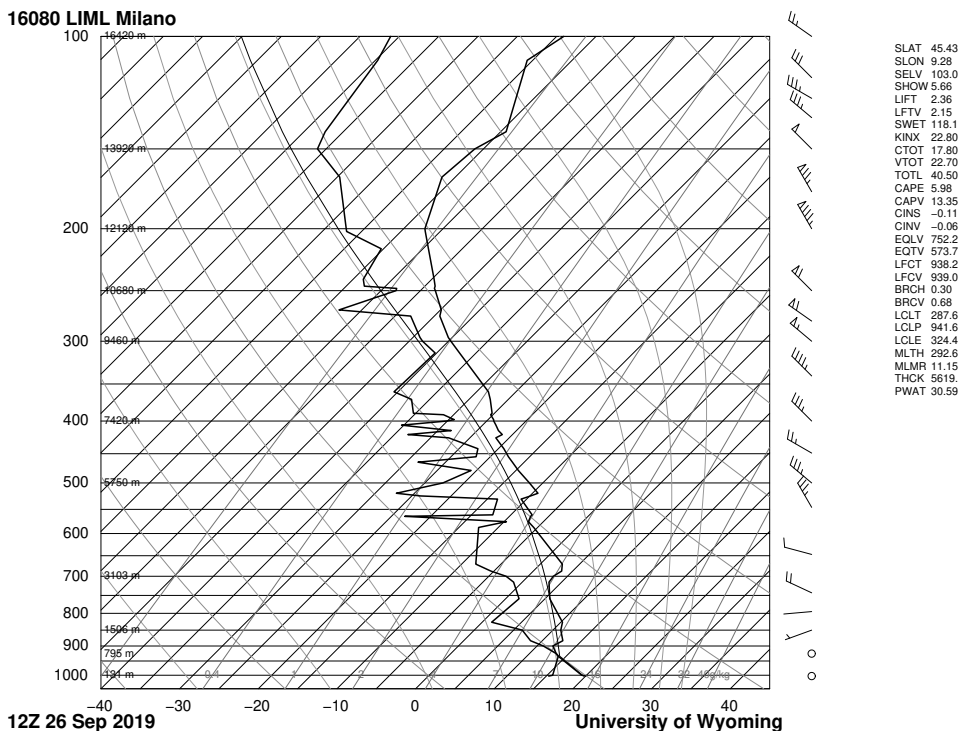
(b) Milano (LIML) sounding.

Figure 2.22: Skew-T log-P diagrams with soundings data on 26 September at 12:00 UTC, for the stations in Rivolto (LIPI) and Milano (LIML). Source: University of Wyoming.

48

Figure 2.23: Google Earth image of the trajectories of flights #14 (blue), #15 (orange) and #16 (blue) performed on 26 September.

2.6.6 27 September

On 27 September, a low pressure area associated with a cold front invested Northern Italy (Figure 2.24), causing a very cloudy and foggy day. Again, CAPE values from the soundings (Figure 2.25) were too low to allow strong convection development: $0 \, \mathrm{J \, kg^{-1}}$ (LIPI) and $31.3 \, \mathrm{J \, kg^{-1}}$ (LIML). LCL values were quite low: $282.5 \, \mathrm{hPa} \sim 1200 \, \mathrm{m}$ (LIPI) and $926.4 \, \mathrm{hPa} \sim 810 \, \mathrm{m}$ (LIML), thus with probable (and observed) formation of clouds under the take-offs.

Despite the conditions not conducive to convective structures, two simultaneous flights (#17 and #18) were performed in the early afternoon, taking off from S and landing at Boscherai (Figure 2.26). As expected, only a simple glide could be carried out to reach the landing.
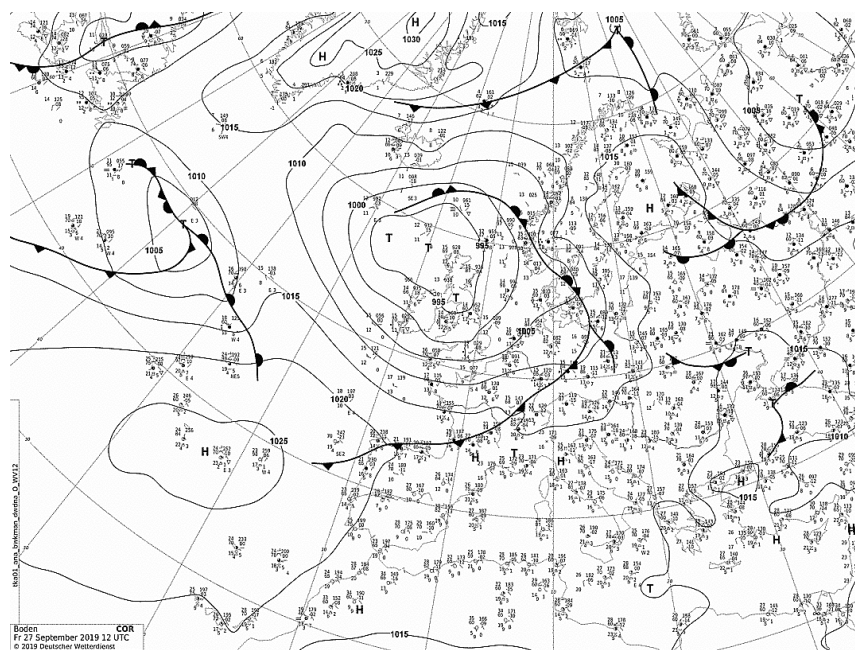
(a) Surface analysis at 12:00 UTC. Source: Deutscher Wetterdienst.
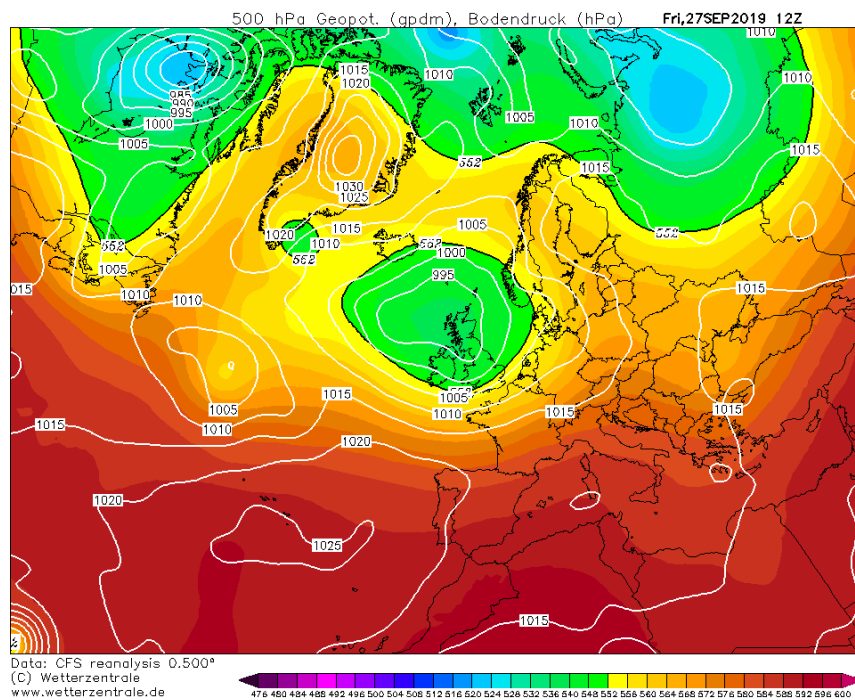
(b) CFS 500 hPa reanalysis at 12:00 UTC. Source: Wetterzentrale.

Figure 2.24: Synoptic charts on 27 September.
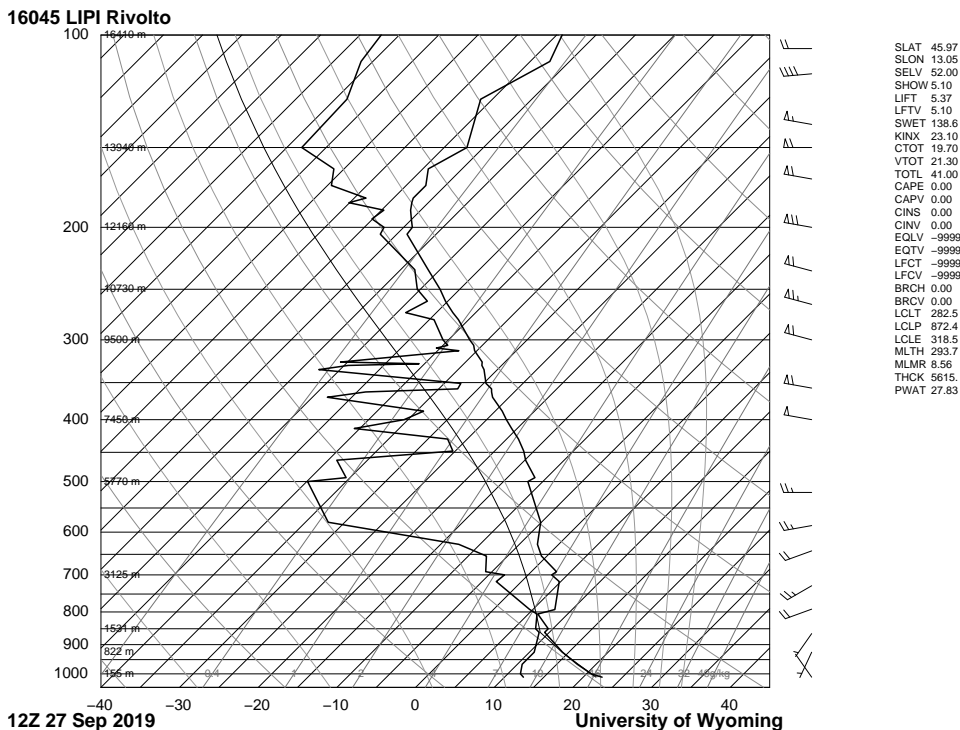
(a) Rivolto (LIPI) sounding.
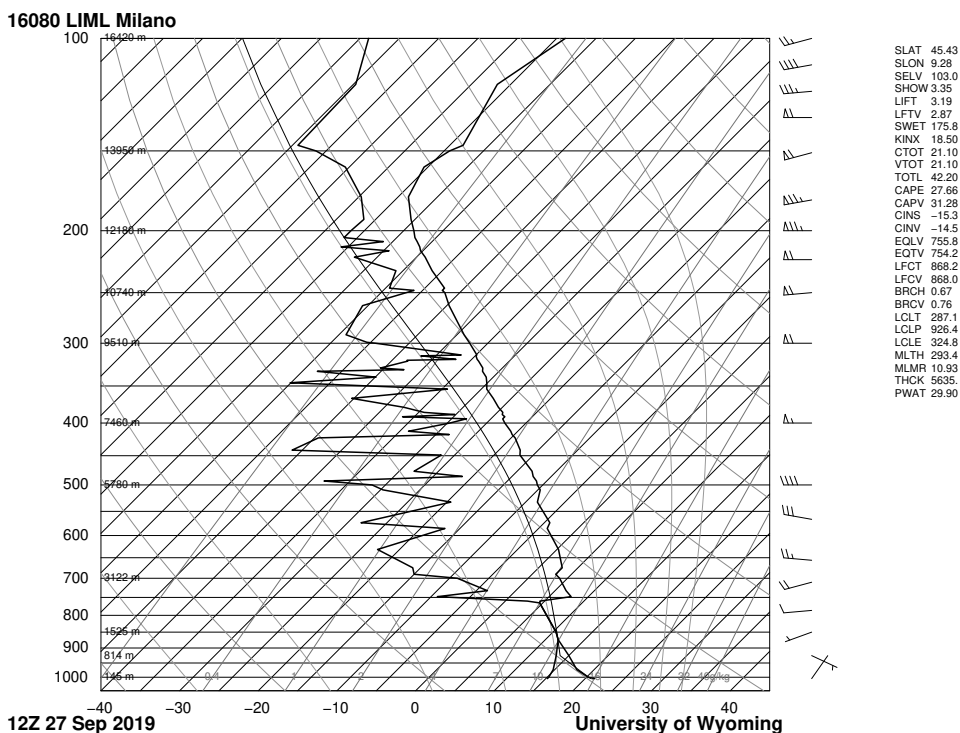
(b) Milano (LIML) sounding.

Figure 2.25: Skew-T log-P diagrams with soundings data on 27 September at 12:00 UTC, for the stations in Rivolto (LIPI) and Milano (LIML). Source: University of Wyoming.

51
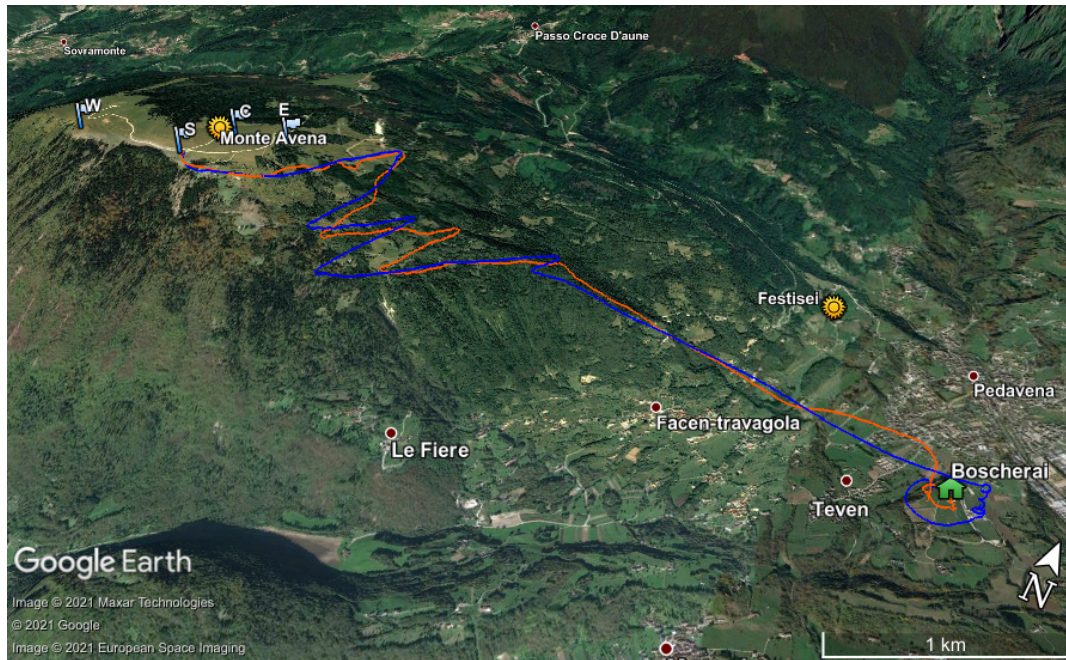
Figure 2.26: Google Earth image of the trajectories of flights #17 (blue) and #18 (orange) performed on 27 September.

2.6.7   30 September

30 September was a mostly cloudy day. Low pressure associated with a warm front interested the measurements areas, with geopotential height about 5740 gpdm (Figure 2.27). The soundings data and diagrams (Figure 2.28) show a stable boundary layer, with zero values of CAPE and a quite low first temperature inversion, at about 1000 m in Rivolto and Milano, and with similar values of the LCL.

Figure 2.29 shows the trajectory of the last flight of the field campaign: after taking off from the E take-off in the early afternoon, the pilot found some modest areas of convective formations over the eastern side of the mountain, and then headed towards the Boscherai landing area.
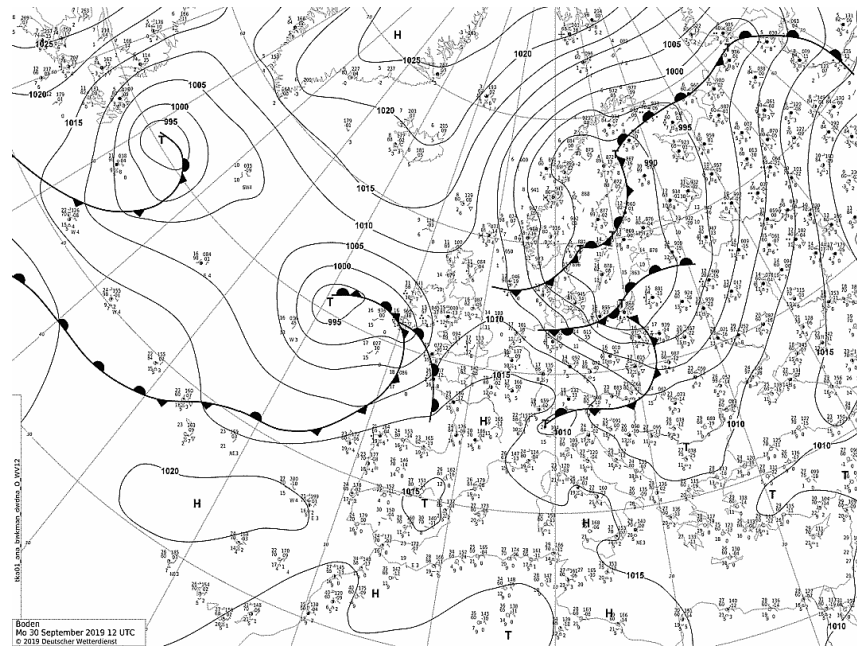
(a) Surface analysis at 12:00 UTC. Source: Deutscher Wetterdienst.
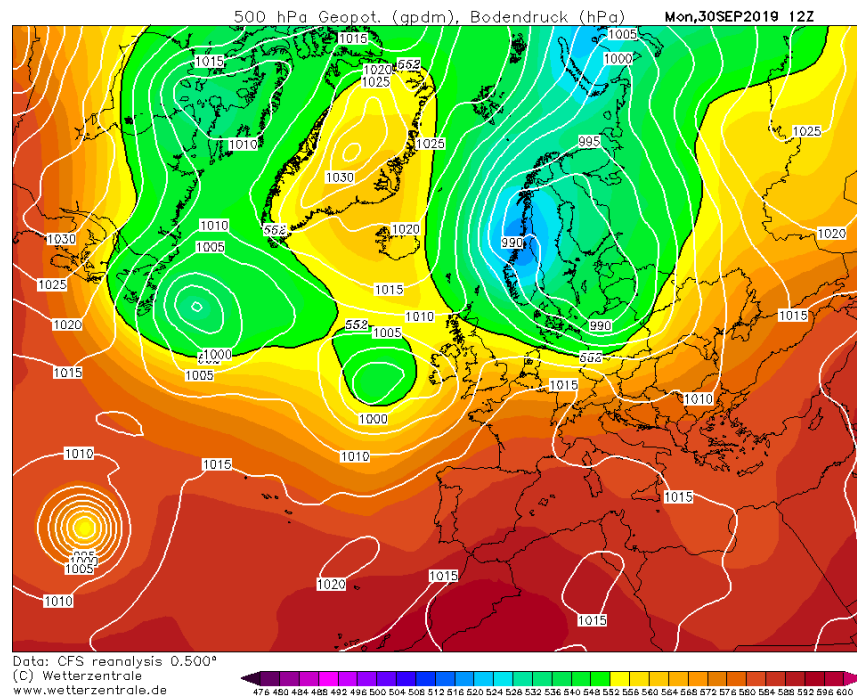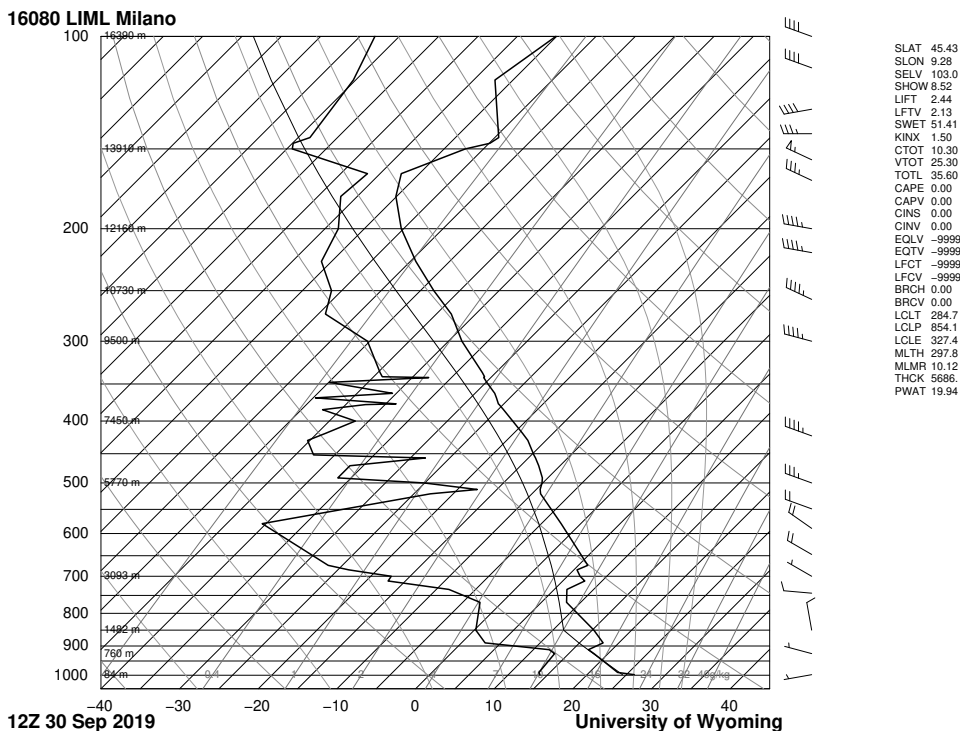

(b) CFS 500 hPa reanalysis at 12:00 UTC. Source: Wetterzentrale.

Figure 2.27: Synoptic charts on 30 September.
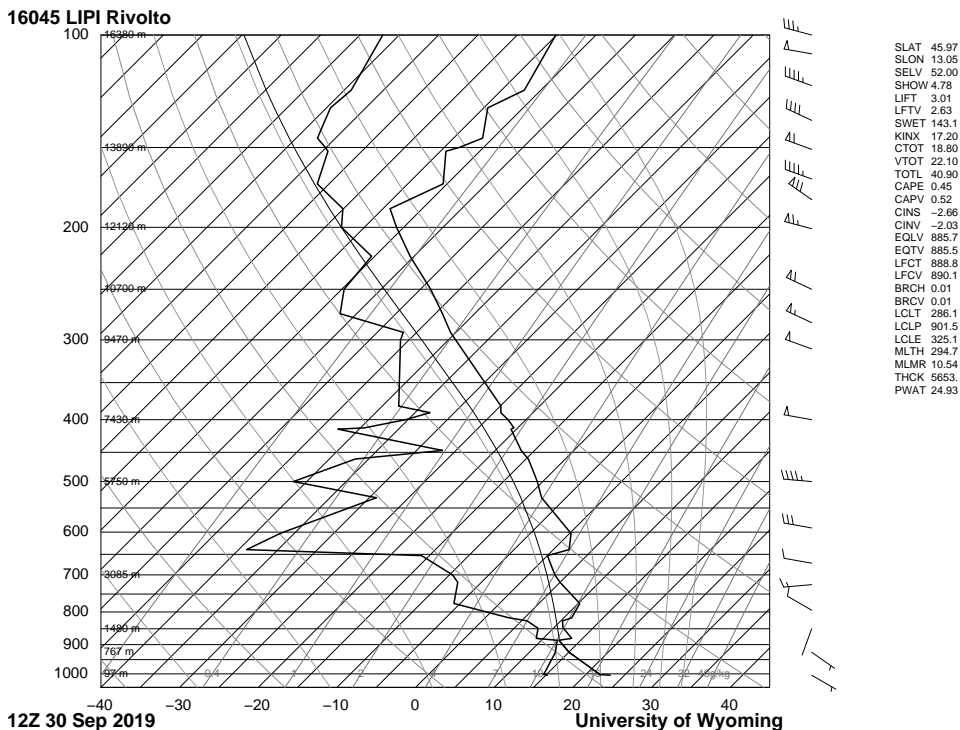
(a) Rivolto (LIPI) sounding.

(b) Milano (LIML) sounding.

Figure 2.28: Skew-T log-P diagrams with soundings data on 30 September at 12:00 UTC, for the stations in Rivolto (LIPI) and Milano (LIML). Source: University of Wyoming.
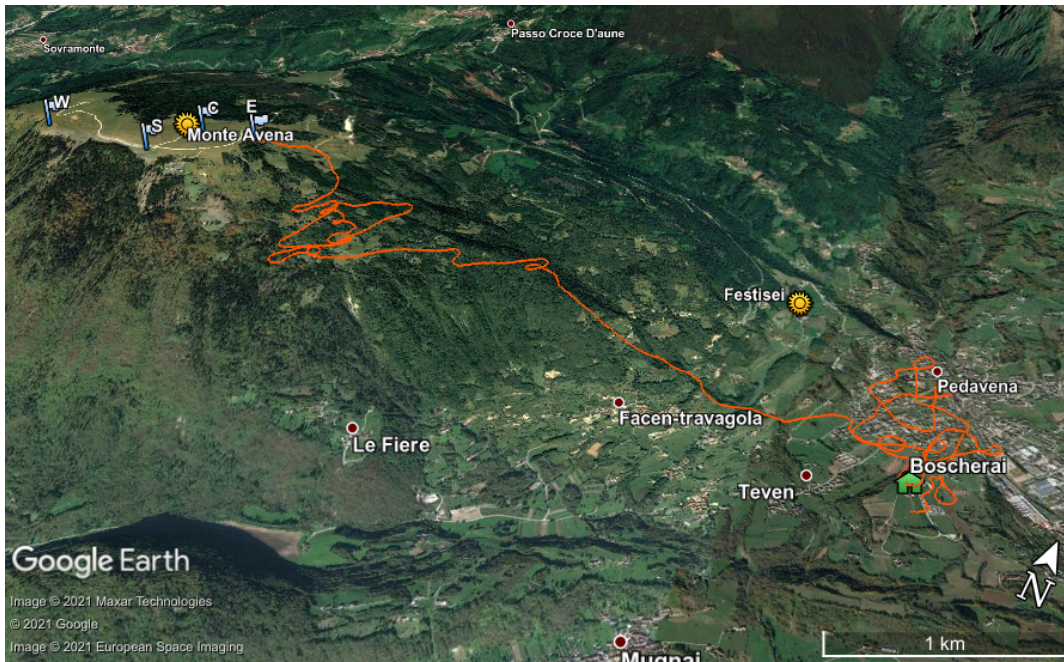
Figure 2.29: Google Earth image of the trajectory of flight #19 (orange) performed on 30 September.

2.7 Summary

The key properties of the paragliding technique, useful to understand the following sections of the thesis, have been introduced. The requirements that the location should satisfy for a successful field campaign involving paragliders have also been explained. The first considered location (Monte Baldo) was discarded, as problems related to accessibility and flight logistics would complicate the organisation of the field campaign.

Instruments able to measure air temperature and relative humidity, atmospheric pressure and wind direction and speed, and that can be easily brought on board the paraglider harness, have been selected.

Measurements were collected on seven days between 17 and 30 September 2019. The chosen location has confirmed expectations about the possibilities for flying and for finding convective structures over the hillsides of Monte Avena, even though not favourable synoptic and local conditions were always present. Three days out of seven were found to display the best flying and convective conditions, and some simultaneous flights were successfully carried out.

In Chapter 4, the three days of 20, 21 and 30 September will be analysed, while in Chapter 3 all the flights will contribute to the analysis of measurements collected by the Compass Srl instruments.

Chapter 3

Post-processing of data from measurements

This chapter presents how data recorded by the couple of instruments C-Pilot and C-Probe (see Section 2.3) are elaborated, describing their positive features along with their drawbacks. The first part of the chapter is dedicated to direct measurements, while in the second part some relevant variables are derived, along with the identification of take-off and landing times.

3.1   GPS measurements

Position and altitude of the pilot are recorded by the GPS module of C-Pilot (see Table 2.1 for datasheet specifications). Files are formatted following the NMEA 0183 standard, which is a proprietary protocol issued by the National Marine Electronics Association for use in boat navigation and control systems, first released in March 1983, and often employed to report recorded data by GPS devices (Betke, 2001; Raymond, 2021). Data are transmitted in the form of *sentences*, each starting with a "$", followed by a *talker identifier* (one or two letters), that specifies the type of the sentence, and a *sentence identifier* (three or more letters), describing the content of the sentence. Data are thus listed in a number of fields separated by commas, followed by an optional *checksum.*

C-Pilot NMEA files basically include Global Positioning System sentences (talker identifier "GP"), containing GPS data, and Proprietary Code sentences (talker identifier "P"), containing data from C-Probe (PCPROBE lines, see Section 3.2). Four types of GP sentences are included in C-Pilot files: GPGGA, GPGSA, GPGSV, GPRMC sentences. The GPGGA lines are the main ones, as they contain the principal GPS data, i.e. UTC time, latitude, longitude and altitude.

In addition to NMEA files, another type of data files is saved by C-Pilot. They are formatted according to the IGC (International Gliding Commission) standard, regulated by FAI (Fédération Aéronautique Internationale) to set standardised rules and specifications for data registered by flight recorders for use in free flight competitions (Fédération Aéronautique Internationale – International Gliding Commission, 2020).

IGC files are not used here, since they basically contain the same information as NMEA files (mainly UTC time, GPS position and altitude) with the only addition of barometric altitude, i.e. altitude estimated from air pressure measurements by the variometer module of C-Pilot, that is compared to GPS altitude in Section 3.1.3.

3.1.1 Time

Coordinated Universal Time (UTC) is the first field in the GPGGA sentences of C-Pilot. Time is henceforward referred to as local time, that is UTC+2.

Some data are missing in the time line of NMEA files during take-off, because of the compass calibration (see Section 2.4), during which the instruments could not record any measurements.

Block average

The acquisition frequency of C-Pilot is 5 Hz, and data are recorded at fractions of second equal to 0.0, 0.2, 0.4, 0.6, 0.8. The acquisition frequency of C-Probe is instead 10 Hz, so for each GGA line more than one PCPROBE lines are recorded. In the following sections, all the presented quantities are block averaged over 1 s, thus reducing the frequency to 1 Hz for all measurements, and the average is associated to the first time of the 1 s interval, that is to the 0.0 fraction of the second.

3.1.2 Horizontal coordinates

Longitude and latitude of the flying paraglider are expressed in the NMEA GPGGA sentences in Degrees Decimal Minutes (DDMM.mmmm).

To work with projected rather than angular geographic coordinates, a conversion to the UTM-WGS84 coordinate system is performed. Thus, the resulting variables are UTM Easting x and UTM Northing y, that correspond respectively to longitude and latitude. They measure the distance in metres of the data point respectively eastward from the central meridian of the 32N zone (corresponding to Italy) and northward from the Equator. Differently from the Equator, that has a Northing value of 0, to the central meridian an Easting value of 500000 m is assigned, and x measures the distance accordingly.

Accuracy of GPS receivers mainly depends on the receiver characteristics (single- or multi-frequency, single- or multi-constellation, Real Time Kinematic (RTK) mode availability (Hodgson, 2020)) and on the visibility and geometry of the constellation of satellites. C-Pilot GPS receivers are low-cost, supporting a single frequency (L1, 1575.42 MHz) and a single satellites constellation (GPS). The horizontal accuracy declared on the datasheet is less than 2.5 m CEP (see Table 2.1).

The C-Pilot GPS receiver supports the DGPS (Differential GPS) mode, that would enhance measurements accuracy thanks to corrections made by comparing the satellites signals received respectively by C-Pilot and by a reference station with known coordinates (Specht et al., 2019). However, it has effectively been exploited in an automatic way only occasionally for a few minutes during the flights, maybe because of satellites visible for a time interval not long enough to allow the differential computation.

The NMEA sentences of types GPGSA, GPGSV and GPRMC contain some parameters related to the satellites constellation in view and to the accuracy of data, including fix validity. The latter is one of the fields of the GPRMC sentences and indicates the validity of each position solution (called "fix"). It can assume an "A" value in case of a valid 3-D fix, or a "V" value reporting a navigation warning: typically, this is related to 2-D fixes, or to fixes which position is unreliable due to poor geometry, or to more variable signal lag induced by lengthened atmospheric transit, or to failure of an elevation test, i.e. the visible satellites are below some fixed elevation (Raymond, 2021). All C-Pilot GPS fixes of flight data have A validity, ensuring an overall basic quality of the signal.

Comparison between the three couples of instruments

Figure 3.1 presents a comparison between the horizontal coordinates measured by the three couples of Compass instruments (a, b and c) during a test data collection carried out on 17 September. The three pairs were located at the Boscherai landing site, resting on the grassy ground, and left recording data between 17:10:00 and 17:52:59. The measurements show elevated variability, greater than the typical 4 m accuracy generally attributed to GPS horizontal measurements in case of excellent conditions of satellites visibility. Also, the three data lines seem to disagree, even if the devices were still and close to each other within few centimetres. UTM Northing (Figure 3.1b) seems also to present increasing latitude values with time, at least for instrument a.

The phenomena that could be responsible for the high fluctuations of the measurements collected by each instrument are signal obstruction (that affects the number and geometry of the satellites in view) and multipath effects (the signal is not received directly but after being reflected) (Hodgson, 2020), caused by the near flight

59

club building and parked vehicles, and maybe by grass to a lesser extent. In the case of data collected during flights, these sources of error are expected to be reduced, as close obstacles are nearly absent. Therefore, the poor behaviour shown in Figure 3.1 is probably not representative of the GPS accuracy during flights.

Two parameters included in NMEA files seem to confirm this hypothesis: DOP and the number of satellites in view. DOP (Dilution Of Precision) is a metric that estimates the quality of the geometric arrangement of available satellites (Hodgson, 2020), on which the accuracy of GPS fixes also depends, and is included in the GPGSA sentences of the NMEA files. Two estimates of DOP can be distinguished: HDOP (Horizontal DOP) and VDOP (Vertical DOP), each related to the horizontal and vertical distribution of satellites. The greater the value of the DOPs, the worse (typically asymmetrical) the satellites configuration and the lower the quality of the received signal. The mean value of HDOP during flights results smaller than for the test data set (respectively 0.94 and 1.51), suggesting that the quality of GPS fixes is greater during flights. Also, the average number of satellites in view, that can be found in the GPGSV sentences and is around 13, is slightly greater in flight data than in test data.

Comparison with personal instruments data

In addition to Compass instruments, GPS data have been recorded also by pilots' personal flight instruments. Since they could not be used always, their data are not available for all the flights: this kind of measurements is not considered in the analysis, but only compared here with Compass data.

A comparison between horizontal coordinates recorded respectively by C-Pilot and the pilot's personal GPS receiver is shown in Figure 3.2. Flight #7, performed on 20 September, has been chosen as an example, but the other flights show similar behaviours. In this case, the personal instrument is an integrated GNSS receiver-altimeter-variometer (leGPSBip produced by Stodeus). Vertical dashed lines represent take-off and landing times, identified as explained in Section 3.3.2. The agreement between C-Pilot coordinates (blue) and those collected by the personal instrument (red) appears satisfactory, as the lines overlap in each part of the flight, suggesting the reliability of C-Pilot measurements, at least in comparison with similar flight instruments.
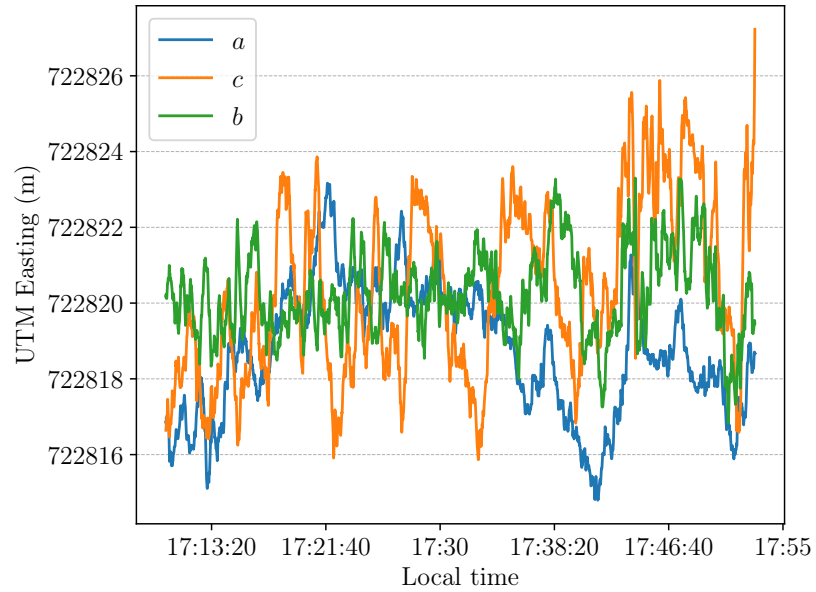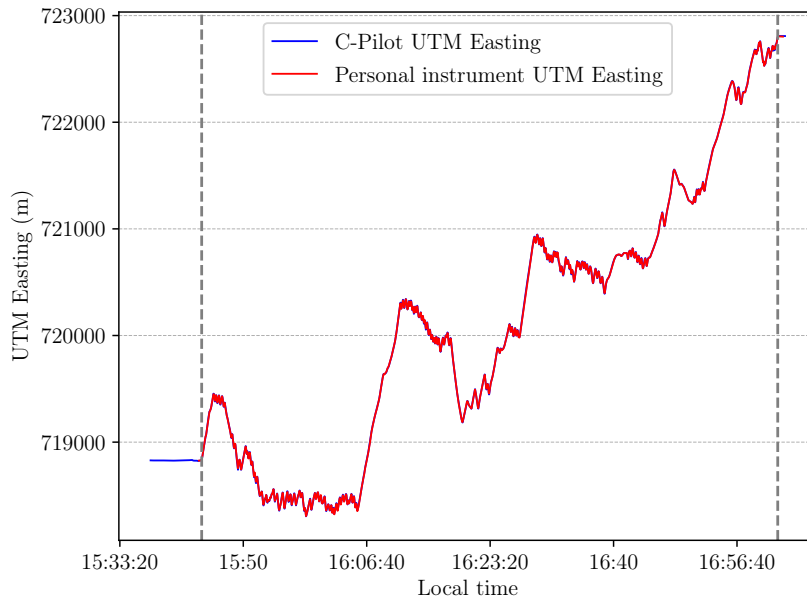
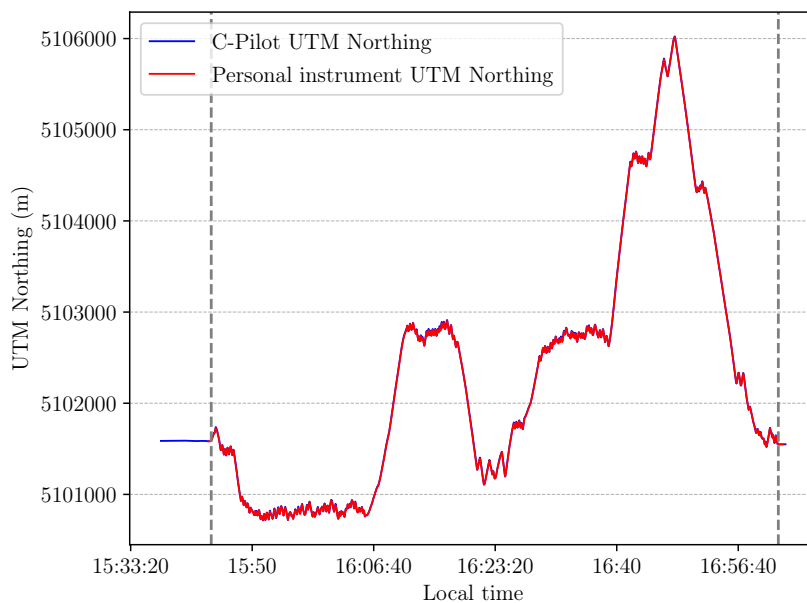(a) Comparison of UTM Easting time series.
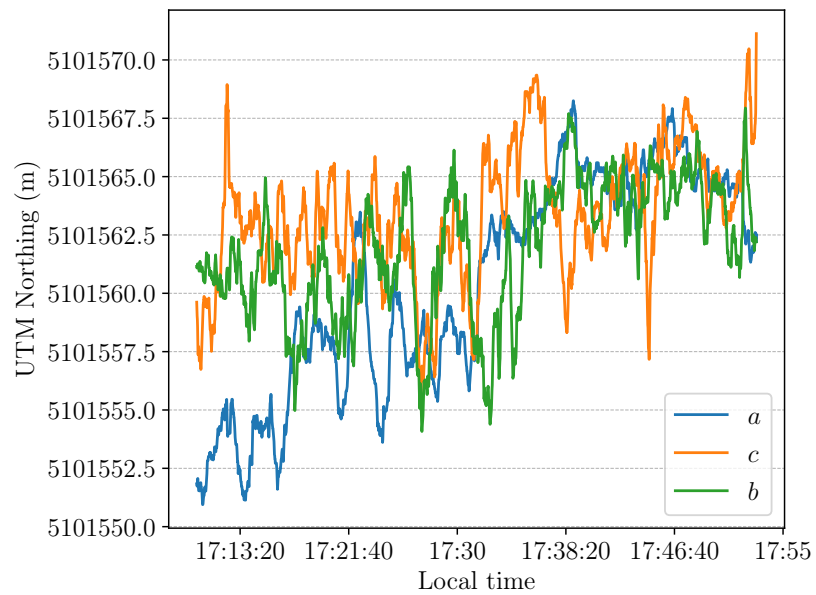
(b) Comparison of UTM Northing time series.

Figure 3.1: Comparison of horizontal coordinates registered by the three couples of instruments (a, b, c) during a test data collection on 17 September.
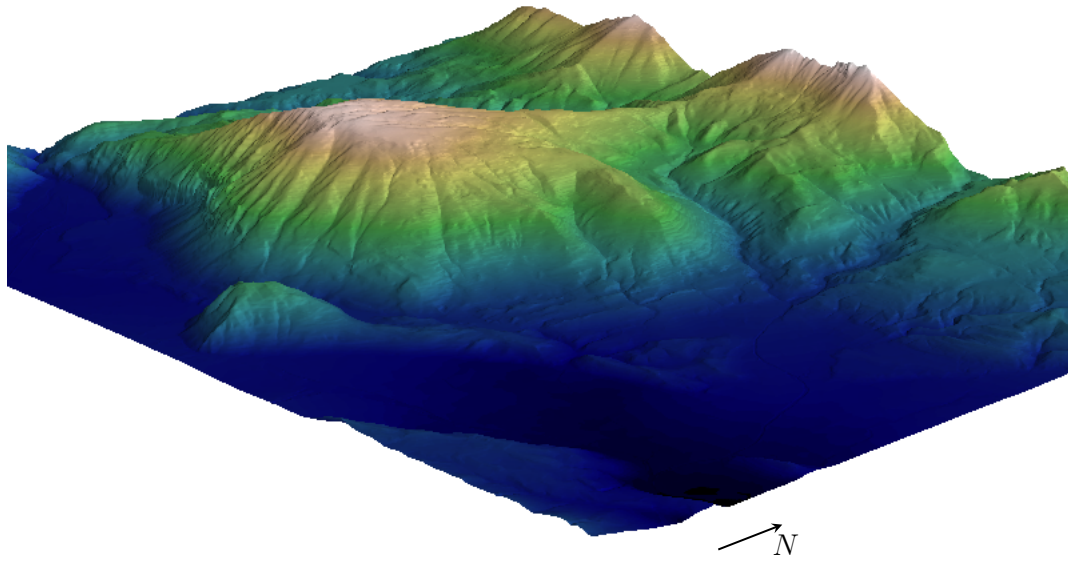
(a) Comparison of UTM Easting time series.
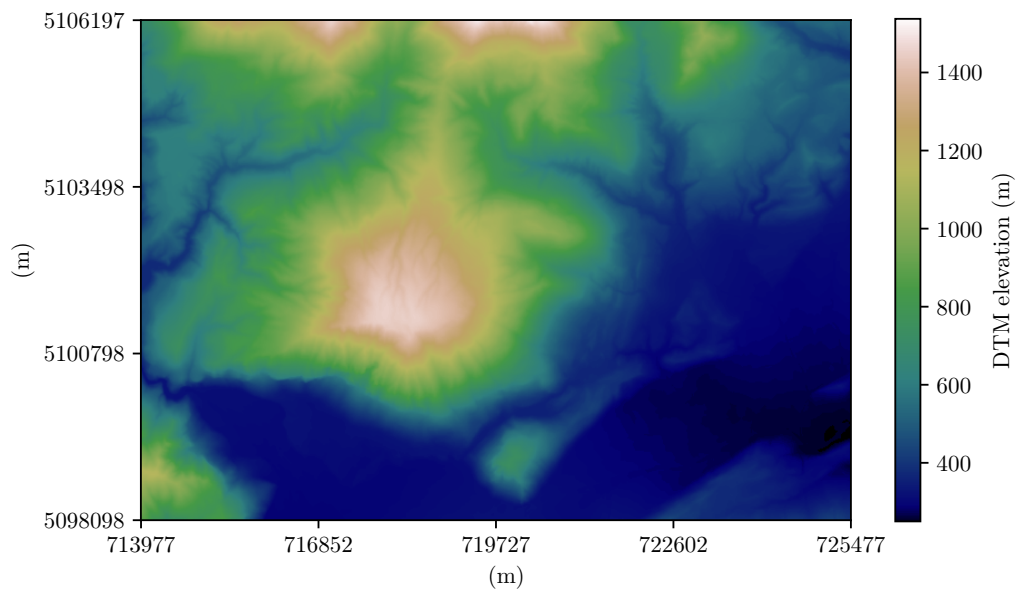

(b) Comparison of UTM Northing time series.

Figure 3.2: Comparison of horizontal coordinates registered by C-Pilot and a personal instrument for flight #7 (20 September).

3.1.3   Altitude

The altitude of the C-Pilot GPS receiver is expressed in the NMEA GPGGA sentences as metres above the mean sea level, identified by the geoid.

(a) 3-D view.

(b) 2-D planimetry view.

Figure 3.3: Visualisation of the Digital Terrain Model centered on Monte Avena, with elevation values mapped to a false-colour scale (legend only on the 2-D representation). Source: Regione del Veneto.

Correction with DTM elevation

At take-off or landing sites the GPS altitude measurement appears sometimes located underground. Hence a correction with elevation values from a Digital Terrain Model (DTM) has been applied. The chosen DTM chosen is a cartographic product of Regione del Veneto (`https://idt2.regione.veneto.it/idt/downloader/download`), centered on the area of interest, with a 5 m resolution. Figure 3.3 depicts, in three and two dimensions, Monte Avena and its surroundings with DTM elevation values mapped to a false-colour scale.

GPS altitude is corrected first at the two sections of data respectively between the beginning of the file (when the instruments are switched on) and the take-off time (hereafter referred to as "take-off section"), and between landing time and the istant the instruments are turned off ("landing section"). During these time intervals (identified as explained in Section 3.3.2), it is imposed that the altitude recorded by the GPS equals the DTM elevation, since the instruments are on the ground or few tens of centimetres above. An average elevation value is computed considering all DTM cells covered by position data points respectively during take-off section and landing section.

During the flight, a linear correction is applied:

$$z_i = z_{or,i} + \Delta z_i, \tag{3.1}$$

where z_i is the corrected value of GPS altitude for each flight point at time i, $z_{or,i}$ is the original altitude value as extracted from the NMEA file, and Δz_i is the correction, computed as:

$$\Delta z_i = mi + q, \tag{3.2}$$

$$m = \frac{\Delta z_{to} - \Delta z_l}{i_{to} - i_l}, \tag{3.3}$$

$$q = \Delta z_{to}, \tag{3.4}$$

where:

- Δz_{to} and Δz_l are the differences between mean DTM elevation and mean GPS altitude at the take-off and landing sections respectively;

- i is the index for time points: $i = 1, 2, 3, ..., i_{to}, ..., i_l, ..., i_f$ with i_{to}, i_l and i_f respectively the indices of take-off, landing and final time points. They are equally spaced by 1 s (see Section 3.1.1).

Two examples of the correction method for two different flights (#15 on 26 September and the second part of #11 on 24 September – see Section 2.6.4) are shown in Figure 3.4: Figure 3.4a and Figure 3.4b display the linear behaviour of

Δz_i, along with the values of Δz_{to} and Δz_l highlighted in blue, while the original (red) and corrected (black) GPS altitudes are compared in Figure 3.4c and Figure 3.4d. Vertical dashed lines mark the take-off and landing times respectively.

In the case of flight #4 (20 September), since C-Pilot shut down unexpectedly before landing (see Section 2.6.2) and thus landing time is missing, the correction has not been applied and the flight is not considered for further analysis.

For all the other flights, the altitude mentioned hereafter is the corrected GPS altitude, unless differently specified.

(a) Additive factor of the GPS altitude correction for flight #15 (26 September).

(b) Additive factor of the GPS altitude correction for flight #11 – part 2 (24 September).

(c) Original and corrected GPS altitude time series of flight #15 (26 September).

(d) Original and corrected GPS altitude time series of flight #11 – part 2 (24 September).
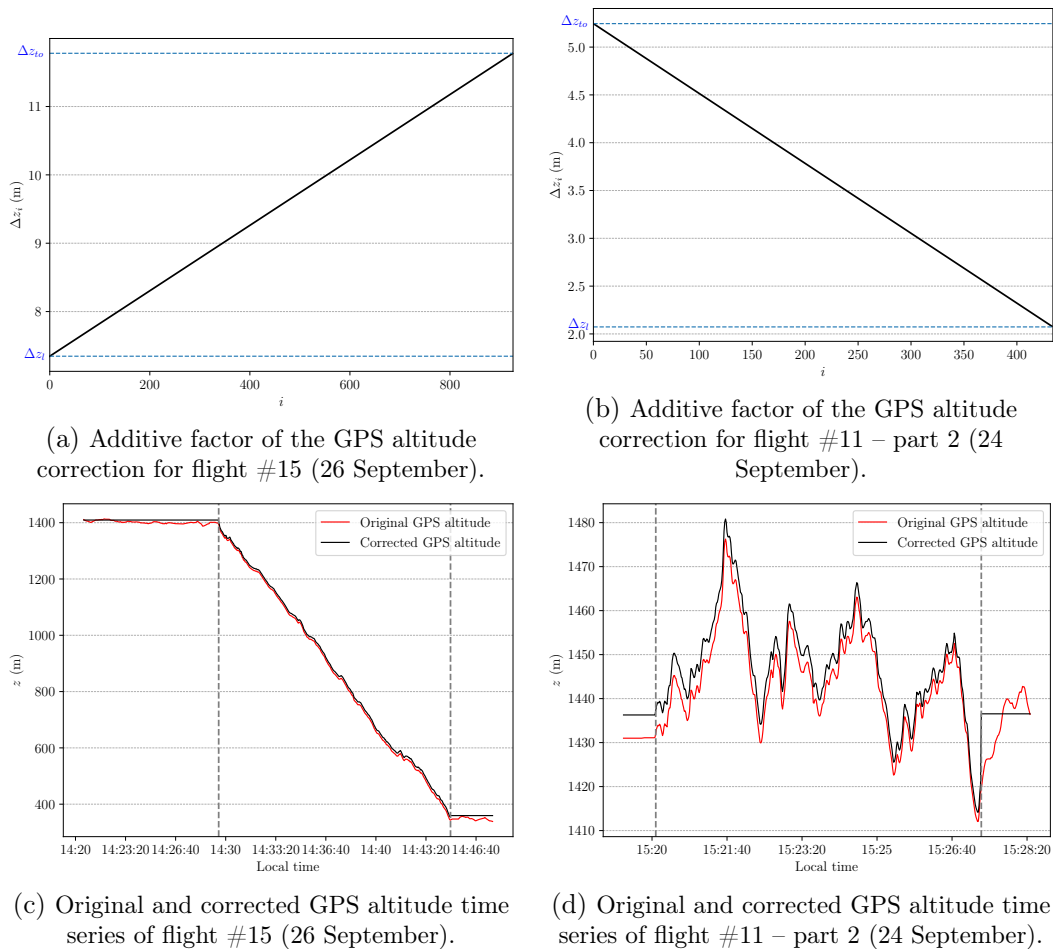
Figure 3.4: Example plots illustrating the GPS altitude correction and its results.

Comparison between the three couples of instruments

As for horizontal coordinates, a comparison between the altitude data measured by the three couples of Compass instruments, from the test data set on 17 September, is presented in Figure 3.5. Here GPS altitude is directly extracted from NMEA files and is not corrected with DTM elevation. The horizontal grey line indicates the

mean elevation (358.8 m) at the average position computed from the UTM Easting and UTM Northing corresponding values of Figure 3.1.

Similarly to horizontal coordinates, the agreement between the three instruments in recording altitude is low, with a quite clear drift towards lower values. Again, this probably does not well represent the accuracy of GPS receivers for flight data. As HDOP, also VDOP presents smaller values during flights rather than for the test data set (1.52 and 1.98 respectively), and the same potential sources of errors could act, probably to a greater extent since the vertical coordinate is generally more susceptible, compared with horizontal coordinates, to occluded signals and to weak satellites configurations (Hodgson, 2020). In general, accuracy on the measurement of altitude is to be expected lower than on the measurement of horizontal position.
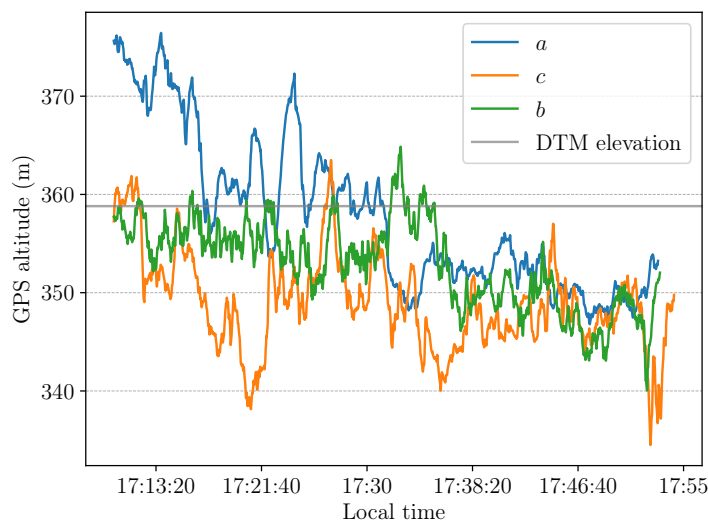
Figure 3.5: Comparison of time series of altitude registered by the three couples of instruments (a, b, c) during the test data collection on 17 September.

Comparison with other types of altitude

Figure 3.6a shows an example comparison between all altitude measurements available, again for the example flight #7 (20 September). Orange and purple lines refer to barometric altitude recorded respectively by the C-Pilot variometer (and contained in the IGC file) and by leGPSBip variometer. As for other flights, these measurements are not useful for the present work, since barometric altitude, in order to match IGC requirements, is calibrated according to the ICAO (International Civil Aviation Organization) International Standard Atmosphere, that defines standard temperature and pressure at sea level and assumes a standard constant temperature vertical profile, thus not representing the actual state of the atmosphere. For this reason, barometric altitude has instead been computed starting from pressure values measured by C-Probe and making use of the hypsometric equation (Section 3.3.5),

and is displayed in green. The agreement between C-Pilot GPS altitude (blue), computed barometric altitude (green) and GPS altitude by the personal instrument (red) appears satisfactory, as in the case of horizontal coordinates (Figure 3.2), suggesting the good choice of C-Pilot as GPS receiver.

A zoom in a limited section of the flight (Figure 3.6b), between 15:52:17 and 15:54:17 reveals also that even the smallest oscillations, of the order of $1\,\mathrm{m}$, are detected by all these three independent measurements, although with different intensities in some cases: they are likely real oscillations and random noise is not present or at least not relevant. Therefore, C-Pilot has proved to have high sensitivity, being able to recognise limited variations in GPS altitude, that agree well with other altitude estimates. Data for other flights are similar to these, confirming that C-Pilot GPS measurements, both for horizontal coordinates and for altitude, are reliable, at least to this extent.
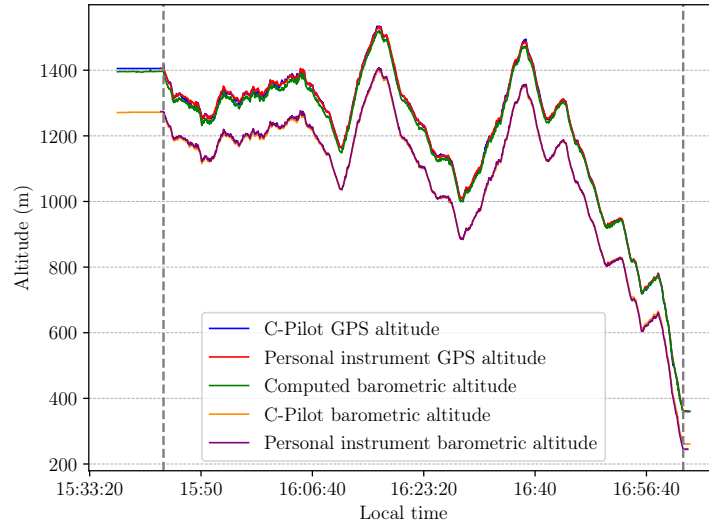
(a) Comparison between all the five altitude estimates.
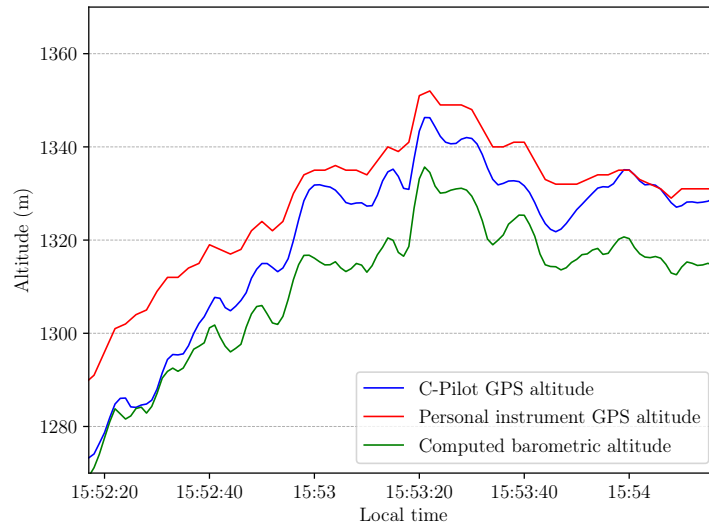
(b) Zoomed comparison between GPS altitude recorded by C-Pilot
and by the pilot's personal instrument, and computed barometric
altitude.

Figure 3.6: Comparison of different altitude estimates time series for flight #7 (20 September).

3.2   C-Probe measurements

Quantities measured by C-Probe are recorded in sentences that are trasmitted to C-Pilot via BlueTooth pairing, and they appear as Proprietary Code sentences (PCPROBE lines) in the NMEA files. PCPROBE strings contain the measures of temperature, relative humidity, pressure, differential pressure, the three components of acceleration and the four quaternions of orientation. Major space is given here to temperature, relative humidity and pressure, whereas differential pressure

and the quaternions are involved in the wind computation in Section 3.3.7.

3.2.1   Temperature and relative humidity

Temperature and relative humidity are recorded by the thermo-hygrometer SHT21 by Sensirion AG (see Table 2.1) and data are contained in the PCPROBE lines of NMEA files.

Adjustment time after take-off

The response time of temperature and relative humidity measurements is declared by the constructor to be between 5 s and 30 s for temperature, and about 8 s for relative humidity (see Table 2.1). Response time, as well as accuracy, is likely to worsen if C-Probe is not correctly positioned on the harness cockpit, not receiving an appropriate airflow (see Section 2.3), or if the instrument is left still under the sun. While the correct positioning condition has probably been satisfied in most cases (the four air intakes have been placed outside the cockpit), during take-off procedures C-Probes have been exposed to sunlight for several minutes before and after the installation on the cockpit, and waiting for the proper condition to fly (see Section 2.4). This has caused a overheating of the sensors, leading to overestimation of temperature and underestimation of relative humidity for the first minutes of the flights.

Figure 3.7 presents an example of this behaviour for flight #1, performed on 17 September. Data collected during the take-off and landing sections (see Section 3.3.2) are not displayed here. The section of the profile highlighted in green shows corrupted values of temperature T (Figure 3.7a) and relative humidity RH (Figure 3.7b) after the take-off, due to the overheating effect. The "adjustment" time needed for the airflow ventilation to correctly act and for the temperature of the electronics to stabilize, considered equal for T and RH, is estimated as the time interval between take-off time and the time point when the profile assumes an ordinary behaviour with increasing/decreasing temperature/relative humidity with decreasing height. This point is located at the boundary between the green and the black sections and for flight #1 the adjustment time results to be about 114 s. Unfortunately, as this effect produces not reliable T and RH values, the first (green) part of all the flights, until the restoration of ideal measuring conditions, has been removed and not considered for further analysis.

Table 3.1 contains the adjustment times evaluated as above for all the 19 flights, resulting between 52 s (flight #11 – part 3) and 294 s (flight #6). For flights #11 and #12, that are divided in three and two sub-flights respectively, as explained in

Section 2.6.4, the adjustment time is referred to the last sub-flight.

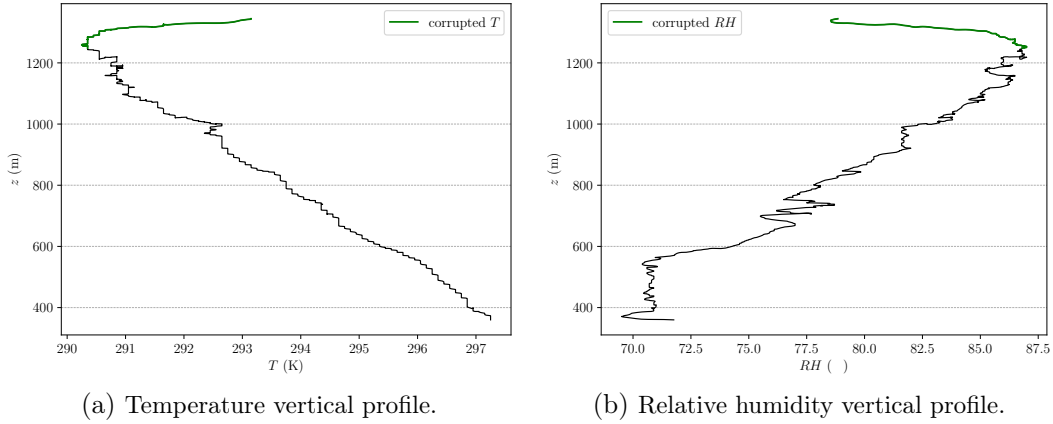(a) Temperature vertical profile.   (b) Relative humidity vertical profile.

Figure 3.7: Temperature and relative humidity vertical profiles for flight #1 on 17 September, showing the slow adjustment time during the first minutes of the flight.

Comparison between the three couples of instruments

As for GPS data, a comparison between temperature and relative humidity measurements collected by the three couples of instruments for the test data set on 17 September afternoon (17:10:00–17:52:59) is presented in Figure 3.8. The degree of agreement is quite satisfactory: since the C-Probe instruments were in this case not in motion, thus without the ventilation necessary to properly operate, the distance between the three lines is considered acceptable. The trend shared by the three instruments is to be associated with the decreasing air temperature and increasing relative humidity as sunset approaches (as confirmed by surface weather stations data, not shown here).

(a) Comparison of T time series.   (b) Comparison of RH time series.
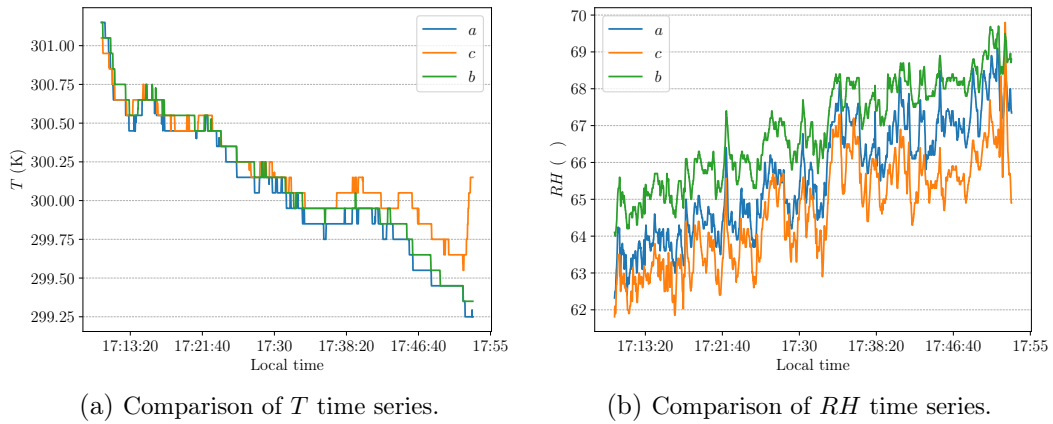
Figure 3.8: Comparison of temperature and relative humidity registered by the three couples of instruments (a, b, c) during the test data collection on 17 September.

flight	date	take-off	instruments	adjustment time (s)
1	17/09/2019	15:18, E	a	114
2	17/09/2019	15:18, E	c	61
3	17/09/2019	15:18, E	b	61
5	20/09/2019	13:00, S	c	143
6	20/09/2019	13:01, S	a	294
7	20/09/2019	15:44, C	a	180
8	20/09/2019	16:12, E	c	79
9	21/09/2019	12:37, E	c	150
10	21/09/2019	12:37, E	a	183
11	24/09/2019	15:00, W	c	52
12	24/09/2019	15:09, W	a	159
13	24/09/2019	15:37, W	b	166
14	26/09/2019	14:19, S	a	116
15	26/09/2019	14:30, S	c	162
16	26/09/2019	16:32, S	a	119
17	27/09/2019	14:51, S	a	169
18	27/09/2019	14:51, S	c	137
19	30/09/2019	15:27, E	c	91

Table 3.1: Adjustment times of temperature and relative humidity related to the overheating effect of the C-Probe thermo-hygrometer at take-off, for all the 19 flights.

3.2.2   Pressure

Pressure is measured by the barometer MS5611-01BA01 manufactured by Measurement Specialties (see Table 2.1) and its values are extracted from the PCPROBE lines of the NMEA files.

Not valid pressure data

Unfortunately, pressure data recorded by instruments b and c seem to be corrupted and are not valid for further analysis. An example is shown in Figure 3.9b for flight #3 with instrument b, compared for reference to flight #1 with instrument a (Figure 3.9a), performed simultaneously on 17 September. Corresponding GPS altitude time series are presented below (Figure 3.9d and Figure 3.9c). Vertical dashed lines mark take-off and landing times (see Section 3.3.2). Both pilots followed a simple glide from take-off to landing, as evident by the altitude time series, but flight #3 presents an unexpected trend of pressure data, in contrast to the expected trend of flight #1. The causes of this behaviour are not clear; they could be related to physical problems of the devices, or maybe to recording disruption.

Some attempts to correct not valid data have been made. In this case, the horizontal segments of data present expected values, comparable with those of flight #1. The correction has been applied to the two corrupted sections: the second long

section (large negative values) has been translated upward to join the first short one (large positive values), then the entire section has been scaled taking as fixed points the valid extremes of the horizontal segments. The result has turned out to be fair, but the artificiality of the procedure and the extra manipulation needed for other more problematic cases has led to follow a different strategy: to replace data collected by instruments b and c, pressure has been computed via the hypsometric equation making use of GPS altitude measurements (see Section 3.3.6).

(a) Pressure time series of flight #1 (17 September), with instrument a.

(b) Pressure time series of flight #3 (17 September), with instrument b.

(c) GPS altitude time series of flight #1 (17 September).

(d) GPS altitude time series of flight #3 (17 September).
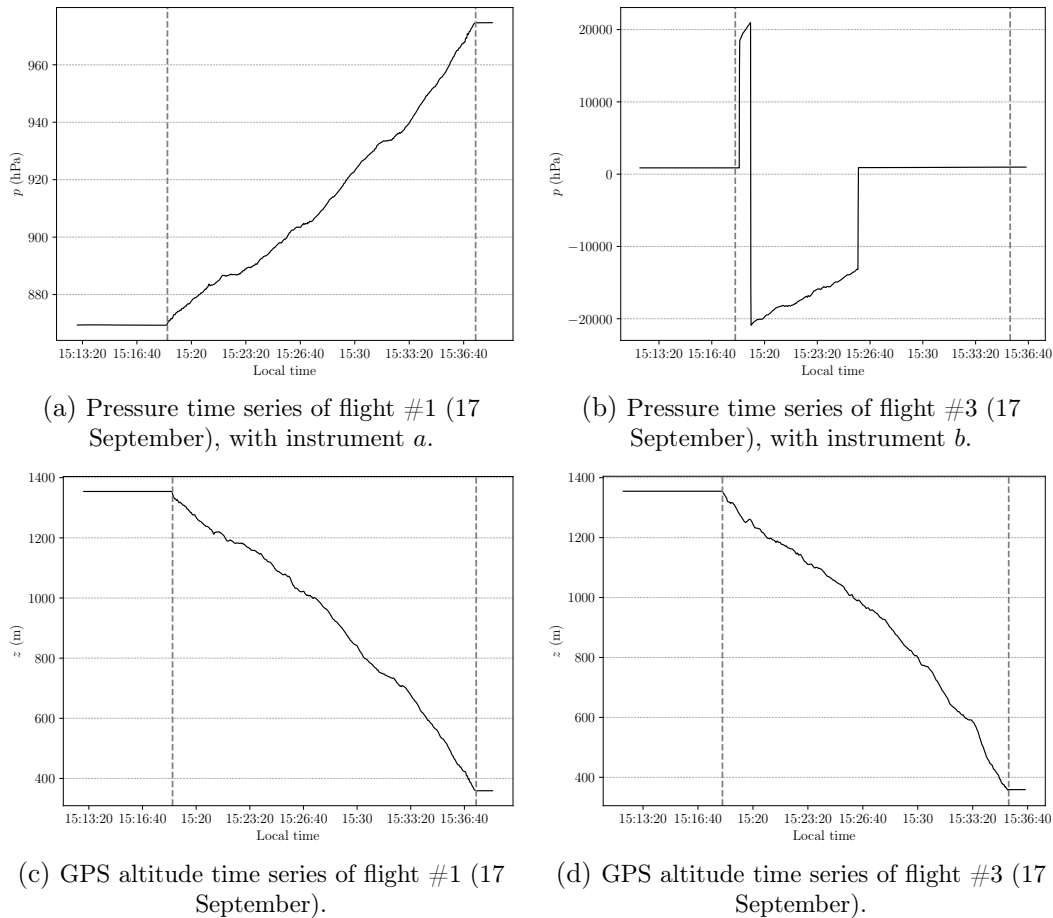
Figure 3.9: Example of not valid pressure data for flight #3 (panel b), compared to flight #1 (panel a) and to corresponding GPS altitudes.

Comparison between the three couples of instruments

For the sake of completeness, also for pressure a comparison between data collected by the three couples of instruments for the test data set on 17 September is shown in Figure 3.10. This is not very significant, since during flights, as seen before, both instruments b and c give not valid measurements and they are thus replaced by computed pressure (Section 3.3.6). Anyway, the agreement between the values of the three C-Probe instruments is quite good, but they show rather different trends

with time.
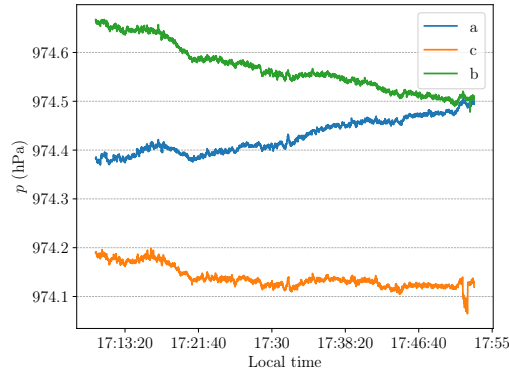
Figure 3.10: Comparison of pressure time series registered by the three couples of instruments (a, b, c) during the test data collection on 17 September.

3.3   Derived quantities

In the following sections, the quantities later used for the analysis of Chapter 4 are presented, along with the calculations necessary to derive them.

From GPS data, ground speed is computed, allowing to determine take-off and landing times. Thermodynamic variables describing the state of the air and obtained from the Pitot tube measurements are mixing ratio, virtual potential temperature and dew-point temperature. Also, barometric altitude is computed and, due to the lack of reliable pressure data for the two couples of instruments b and c, an estimate of pressure is given too. Finally, wind computation is discussed.

3.3.1   Ground speed

Ground speed of the flying paraglider, that is its speed with respect to ground (differently from airspeed, i.e. speed with respect to air – see Section 3.3.7), is computed making use of GPS position and altitude data, with a fourth-order centered difference approximation of the first derivative:

$$GS_{x,i} = \frac{-x_{i+2} + 8x_{i+1} - 8x_{i-1} + x_{i-2}}{12} \tag{3.5}$$

$$GS_{y,i} = \frac{-y_{i+2} + 8y_{i+1} - 8y_{i-1} + y_{i-2}}{12} \tag{3.6}$$

$$GS_{z,i} = \frac{-z_{i+2} + 8z_{i+1} - 8z_{i-1} + z_{i-2}}{12}, \tag{3.7}$$

where $GS_{x,i}$, $GS_{y,i}$, $GS_{z,i}$ are respectively the components of ground speed $\boldsymbol{GS}$ at each flight point at time i (the time points being equally spaced by $1\,\mathrm{s}$, see

Section 3.1.1). They are defined in the standard meteorological coordinate system (x, y, z): positive eastward (x), northward (y) and upward along the local vertical (z) (Metzger et al., 2011). The local vertical, i.e. the direction of gravity, can be considered constant over the whole limited flight area. x, y and z are respectively UTM Easting, UTM Northing, and GPS altitude.

For $i = 2$ or $i = i_f - 1$, with $i = 1, 2, 3, ..., i_f$, the previous equations reduce to a second-order centered difference approximation of the first derivative. For the x component (the same for y and z):

$$GS_{x,i} = \frac{x_{i+1} - x_{i-1}}{2}. \tag{3.8}$$

Similarly, for $i = 1$ or $i = i_f$, a first-order forward or backward difference approximation is used:

$$GS_{x,i} = \frac{x_{i+1} - x_i}{1} \quad (i = 1), \qquad GS_{x,i} = \frac{x_i - x_{i-1}}{1} \quad (i = i_f). \tag{3.9}$$

Horizontal ground speed is then computed from the vector summation rule as:

$$GS_{h,i} = \sqrt{GS_{x,i}^2 + GS_{y,i}^2}. \tag{3.10}$$

Ground speed is used to identify take-off and landing times (see Section 3.3.2), as well as ascent and descent sections of the flights (see Section 4.1). It is also involved in wind computation (Section 3.3.7).

3.3.2   Take-off and landing times identification

NMEA files start when the instruments are turned on at the take-off site, and end some time after the pilots has landed. As in the present work interesting data are mainly those collected while flying, take-off and landing times have been evaluated in order to separate airborne from surface measurements.

Since one of the variables that change most noticeably from take-off to flight and from flight to landing is the ground speed, take-off and landing times are respectively identified as the first and last time points i of the NMEA file of each flight satisfying $GS_{h,i} > 10 \, \mathrm{km \, h^{-1}} \, (2.8 \, \mathrm{m \, s^{-1}})$.

The threshold has been chosen on an observational basis, comparing the time series of ground speed (example in Figure 3.11a) with that of original GPS altitude (example in Figure 3.11b). Take-off and landing times are shown as vertical dashed lines. It can be seen that the choice of the threshold allows to correctly identify take-off and landing times, as they mark the times when altitude changes from nearly constant to decreasing for take-off, and conversely for landing.

The $10\,\mathrm{km\,h^{-1}}$ threshold is appropriate for all flights except those performed on 24 September, when a stronger wind was blowing at the take-off (see Section 2.6.4). In this case, a lower threshold for the take-off time is more suitable, because the speed necessary for taking off is lower in the presence of a strong opposite wind (see Section 2.1). A take-off threshold of $6\,\mathrm{km\,h^{-1}}$ ($1.7\,\mathrm{m\,s^{-1}}$) has thus been chosen in these cases. For sub-flights 1 and 2 of flight #11 and for sub-flight 1 of flight #12, as landing took place on the take-off site (see Section 2.6.4), the same $6\,\mathrm{km\,h^{-1}}$ threshold has been used for landing too.

For the analysis shown in Chapter 4, only data collected during flights have been further analysed, while those recorded before take-off and after landing have been discarded. Plots will therefore include only flight sections, starting from take-off and ending at landing.
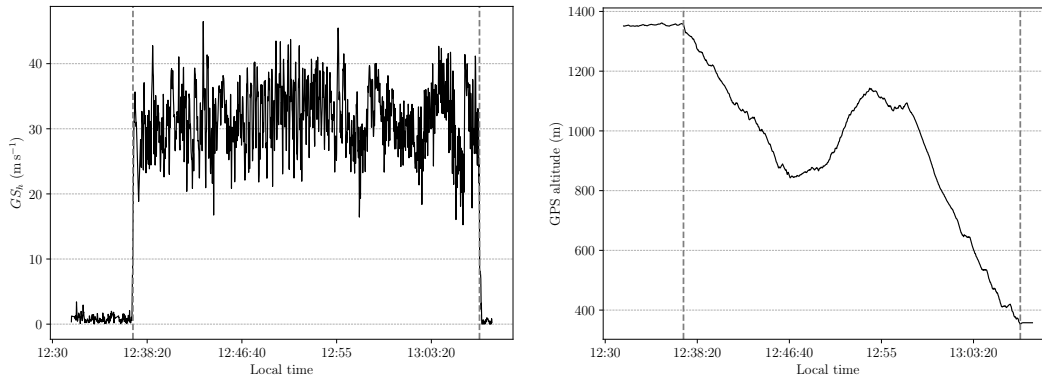
(a) Horizontal ground speed time series of flight #10 (21 September).

(b) Original GPS altitude time series of flight #10 (21 September).

Figure 3.11: Example plots showing the identification of take-off and landing times, marked as vertical dashed lines.

3.3.3 Water vapour mixing ratio

Water vapour mixing ratio is computed for each flight point as:

$$q = \epsilon \cdot \frac{e}{p - e}, \tag{3.11}$$

where water vapour partial pressure e is computed from:

$$e = \frac{e_s RH}{100} \tag{3.12}$$

and the saturation water pressure e_s is computed as suggested in Ambaum (2020):

$$e_s = e_{s0} \left(\frac{T_0}{T}\right)^{(c_{pl}-c_{pv})/R_v} \exp\left(\frac{L_0}{R_v T_0} - \frac{L}{R_v T}\right), \tag{3.13}$$

where the latent heat of evaporation of water at temperature T is:

$$L = L_0 - (c_{pl} - c_{pv})(T - T_0). \tag{3.14}$$

In the above equations, p, RH and T are the atmospheric pressure, relative humidity and air temperature measured for each flight point (in the case of pressure, it is measured or computed – see Section 3.3.6), whereas the constants are:

- $\epsilon = R_d/R_v$, with $R_d = 287.0\,\mathrm{J\,kg^{-1}\,K^{-1}}$ (gas constant of dry air) and $R_v = 461.52\,\mathrm{J\,kg^{-1}\,K^{-1}}$ (gas constant of water vapor);

- $T_0 = 273.16\,\mathrm{K}$ is a reference temperature, chosen as the triple-point temperature of water;

- $e_{s0} = 611.655\,\mathrm{Pa}$ is the saturation water pressure at the triple-point T_0;

- $L_0 = 2.501 \times 10^6\,\mathrm{J\,kg^{-1}}$ is the latent heat of evaporation of water at the triple-point T_0;

- $c_{pl} - c_{pv} = 2180\,\mathrm{J\,kg^{-1}\,K^{-1}}$ is the difference between the specific isobaric heat capacity of liquid water and water vapour.

3.3.4 Virtual potential temperature

Virtual potential temperature is computed for each flight point as:

$$\theta_v = T_v \left(\frac{p_0}{p}\right)^k, \tag{3.15}$$

where the virtual temperature T_v is:

$$T_v = \frac{T}{1 - \frac{e}{p}(1 - \epsilon)}. \tag{3.16}$$

T and p are the temperature and pressure measured for each flight point (in the case of pressure, it is measured or computed – see Section 3.3.6), e is the partial water vapour pressure as in Equation 3.12 and ϵ is defined as before. In addition:

- $p_0 = 1000\,\mathrm{hPa}$ is a reference pressure;

- $k = R_d/c_p$, with $c_p = 1004\,\mathrm{J\,kg^{-1}\,K^{-1}}$ (specific isobaric heat capacity of dry air) and R_d as above.

3.3.5   Barometric altitude

As an alternative to the direct GPS measurement, altitude can be computed by means of the hypsometric equation in differential form, making use of data from pressure measurements (for this reason it is called barometric altitude):

$$z_i = z_{i+1} - \frac{R_d}{g_0} T_{v_i} \frac{p_i - p_{i+1}}{p_i}, \tag{3.17}$$

where:

- z_i is the barometric altitude for each flight point i;

- p_i, T_{v_i} are the pressure (measured or computed – see Section 3.3.6) and the virtual temperature at flight point i;

- $g_0 = 9.81\,\mathrm{m/s^2}$ is the mean value of the acceleration of gravity at the Earth surface.

Computation starts from landing, that corresponds to the last time i, and proceeds backwards to take-off, corresponding to the first time i. Mean elevation from the Digital Terrain Model at the landing section (i.e. corrected GPS altitude at landing, see Section 3.1.3) is imposed as first z_i.

Valid pressure data are available only for instruments a (see Section 3.2.2), thus computation of barometric altitude gives reliable results only in this case.

3.3.6   Computed pressure

Pressure data, as seen in Section 3.2.2, included corrupted values for instruments b and c. Therefore, a derivation of pressure from Equation 3.17 making use of the measured GPS altitude data has been carried out:

$$p_i = p_{i+1} \cdot \frac{R_d T_{v_{i+1}}}{R_d T_{v_{i+1}} + (z_i - z_{i+1})g_0}, \tag{3.18}$$

where:

- p_i is the computed pressure for each flight point i;

- z_i is the GPS altitude measured at flight point i;

- $T_{v_{i+1}} = \frac{T_{i+1}}{1 - \frac{e_{i+1}}{p_{i+1}}(1-\epsilon)}$ is used instead of T_{v_i}, as T_{v_i} depends itself on pressure at time i, and is computed as in Section 3.3.4.

As for barometric altitude, computation starts from landing (last i) and goes back to take-off (first i). The first value of pressure is imposed as the average

pressure after landing until the end of file (that is between 57 s and 168 s according to the flight) for flights with instruments a or with instruments b and c with valid data after landing. For corrupted values of pressure at landing, concerning four flights, the average p is derived from the contemporary flight with instrument a on the same day, even if landings happened at slightly different times (between 1 and 12 min difference).

For flight #8, performed on 20 September with instrument c, pressure data at landing are corrupted and no other simultaneous flights have been conducted, thus a reference starting pressure is missing. This flight is therefore not considered for further analysis.

For data collected by instruments a, original pressure measurements are used for further analysis, while pressure computed as above is used hereafter to replace not valid data of instruments b and c.

To assess the quality of the pressure computation algorithm, Figure 3.12a shows the time series of original valid pressure (red) and computed pressure (black) of flight #1 (17 September), with a clear satisfying agreement. Computed pressure for flight #3, replacing the original one in Figure 3.9b, is presented in Figure 3.12b.

(a) Comparison between the original and the computed pressure time series of flight #1 (17 September), with instrument a.

(b) Computed pressure time series of flight #3 (17 September), with instrument b.
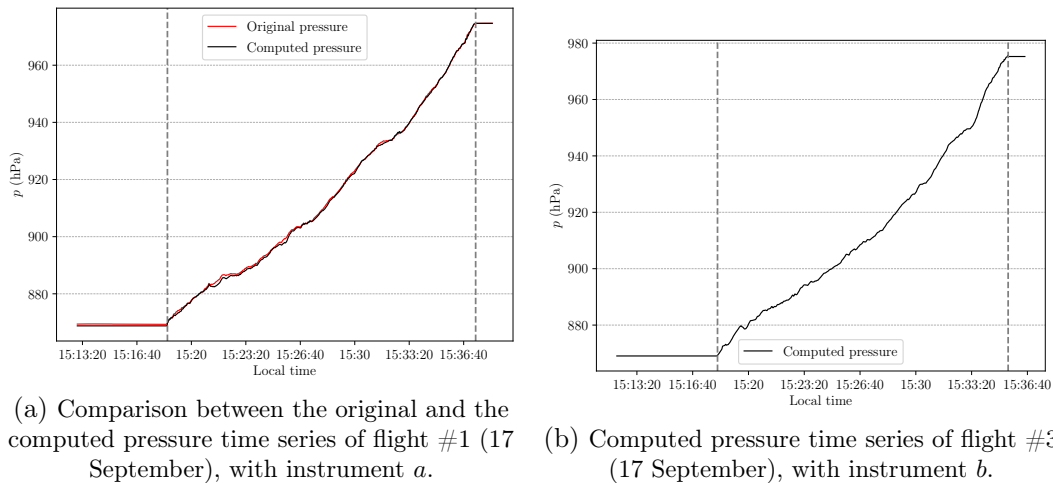
Figure 3.12: Results of the pressure computation algorithm for flights #1 (panel a) and #3 (panel b).

3.3.7 Wind

The computation of wind speed and direction during straight trajectories is possible by means of the differential pressure data measured by the Pitot tube and the orientation in space measured by the three-axis gyroscope and the magnetic compass of C-Probe. During turning trajectories, a different approach is necessary

and the patent-pending algorithm developed by Compass Srl provides the horizontal components of wind velocity.

Unfortunately, as seen below, both the strategies have turned out to give not valid results, not compatible with the expected wind in the area of measurements. The most probable reason for this is a not corrected calibration of the compass of C-Probe, that affects the estimate of the True Airspeed direction (see below). Only the vertical component of wind is not affected by this, as it is computed in a different way.

Wind vector and True Airspeed computation

The 3-D wind vector ($\boldsymbol{w}$) can be computed as the vector difference between the velocity of the paraglider with respect to ground ($\boldsymbol{GS}$) and the velocity of the paraglider with respect to air ($\boldsymbol{TAS}$), as in Metzger et al. (2011), Cho et al. (2011) and van den Kroonenberg et al. (2008):

$$\boldsymbol{w} = \boldsymbol{GS} - \boldsymbol{TAS}. \tag{3.19}$$

The vector components are defined with respect to the standard meteorological coordinate system (Section 3.3.1). The three components of $\boldsymbol{GS}$ are computed as described in Section 3.3.1, while $\boldsymbol{TAS}$ is derived starting from differential pressure measurements.

The modulus of $\boldsymbol{TAS}$ is computed from Bernoulli's equation as:

$$TAS = \sqrt{\frac{2\Delta p}{\rho(z, T_v)}}, \tag{3.20}$$

where Δp is the differential pressure measured by the Pitot tube and contained in the PCPROBE lines of NMEA files. Air density $\rho(z, T_v)$ is computed from the ideal gas law for wet air as:

$$\rho(z, T_v) = \frac{p(z)}{R_d T_v(p(z))}, \tag{3.21}$$

where p is the pressure measured by instruments a, or the pressure computed for instruments b and c as in Section 3.3.6. In the latter case, Equation 3.21 explicitly becomes, for each flight point at time i:

$$\rho_i = p_{i+1} \cdot \frac{1}{R_d T_{v_{i+1}} + (z_i - z_{i+1})g_0}. \tag{3.22}$$

The relative speed with respect to air is referred to as TAS, standing for True Airspeed, as aircrafts airspeed in aviation contexts is usually distinguished into four different estimates: Indicated AirSpeed (IAS), Calibrated Airspeed (CAS), Equiva-

lent Airspeed (EAS) and True Airspeed (TAS) (International Virtual Aviation Organisation, 2021). If ρ is taken as the standard value of air density at mean sea level ($1.225\,\mathrm{kg\,m^{-3}}$), then Equation 3.20 represents the modulus of IAS, that is the airspeed usually read on aircrafts flight instruments, directly deriving from Pitot tube measurements. TAS is an improvement of the IAS estimates as it takes into account the dependence of air density on altitude and temperature. CAS and EAS represent other kinds of adjustments with respect to IAS, as they consider instruments position and installation errors (CAS), and air compressibility errors (EAS). CAS correction is generally important only for an angle between the Pitot tube and the relative airflow greater than that possibly present in our case; EAS correction is relevant only for airspeeds much more elevated than those reached by a paraglider. Thus, here only TAS has been considered.

As visible in Figure 3.13, showing an example of TAS and IAS time series for flight #1 (17 September), TAS (black line) is greater than IAS (blue line), since for densities lower than the sea level density a greater speed is necessary to get the same lift on the wing. Vertical dashed lines identify take-off and landing times, as determined from ground speed data in Section 3.3.2. They mark a discontinuity between the two ranges of airspeed values in the plot: lower values respectively before and after take-off and landing times, and higher values in between, confirming the quality of the procedure for take-off and landing identification. Since during take-off and landing sections the instruments were essentially still, airspeed in the lower range is an estimate of the wind intensity at take-off and landing that, in this case, is about $1\,\mathrm{m\,s^{-1}}$ (light air in the Beaufort scale). However, this has to be considered a rough estimate, since the orientation of the probe at take-off and landing was variable and not always directed into the wind. The higher range values, about $9\,\mathrm{m\,s^{-1}}$, give instead the airflow speed during flight.

Horizontal wind

True Airspeed components are derived considering the orientation of C-Probe in the standard meteorological coordinate system, as the direction of the computed True Airspeed is that of the Pitot tube of C-Probe (the black tube in Figure 2.5b). Since the paraglider's horizontal airspeed is generally much greater than its vertical airspeed, TAS as computed in Equation 3.20 is considered approximately as the modulus of the horizontal True Airspeed.

Anyway, the vertical component cannot be obtained by decomposition of $\boldsymbol{TAS}$, as the gyroscope of C-Probe gives the pitch angle (angle with respect to the vertical) of the white body of C-Probe and not of the black tube. The tube, as explained in Section 2.3, is bent to be aligned to the relative airflow and the benting angle could vary and was not measured. The vertical component is thus derived in a different
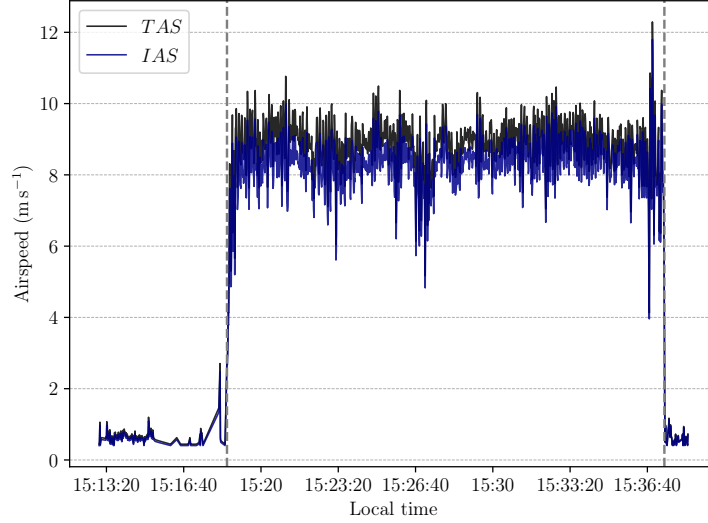
Figure 3.13: Comparison between TAS and IAS time series of flight #1 (17 September).

way (see below).

The inertial measurement unit of C-Probe provides the orientation of the probe itself in quaternions format. A description of quaternions and their relation with Euler angles can be found in De Marco and Coiro (2017). The four components of the quaternion of orientation $(q0, q1, q2, q3)$ are contained in the PCPROBE lines of NMEA files. To decompose the 2-D True Airspeed vector into its x and y components, the Euler angle of heading ψ is required and is derived as:

$$\psi = \pi + \text{atan2}[2(q_0 q_3 + q_1 q_2), -1 + 2(q_2{}^2 + q_3{}^2)].\tag{3.23}$$

The atan2 function is a two-argument arctangent function: $\text{atan2}(y, x)$ returns the arctangent of y/x in radians, belonging to the appropriate quadrant according to the signs of the arguments (De Marco and Coiro, 2017).

Since C-Probe magnetic compass gives the orientation of the device with respect to Magnetic North, ψ is the angle formed by the True Airspeed vector in the 2-D plane, positive clockwise with respect to the Magnetic North direction – see Figure 3.14. Thus, a correction needs to be applied in order to obtain the heading ψ_{TN} with respect to Geographic (True) North, that is the direction of the y-axis of the chosen coordinate system. A value of 3.44° E is assumed as mean magnetic declination δ for the area and days of the field campaign, obtained from the International Geomagnetic Reference Field (IGRF) 13th generation model (Alken et al., 2021).

The horizontal True Airspeed is then decomposed into its x and y components as:

$$TAS_x = TAS \sin \psi_{TN},\tag{3.24}$$

$$TAS_y = TAS \cos \psi_{TN}, \tag{3.25}$$

where $\psi_{TN} = \psi + \delta$ is the heading angle referred to True North.

Horizontal wind components are then obtained from Equation 3.19 as:

$$w_x = GS_x - TAS_x, \tag{3.26}$$

$$w_y = GS_y - TAS_y. \tag{3.27}$$
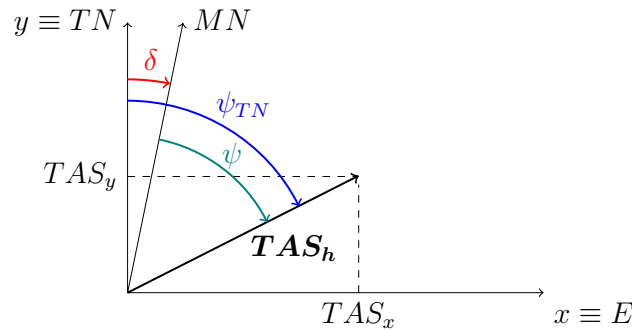
Figure 3.14: Difference between True North (TN) and Magnetic North (MN) directions in the 2-D standard meteorological coordinate system, with heading angles ψ and ψ_{TN} and magnetic declination δ. δ is not to scale.

The algorithm illustrated above is valid only during straight trajectories, due to the delay between the ground speed direction, tangent to the trajectory, and the heading with respect to ground, that takes place when the pilot changes direction from a straight line to a curve. In this cases, especially for spiral trajectories in thermals, the patent-pending algorithm by Compass Srl, that also includes the automatic calibration system of C-Probe, has been considered. As details of the algorithm are subject to a Non-Disclosure Agreement, only its results can be presented.

Figure 3.15a presents an example result for the computation of horizontal wind during a section of straight trajectory of flight #1 (17 September), while Figure 3.15b shows the corresponding TAS vector. Wind and TAS vectors are represented as black arrows on a 2-D horizontal plane, while the trajectory followed by the pilot with respect to the ground is highlighted in grey. Ground speed vectors are not shown, but they coincide with the tangent to the trajectory at each data point. DTM contour lines of the underneath slope are also added to the plot each 20 m.

It is evident that the wind estimates are not valid, as they change direction frequently and according to the direction of trajectory. This is explained observing

TAS: it appears always tilted to the left of the trajectory direction. This would mean that the paraglider, even if following the grey trajectory with respect to the ground, is pointed according to *TAS* direction, thus flying with a very pronounced and not likely drift. Instead, the probable cause for this is an incorrect calibration of the magnetic compass. This operation was not perfectly carried out all the times, mainly because of the number of procedures and checks necessary to correctly turn on and pair C-Probe and C-Pilot, and of the limited time the pilots could dedicate to the flight for work or personal commitments. As a consequence, the heading measured by the compass is probably biased and the decomposition of *TAS* produces not reliable x and y components. A possible second source of error could be related to a not appropriate installation procedure of the instrument on the cockpit, or to successive movements of the Pitot tube after take-off, that would compromise the correct alignment with the relative airflow affecting the modulus of *TAS*.

The behaviour of wind vectors where the trajectory describes turnings or circles appear not valid, for the reason explained above. Other flights present similar problems.

Figure 3.16a shows instead an example result of horizontal wind computation using the Compass algorithm for a section of spiral trajectory of flight #9 (21 September). Figure 3.16b and Figure 3.16c present the corresponding wind direction and intensity time series, compared to surface weather stations data (Monte Avena, Festisei, Feltre – see Section 2.5). Wind direction, i.e. the direction from which it originates, is expressed as the angle in degree with respect to (True) North.

Here, the direction of wind vectors seems reasonable, at least in the central part of the spiral trajectory, where it follows the maximum slope of the hillside, perpendicular to the countour lines. Also, direction looks in fair agreement with surface stations data (except for Feltre station, located in the valley, quite distant from Monte Avena). However, wind intensity appears much greater than that registered by surface stations. This difference is not justified considering that wind measurements are collected not at surface but in flight, since height over ground, computed as the difference between GPS altitude and DTM elevation, is on average only $\sim 150\,\mathrm{m}$ in the selected flight section.

Because of the mentioned problems, horizontal wind measurements computed as above are not used for further analysis. An alternative instrument for the measurement of the wind speed and intensity may be a five-hole probe, sometimes adopted for airborne measurements from gliders or aeroplanes, as in Metzger et al. (2011).

An alternative algorithm for the derivation of horizontal wind velocity in thermal sections, estimated as wind drift, could be developed adapting Allen and Lin (2007)

and Ultsch (2012) (see Section 1.4).
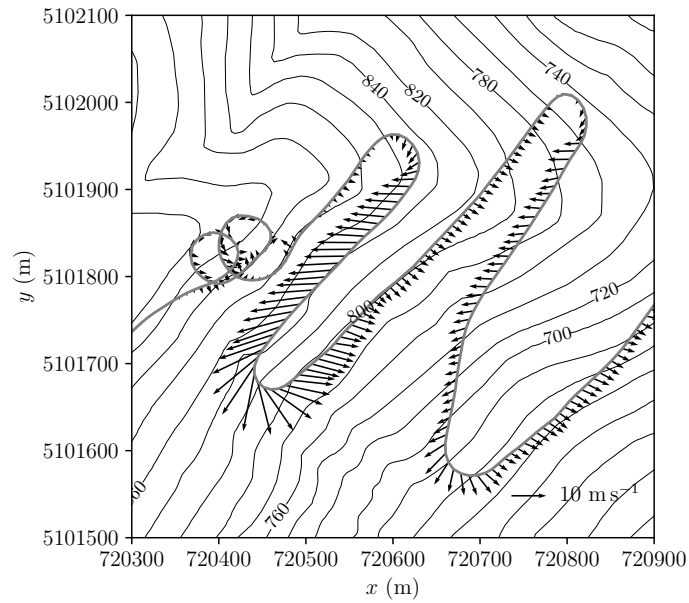
(a) Section of trajectory with the 2-D wind vector.
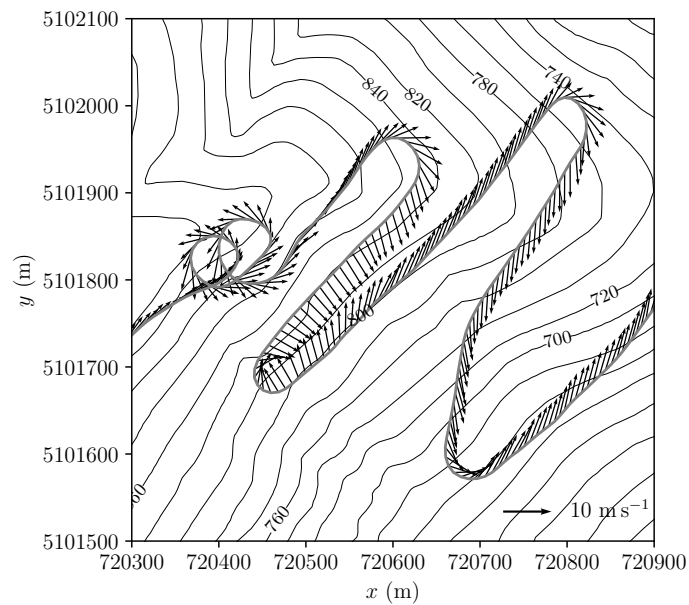
(b) Section of trajectory with the 2-D TAS vector.

Figure 3.15: Results of the horizontal wind computation algorithm for a straight trajectory section of flight #1 (17 September). DTM contour lines are displayed each 20 m.
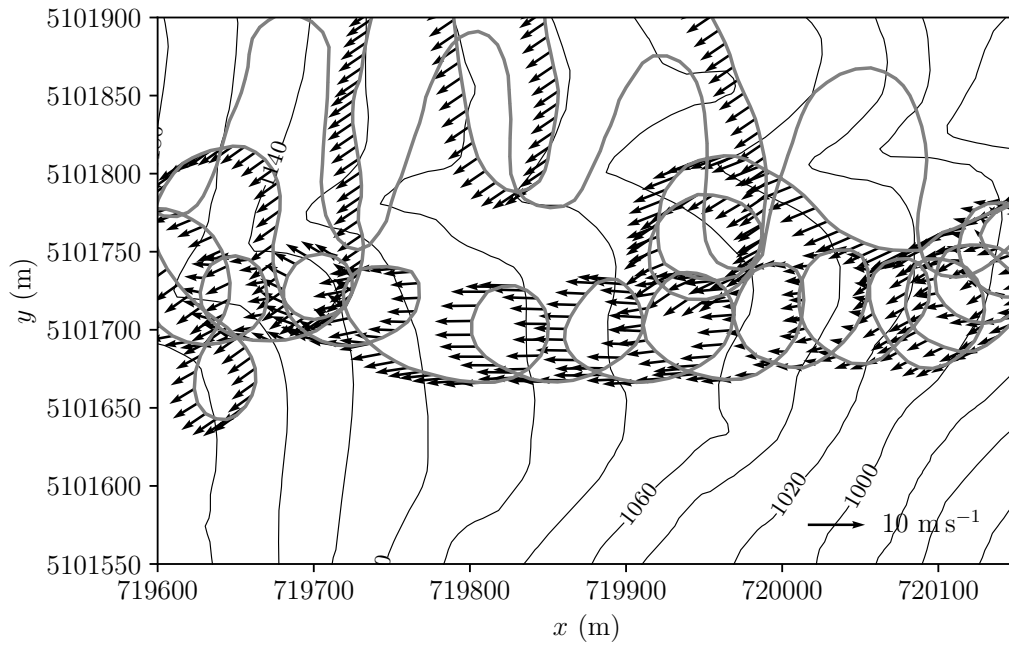
(a) Section of trajectory with the 2-D wind vector. DTM contour lines are displayed each 20 m.
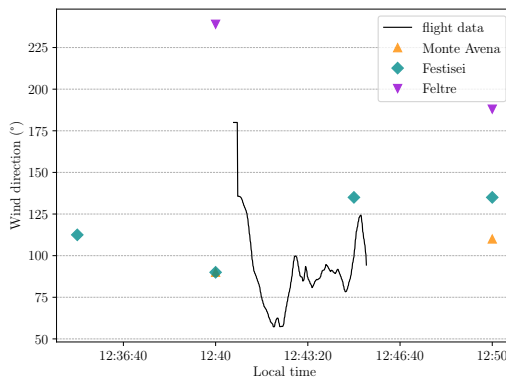
(b) Wind direction time series with surface weather stations data.
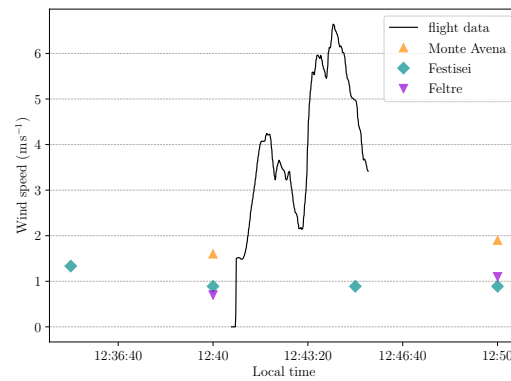
(c) Wind intensity time series with surface weather stations data.

Figure 3.16: Results of the horizontal wind computation algorithm by Compass Srl for a spiral trajectory section of flight #9 (21 September).

Vertical wind

As explained above, the vertical component of the wind w_z is derived with a different method:

$$w_z = GS_z - v_{sink}, \tag{3.28}$$

where GS_z is the vertical ground speed (Equation 3.7), whereas v_{sink} is the average sink rate of the paraglider, i.e. the wing average vertical speed with respect to air. As explained in Section 2.1, v_{sink} is always negative (i.e. it is a downward vertical velocity) to allow lift generation for gliding. The sink rate depends mainly on the horizontal airspeed, which is regulated by acting on the brakes. This relationship is usually displayed in a diagram called *speed polar curve* or *hodograph*, with values of True Airspeed on the x-axis and of sink rate on the y-axis. Generally, the polar curve depends on the wing type and performance properties. The sink rate can also change for sudden or special manoeuvres, thus the pilots were asked to limit them as much as possible, conducting a smooth flight, in order not to take into consideration such variability.

Figure 3.17 displays four hodographs for four different types of wing, obtained from data provided by Compass Srl. B, C and D are wing classes listed in order of increasing performance and skills required by the pilot, following the classification of the European Standard EN 926. CCC is a competition paraglider class, specifically designed to fulfil the requirements set by CIVL (Commission Internationale de Vol Libre). Pilots have flown with EN A (the beginners class, not shown), B or C wings.

The three data points available for each curve correspond to three characteristic airspeed values: with released brakes, with half speed bar, and with full speed bar, in order of increasing speed. The speed bar is a foot control attached to the risers, that increases the wing's speed by changing its angle of attack (i.e. the angle between the wing chord – the line connecting the leading to the traling edge of the wing profile – and the relative airflow). The pilots never used the speed bar, so that the first point speed (released brakes) is in our case probably the highest speed during the flight. Lower speeds are reached for example while thermalling, as brakes are kept pulled to a certain extent. The average value of TAS for each flight, computed between take-off and landing times, varies between $6.7\,\mathrm{m\,s^{-1}}$ (flight #18, 27 September) and $9.3\,\mathrm{m\,s^{-1}}$ (flight #2, 17 September). This interval is shaded in grey in Figure 3.17. Flights performed on 24 September have not been considered here: for the peculiarity of the wind conditions on that day (Section 2.6.4), TAS is on average lower (till $4.0\,\mathrm{m\,s^{-1}}$) than typical flight speeds, and this day of measurements is excluded in the analysis of thermal structures of Chapter 4.

The average of the TAS measured values has been considered here for the evaluation of the range of airspeed during flights, even if they could be affected, as seen

above, by errors in the correct alignment of C-Probe with the relative airflow. However, an alternative measurement for the airspeed is not available, the average TAS is typical of the wings the pilots flew with and it probably presents minor errors than the instantaneous TAS.

The sink rate v_{sink} has been assumed as a constant value for all the flights, equal to the average of the three hodograph points available in the grey area, that is $-1.2\,\mathrm{m\,s^{-1}}$. In order to account for the errors derived by the limited number of data in the grey area, an uncertainty value equal to $\frac{1}{3}$ of v_{sink} has been assigned to it and plays a role in the classification of updraft and downdraft points in Chapter 4.

An example of the time series of the resulting w_z is shown in Figure 3.18 (grey) for flight #10 (21 September). Since at take-off and landing sections the sink rate is not defined, w_z is computed and shown only during the flight. In order to filter out noise in the original signal, a moving window average of w_z (black), centered on 10 data points that correspond to 10 s, has been computed. Hereafter, the vertical wind w_z is always the average, unless differently specified.
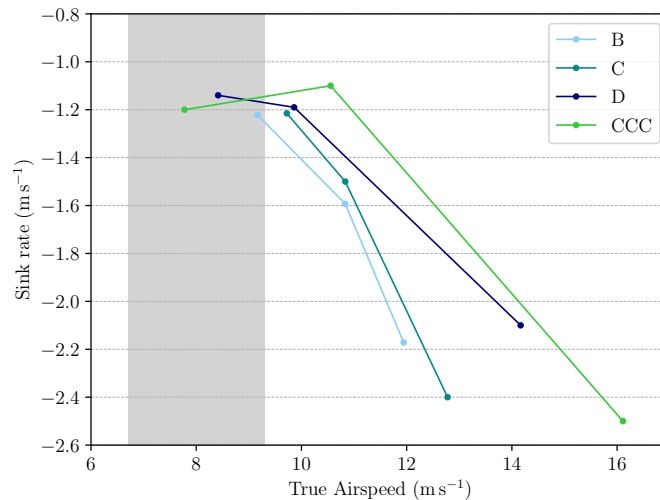
Figure 3.17: Hodograph curves for four classes of paraglider wings. Source: Compass Srl. The grey area corresponds to the interval of mean TAS of all the performed flights.
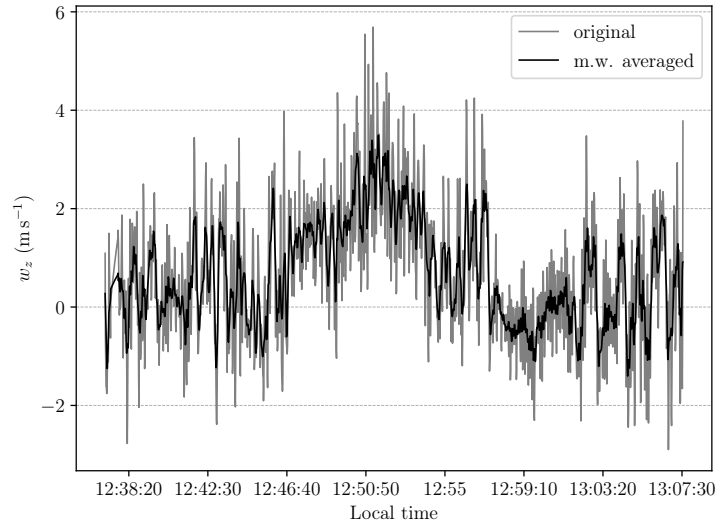
Figure 3.18: Vertical wind time series of flight #10 (21 September).

3.4 Summary

This chapter has presented the post-processing applied to the direct measurements recorded by the couple of instruments C-Pilot and C-Probe, and a first evaluation of their reliability has been conducted.

C-Pilot GPS receivers are considered sufficiently reliable, being in agreement with the data collected by pilot's personal flight instruments and with computed barometric altitude values. The measurement of altitude seems also quite sensitive to small oscillations.

Temperature and relative humidity measurements have been affected by a high adjustment time in the first minutes after take-off, related to a overheating effect caused by sunlight before the flight start. After that, their behaviour seems ordinary and the resolution is considered satisfactory. The adjustment time could be removed by lowering the time needed for pre take-off procedures such as the calibration of the instruments.

Pressure data collected by instruments b and c had to be discarded, due to unexpected, corrupted values. However, they have been replaced by pressure values computed via the hypsometric equation, that have resulted in good agreement with the valid data by instrument a.

The measurement of the wind has not produced reliable results, probably for calibration or installation problems, except for its vertical component. Only the latter is considered in Chapter 4.

Two flights (#4 and # 8), because of issues related to GPS altitude correction (Section 3.1.3) and pressure computation (Section 3.3.6) have been discarded for

further analysis, thus reducing the total number of flights from 19 to 17.

In Chapter 4, the quantities that have been derived as explained in Section 3.3 are involved in the analysis.

Chapter 4

Analysis of thermal structures

In this chapter, a study of the thermal structures detected by the measurements is conducted. Firstly, the sections of the flights that are thought to present ascending air, associated to the presence of upslope winds or thermals, are identified. A novel identification method, based on the paraglider key-property of being engine-free, is adopted. An overview of the 10 thermal sections that have been found is thus presented.

A total of three days of measurements resulted to include thermal sections: each of them is separately analysed, by means of vertical profiles of temperature, virtual potential temperature and mixing ratio, along with horizontal and vertical maps showing the spatial distribution of the thermodynamic variables and of vertical wind.

In the last part of the chapter a comparison between the five different flights containing thermal sections is carried out, to investigate the dependence of vertical wind on virtual potential temperature.

4.1   Identification of thermals

The method for identifying thermals adopted here differs from the literature presented in Section 1.2, since it is not based on threshold values of temperature or humidity as in the case of Lenschow and Stephens (1980) and Williams and Hacker (1992), but a different thermal indicator is used: the ascent or descent phases of the flight. Here, the identification takes advantage of the data acquisition methodology itself, i.e. paragliding. Indeed, as explained in Section 2.1, the paraglider gains or loses altitude according to the vertical motion of the air inside which it flies. In descending air or null vertical wind, the wing loses height with respect to ground, whereas an updraft makes it gain height. As already underlined, this holds with respect to ground: for the aerodynamic lift to be generated, the vertical velocity of the wind with respect to air (i.e. its sink rate – see Section 3.3.7) is always nega-

tive. Therefore, the paraglider itself, while flying and recording data, is probing the vertical movements of the atmosphere thanks just to its intrinsic nature.

Each flight point at time i is identified as an *updraft point*, that can be related to a thermal or an upslope current, if the vertical wind w_{z_i}, computed and averaged as explained in Section 3.3.7, satisfies $w_{z_i} > 0.4\,\mathrm{m\,s^{-1}}$. Instead, if $w_{z_i} < -0.4\,\mathrm{m\,s^{-1}}$, the point is considered a *downdraft point*. The choice of the threshold has been done considering the uncertainty ($\pm 0.4\,\mathrm{m\,s^{-1}}$) assigned to the sink rate, as explained in Section 3.3.7. Points with intermediate values of the vertical wind ($-0.4\,\mathrm{m\,s^{-1}} \leq w_{z_i} \leq 0.4\,\mathrm{m\,s^{-1}}$), whose classification is exposed to this uncertainty, are considered *calm air points*, in order to avoid misclassification of actual weak downdraft points as updraft points, and vice versa. Since the interest of the study is on updraft, more importance is given to an accurate identification of actual updraft points, even at the expense of a loss of weak updraft points, that are classified as calm air.

Also, the flight points are divided into two main categories according to GPS altitude measurements. A *glide section* is a group of consecutive time points during which altitude globally decreases with time (i.e. altitude at the final point is lower than altitude at the first point). It is called "glide" as it is related to the gliding mode of paragliding technique (see Section 2.1), in which the wing naturally loses altitude with respect to ground and is associated with null vertical wind or a downslope flow. Instead, a *thermal section* is defined as a group of consecutive time points during which altitude globally increases with time, and is related to the thermalling mode of paragliding. It is called "thermal" for this reason, but the phenomenon behind it is generically a mass of ascending air, that can specifically be a thermal or an upslope flow. Glide and thermal sections are expected to globally contain downdraft or calm air points, and updraft points, respectively.

In order to work, in the following analysis, with groups of updraft points large enough to ensure statical significance, thermal sections have to satisfy the condition of beginning with a local minimum and ending with a local maximum in the time series of GPS altitude, whose difference in height is greater or equal to 80 m. All the other sections with globally decreasing altitude are considered as glide sections. The choice of the threshold is related to the strength of the updrafts: it separates the few significant ascent phases of the flight from the many modest updraft sections. Weak-moderate convective conditions typical of the end of September developed on the days of measurement (see Section 2.6). Instead, if stronger convective conditions had been present, for example those that develop in the springtime or in different locations more internally in the Alps, a higher threshold or more than one threshold, to distinguish between moderate and strong updrafts, should have been used.

An example illustrating the identification of thermals is shown in Figure 4.1a.
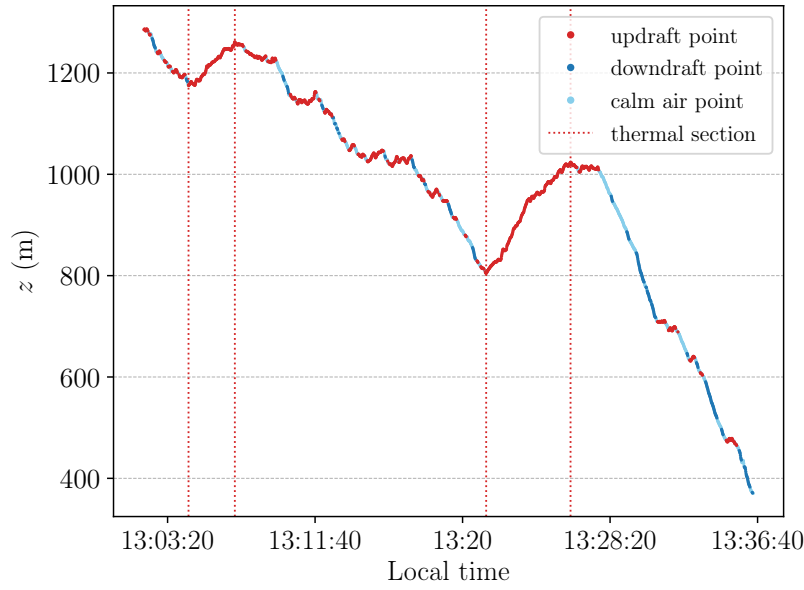
(a) GPS altitude time series, with flights points marked as updraft,
downdraft or calm air points. Vertical dotted red lines identify the extremes
of the thermal sections.
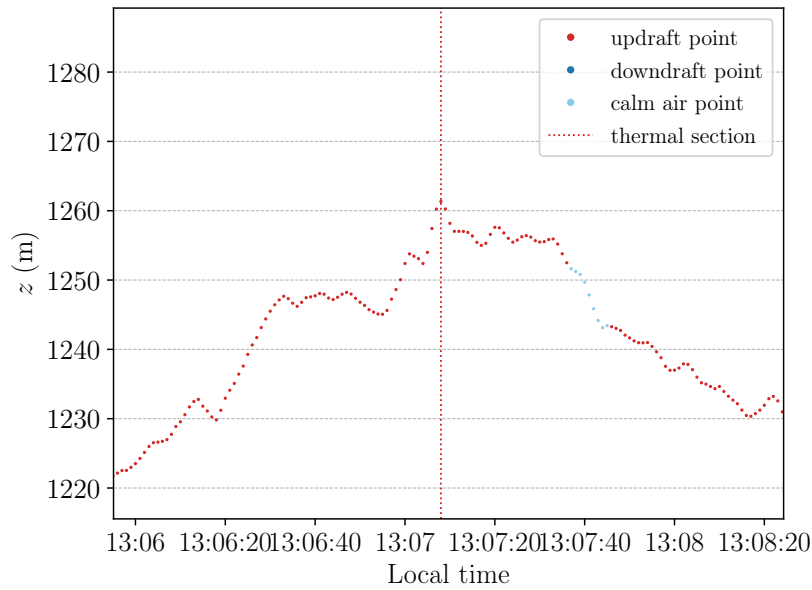
(b) Zoomed view centered on the maximum altitude of the first thermal
section.

Figure 4.1: Indentification of thermal sections for flight #5 (20 September).

Two main thermal sections are found and identified by vertical dotted red lines,
whereas minor altitude oscillations are not considered, according to the choice of
the 80 m threshold. As expected, the thermal sections contain updraft (red) points,
suggesting that the proposed thermal identification method is rather reliable.

Figure 4.1b shows an expanded view around the maximum altitude of the first

thermal for the same flight. While each segment showing altitude gain is composed of updraft points, some segments with decreasing altitude include updraft points as well. In the latter segments, the wing is losing altitude with respect to ground, but its negative vertical ground speed is smaller in absolute value than its sink rate. This is caused by the presence of ascending air (with positive vertical velocity, but smaller in absolute value than the sink rate) and for this reason the points are classified as updraft points.

Among the 17 flights, a total of 10 main thermal sections have been identified. They belong to five flights, distributed between three different days: 20, 21 and 30 September. This is not surprising, as their synoptic conditions and soundings profiles, as observed in Section 2.6, are likely associated to the development of convection.

Table 4.1 presents an overview of the 10 thermal sections identified as explained above. The numbering of the flights is the same of Table 2.2. Δt is the duration of the thermal section, while Δz is the GPS altitude gain. Starting and ending flight times and altitudes are also shown in brackets. $\overline{z_g}$ is the mean height over ground during the thermal section, derived as the difference between the GPS altitude and the corresponding DTM elevation values.

In the following sections, the three days of measurement that include thermal sections are examined, with vertical profiles and horizontal and vertical maps showing the spatial distribution of the interesting variables.

4.2   21 September

The first thermal sections analysed are those detected on 21 September, for simultaneous flights #9 and #10, shown respectively in Figure 4.2a (thermal section #6) and Figure 4.2b (thermal section #7). The vertical green line is related to the choice of the flight section to be shown in horizontal and vertical maps (see Section 4.2.4). The black line is the time series of the corresponding height over ground.

As Table 4.1 suggests, thermal section #9 is found approximately 6 min earlier, at a starting altitude about 245 m higher and higher along the slope (see Figure 2.16) than thermal section #10. Thermal section #10 is more than 2 min longer and has an altitude gain about 100 m greater than thermal section #9.

thermal section	flight	date	Δt	Δz (m)	$\bar{z}_g$ (m)
1	5	20/09/2019	2 min 37 s (13:04:31 − 13:07:08)	86.0 (1175.4 − 1261.3)	102.0
2	5	20/09/2019	4 min 46 s (13:21:20 − 13:26:06)	218.9 (804.9 − 1023.8)	295.2
3	7	20/09/2019	3 min 14 s (15:50:07 − 15:53:21)	95.9 (1250.4 − 1346.3)	76.8
4	7	20/09/2019	5 min 36 s (16:11:04 − 16:16:40)	373.5 (1161.5 − 1535.0)	347.2
5	7	20/09/2019	9 min 26 s (16:29:11 − 16:38:37)	487.9 (1007.0 − 1494.9)	247.0
6	9	21/09/2019	4 min 49 s (12:40:39 − 12:45:28)	207.0 (1086.7 − 1293.7)	146.8
7	10	21/09/2019	7 min 11 s (12:46:45 − 12:53:56)	301.2 (842.9 − 1144.1)	135.2
8	19	30/09/2019	2 min 22 s (15:31:18 − 15:33:40)	146.2 (1105.0 − 1251.2)	122.0
9	19	30/09/2019	3 min 28 s (15:44:45 − 15:48:13)	117.5 (667.7 − 785.1)	377.2
10	19	30/09/2019	2 min 20 s (15:49:40 − 15:52:00)	108.9 (750.3 − 859.2)	473.0

Table 4.1: Overview of the 10 identified thermal sections. The numbering of the flights follows Table 2.2.
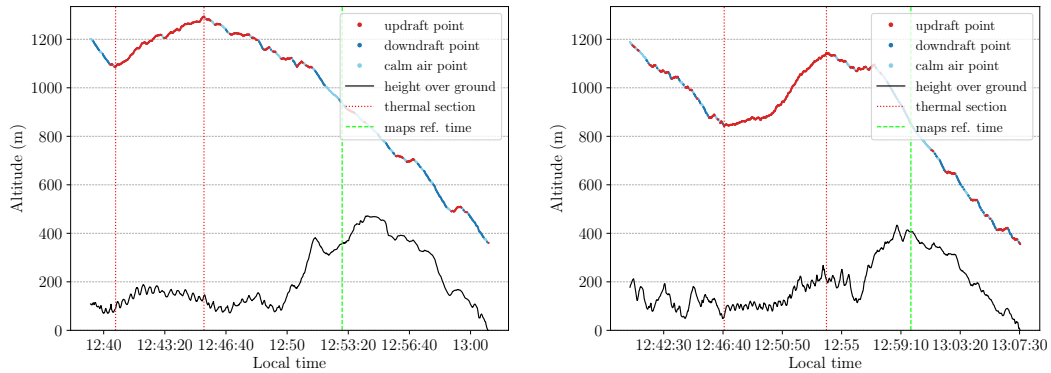
(a) GPS altitude time series of flight #9, with the identification of updraft, downdraft and calm air points and the thermal section #6.

(b) GPS altitude time series of flight #10, with the identification of updraft, downdraft points and calm air points and the thermal section #7.

Figure 4.2: Identification of thermal sections of flights #9 and #10 on 21 September.

4.2.1   Vertical profiles

The vertical profile of temperature for flight #9 is shown in Figure 4.3a. Flight data are divided into three sections: glide section 1 (blue) is the first part of the flight until the beginning of the thermal section #6 (red), while glide section 2 (green) is the following part of the flight after the end of the thermal section. The glide sections correspond to the altitude time series in Figure 4.2a respectively before and

after the vertical red lines. Data from the soundings in Rivolto (LIPI, black) and in Milano (LIML, grey) are also shown, as well as data collected by the surface weather stations. ARPAV Monte Avena and Feltre stations are located respectively above all the take-off sites and under the landing areas Boscherai and Arten. Thus, take-off sites and landing areas have the altitude values closest to ARPAV stations altitude among all the flight data points. The figure thus presents the measurements taken by the stations at the closer time to take-off and landing times, respectively. Similarly, Festisei measurement has been taken at the time closest to the passage of the pilot at Festisei station altitude. In this case, a good agreement with in-flight measurements, even though at the same altitude, cannot be expected, as the meteorological variables recorded by Festisei station are probably influenced by the presence of the surface.

In the same way, Figure 4.4a shows the temperature vertical profile of flight #10.

The profiles for both the flights seem in agreement with soundings and surface weather stations data. While vertical soundings depict the state of the atmosphere at a regional scale (see Figure 2.6 for the position of soundings stations), flight data present the local nature of the boundary layer above complex terrain, with its spatial variability not only along the vertical direction, but also in the horizontal ones. The difference of T between the three flight sections is clearly visible, especially for flight #10, reflecting the different nature of the corresponding air masses. During flight #10, the pilot first glided following the blue line, then found a warmer mass of ascending air (red) and finally glided again in intermediate temperature air. In case of flight #9, the glide 1 and thermal sections profiles approximately coincide.

Even though the different sections of the flights have been temporally distinguished, the profile can be assumed stationary or quasi-steady, as the total flight duration, about 24 min (flight #9) and 30 min (flight #10), is smaller than the characteristic time scale of the boundary layer evolution, i.e. about 1 h (Stull, 1988).

Figure 4.3b presents the same vertical profile of Figure 4.3a, but flights points are divided into updraft (red), downdraft (blue) and calm air (light blue) points. The solid line displays a moving window average performed on the data points, as done in Laiti et al. (2013), with the same colour division of the three sections of Figure 4.3a. The chosen window consists of 60 data points, equal to 1 min, centered on the considered point. Figure 4.3d shows the altitude interval interested by the window as it moves along the flight time line. The window width has been chosen, similarly to Laiti et al. (2013), to obtain a profile as smooth as possibile and normally distributed residuals (see below). The same procedure is followed for flight #10, in Figure 4.4b and Figure 4.4d.
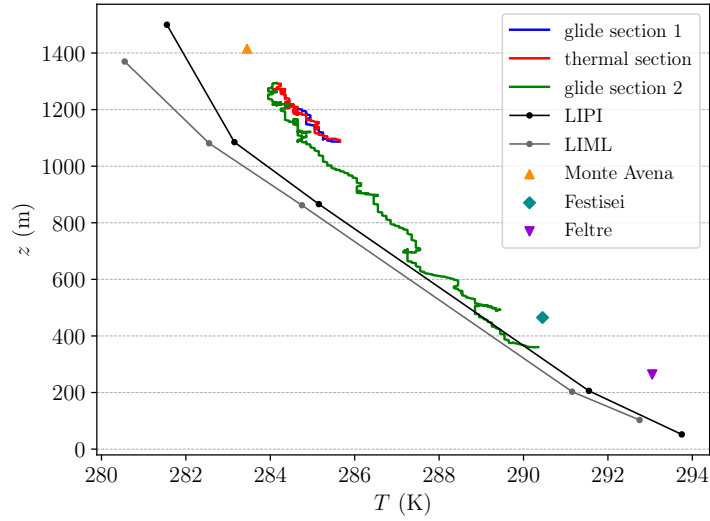
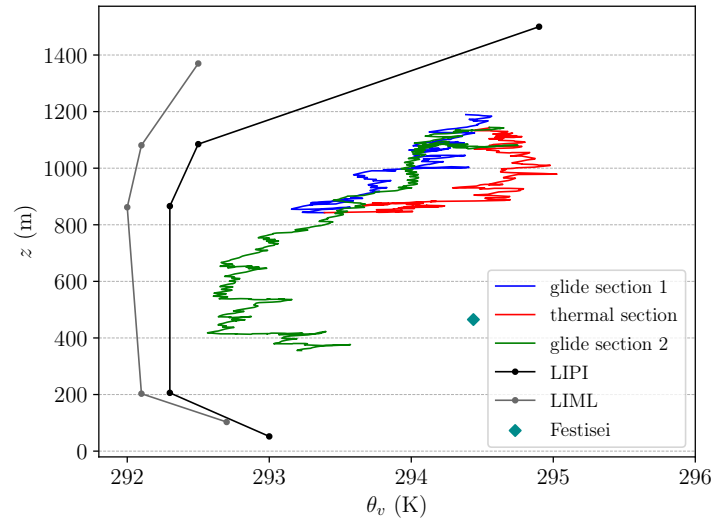(a) Temperature vertical profile with soundings and surface weather stations data.
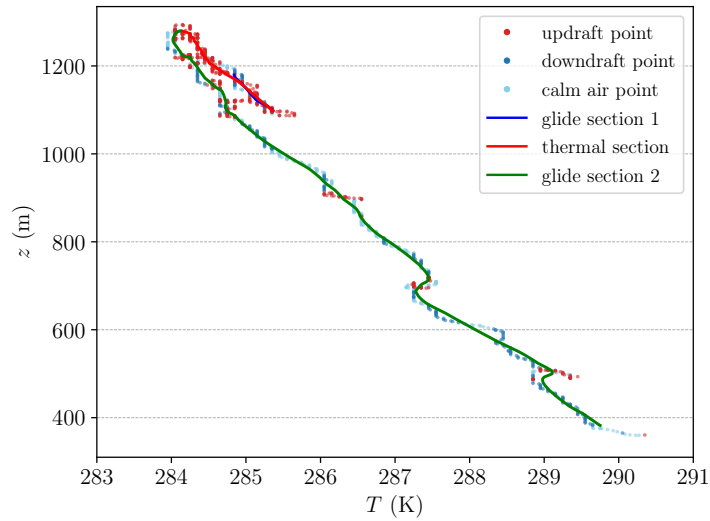
(b) Temperature vertical profile with a moving window (60 s) average.
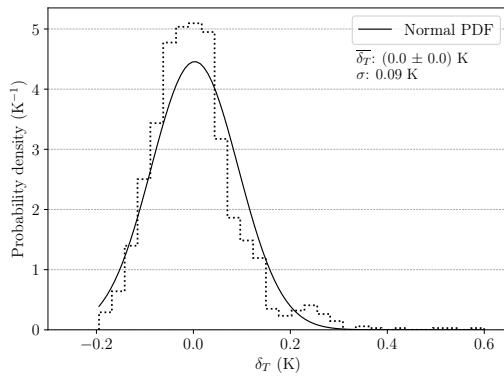
(c) Distribution of the residuals of temperature from the moving window average.
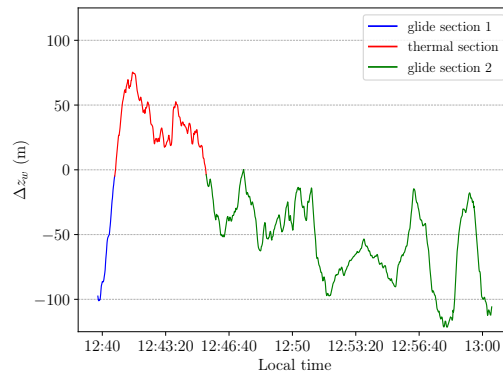
(d) Time series of the altitude intervals covered by the moving window average.

Figure 4.3: Temperature vertical profile of flight #9 (21 September).
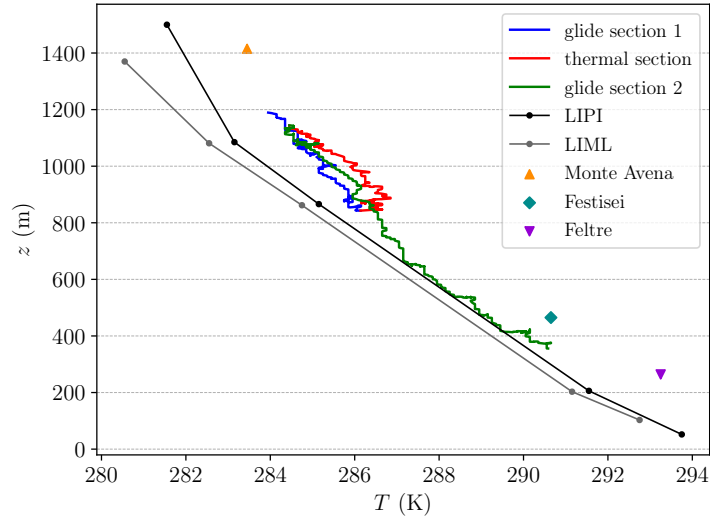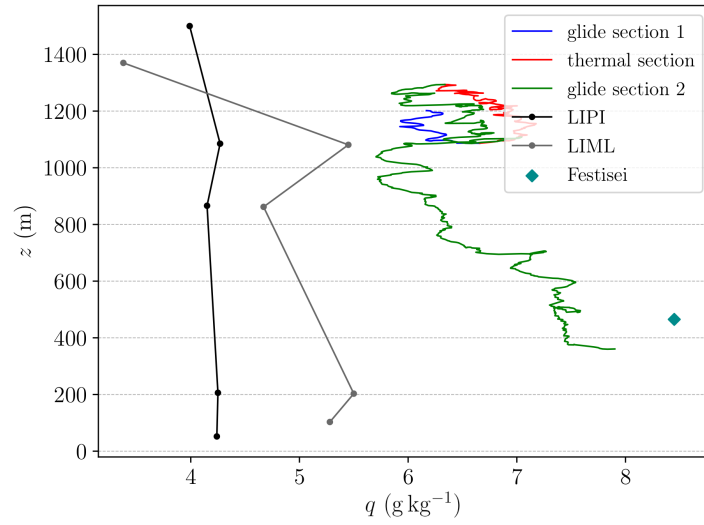
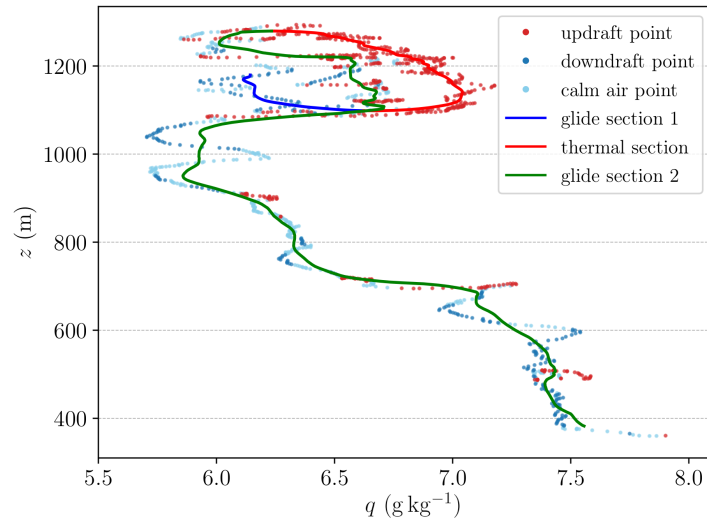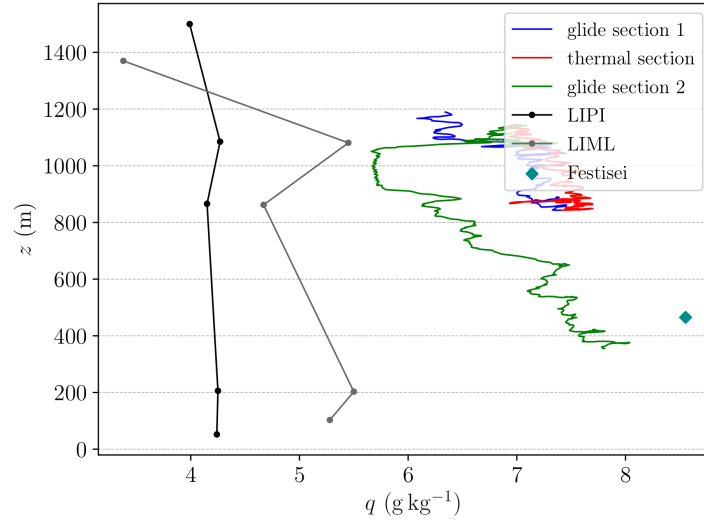(a) Temperature vertical profile with soundings and surface weather stations data.
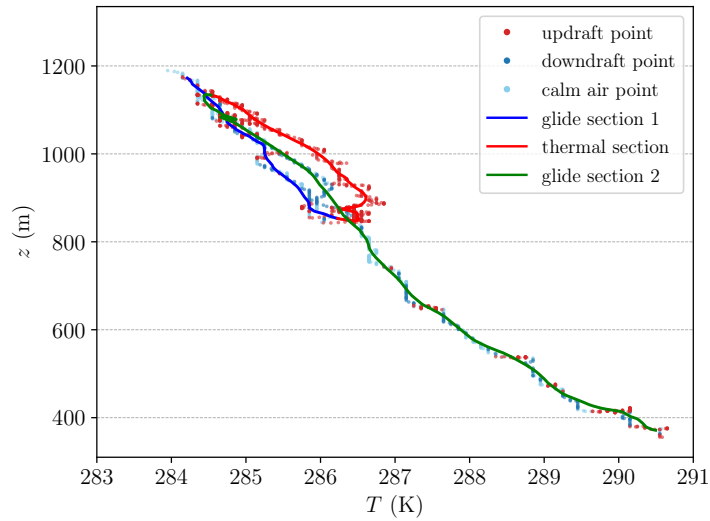
(b) Temperature vertical profile with a moving window (60 s) average.

(c) Distribution of the residuals of temperature from the moving window average.
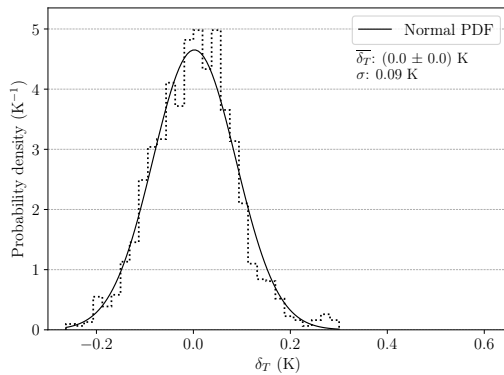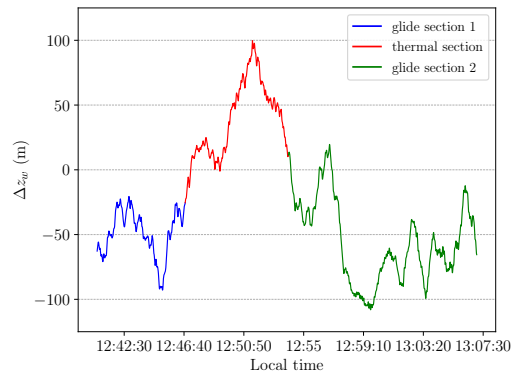
(d) Time series of the altitude intervals covered by the moving window average.

Figure 4.4: Temperature vertical profile of flight #10 (21 September).

97

The average represents the dominant vertical structure of the boundary layer above the slope and the valley, filtering out the variability of the original data points that deviate from it. This is evident in glide sections 2 of both flights, where some altitude levels present original T values that are not constant (horizontally distributed red updraft points). As an example, Figure 4.5 shows the group of the data points between 13:04:03 ($z = 543.2$ m) and 13:04:34 ($z = 531.4$ m), both in the temperature vertical profile (Figure 4.5a) and in the GPS altitude time series (Figure 4.5b). The pilot experienced an up-down oscillating motion around a mean altitude ($z \sim 537$ m) in a limited time interval (31 s). The same data points are shown on the 2-D horizontal plane in Figure 4.5c, coloured according to original temperature values and with contour lines of the Digital Terrain Model each 2 m. The section is near the landing area and the trajectory was flown from the upper right corner towards the lower left corner of the plot.
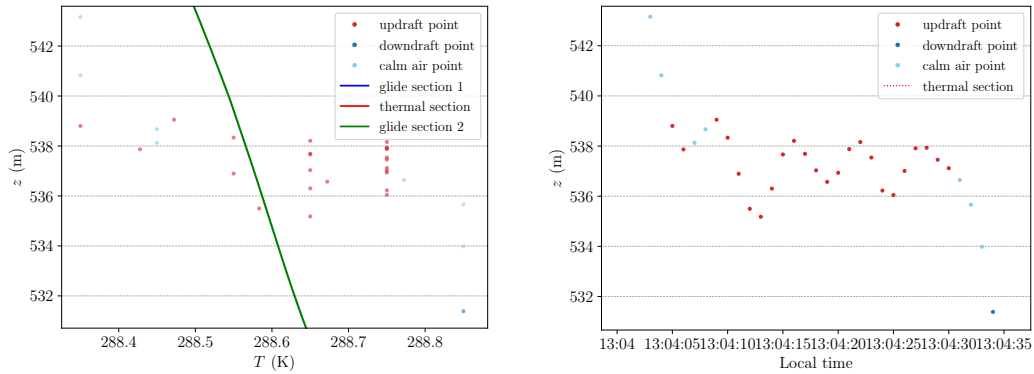
(a) Zoomed view of the temperature vertical profile.

(b) Zoomed view of the GPS altitude time series.
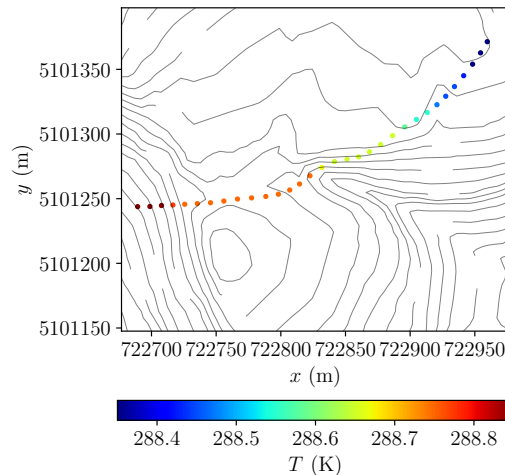
(c) Trajectory of the corresponding flight section.

Figure 4.5: Temperature small-scale anomalies from the moving window average (green) for a section of flight #10 (21 September).

The variability displayed by original data points may account for the local spatial patterns of thermodynamic variables, that could derive from complex orography and strong surface inhomogeneities (Laiti, 2013). Considerations based on the spatial coverage of the trajectories are given in Section 4.2.4.

If the window width is increased to time intervals longer than the duration of the thermal sections (for example, 10 min for thermal section #7), the vertical profiles become smoother, tending to a straight line, and even the thermal sections are no longer visible.

The averaged profiles in Figure 4.3b and Figure 4.4b appear fairly linear with altitude, in particular for flight #10. The mean total temperature gradient for the three sections (respectively glide 1, thermal, glide 2), computed as the ratio of the difference between maximum and minimum T of the section and the corresponding difference in z, results $6.4\,\mathrm{K\,km^{-1}}$, $6.8\,\mathrm{K\,km^{-1}}$ and $6.5\,\mathrm{K\,km^{-1}}$ for flight #9, and $6.3\,\mathrm{K\,km^{-1}}$, $8.8\,\mathrm{K\,km^{-1}}$ and $8.0\,\mathrm{K\,km^{-1}}$ for flight #10.

In Figure 4.3c and Figure 4.4c the distribution of temperature residuals (δ_T) with respect to the moving window average is presented. δ_T is the difference between the original T and the averaged temperature at each time point. A density histogram (dotted line) is compared to a normal probability density function (solid line) – the height of each histogram bin being the relative frequency of the residuals in that bin, divided by the bin width itself. The normal distribution is:

$$f(\delta_T, \overline{\delta_T}, \sigma) = \frac{1}{\sqrt{2\pi}\sigma} \exp\left(-\frac{1}{2}\frac{(\delta_T - \overline{\delta_T})^2}{\sigma^2}\right), \tag{4.1}$$

where the values of the mean $\overline{\delta_T}$ and the standard deviation σ are derived from the residuals and are included in the figure. It can be seen that the distribution of the residuals is well approximated by the gaussian PDF, centred on zero. This would allow to use the averaged profiles and their residuals respectively as drift and residual terms in a residual kriging interpolation algorithm, in order to obtain a 3-D field of the interesting thermodynamic variables from their measured values (Laiti, 2013). This has not been done in the present work, but it could represent an interesting development.
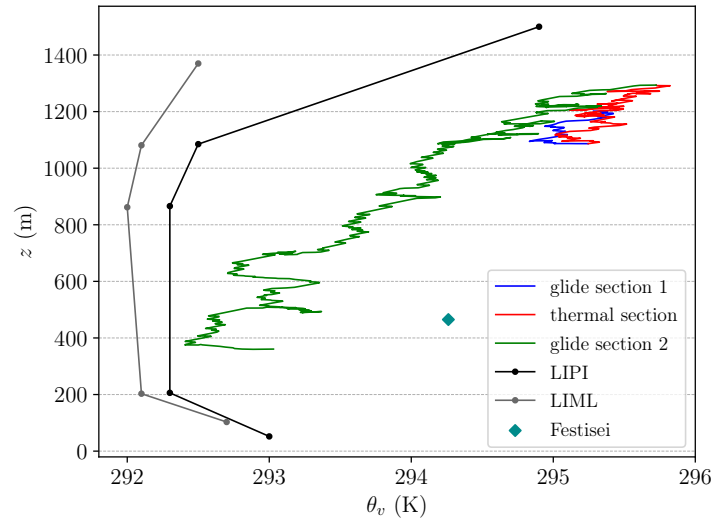
(a) Virtual potential temperature vertical profile with soundings and surface weather stations data.
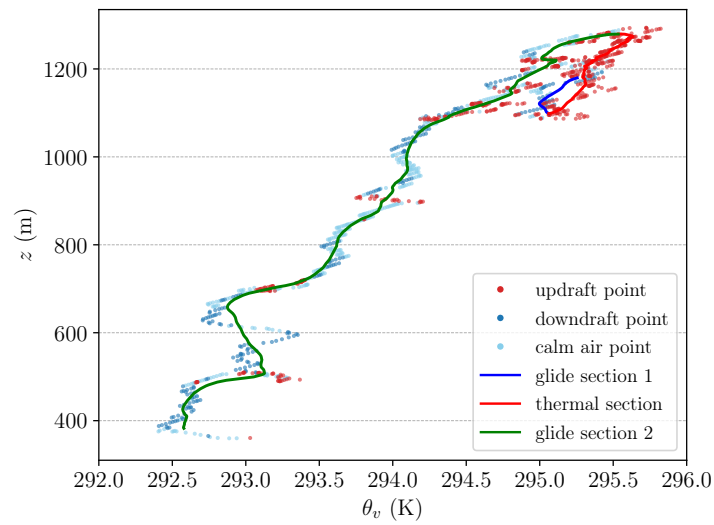
(b) Virtual potential temperature vertical profile with a moving window (60 s) average.

Figure 4.6: Virtual potential temperature vertical profile of flight #9 (21 September).

(a) Virtual potential temperature vertical profile with soundings and surface weather stations data.
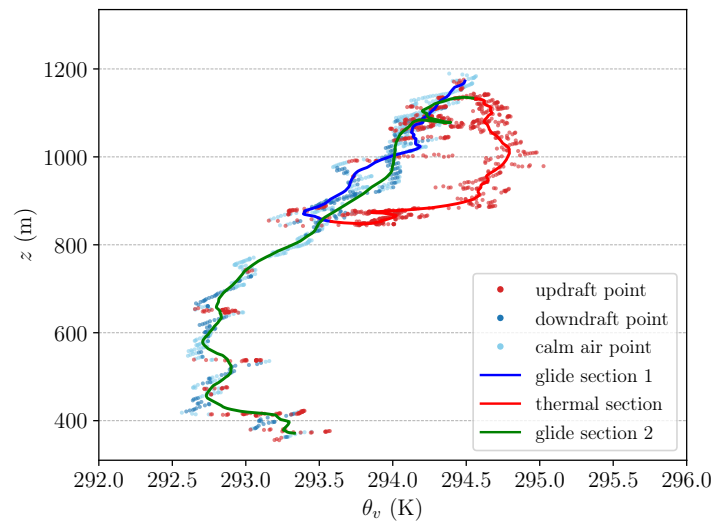
(b) Virtual potential temperature vertical profile with a moving window (60 s) average.

Figure 4.7: Virtual potential temperature vertical profile of flight #10 (21 September).

(a) Mixing ratio vertical profile with soundings and surface weather stations data.

(b) Mixing ratio vertical profile with a moving window (60 s) average.

Figure 4.8: Water vapour mixing ratio vertical profile of flight #9 (21 September).

(a) Mixing ratio vertical profile with soundings and surface weather stations data.
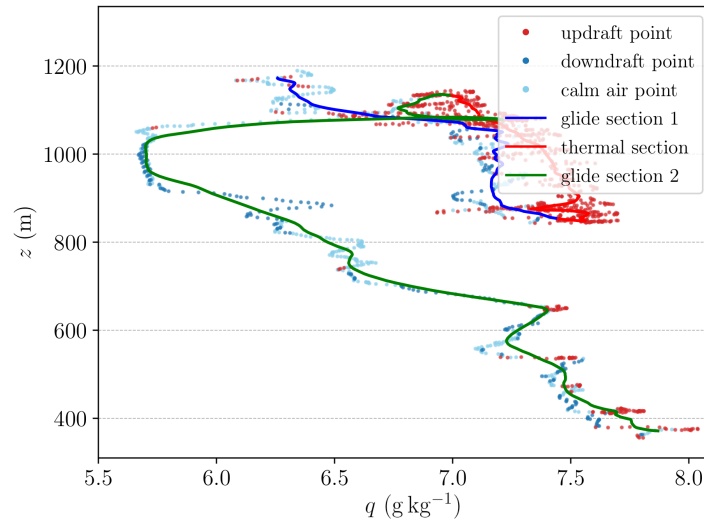
(b) Mixing ratio vertical profile with a moving window (60 s) average.

Figure 4.9: Water vapour mixing ratio vertical profile of flight #10 (21 September).

In Figure 4.6, Figure 4.8, Figure 4.7 and Figure 4.9, vertical profiles of virtual potential temperature and water vapour mixing ratio are presented respectively for flights #9 and #10, in a way similar to temperature vertical profiles. The interpretation is made a little more complicated by the fact that they are derived variables (see Section 3.3.3 and Section 3.3.4), not directly measured. The atmospheric layer between 400 m and 700 m seems to be rather mixed, as θ_v appears on average constant with height, around 293 K, for both flights. Above 700 m, the boundary layer seems stable, as the gradient of θ_v with z, related to the glide sections, is about $4 \, \mathrm{K \, km^{-1}}$ (flight #9) and $3 \, \mathrm{K \, km^{-1}}$ (flight #10). Soundings data suggest a similar behaviour, even if to a lesser extent than the temperature profiles. Here only Fes-

tisei station data are presented, as the two ARPAV stations do not record pressure data, needed for the computation of θ_v and q. The trend of the mixing ratio q is less clear. The agreement of Festisei station data is limited since, as observed before, the measurements collected there are affected by the heating of the surface, differently from the data recorded in flight.

Also θ_v and q residuals (not shown) follow a gaussian distribution, and the altitude interval covered by the moving window is not shown, as it is the same as before.

4.2.2 T, θ_v and q excess

(a) Temperature excess.

(b) Virtual potential temperature excess.

(c) Mixing ratio excess.
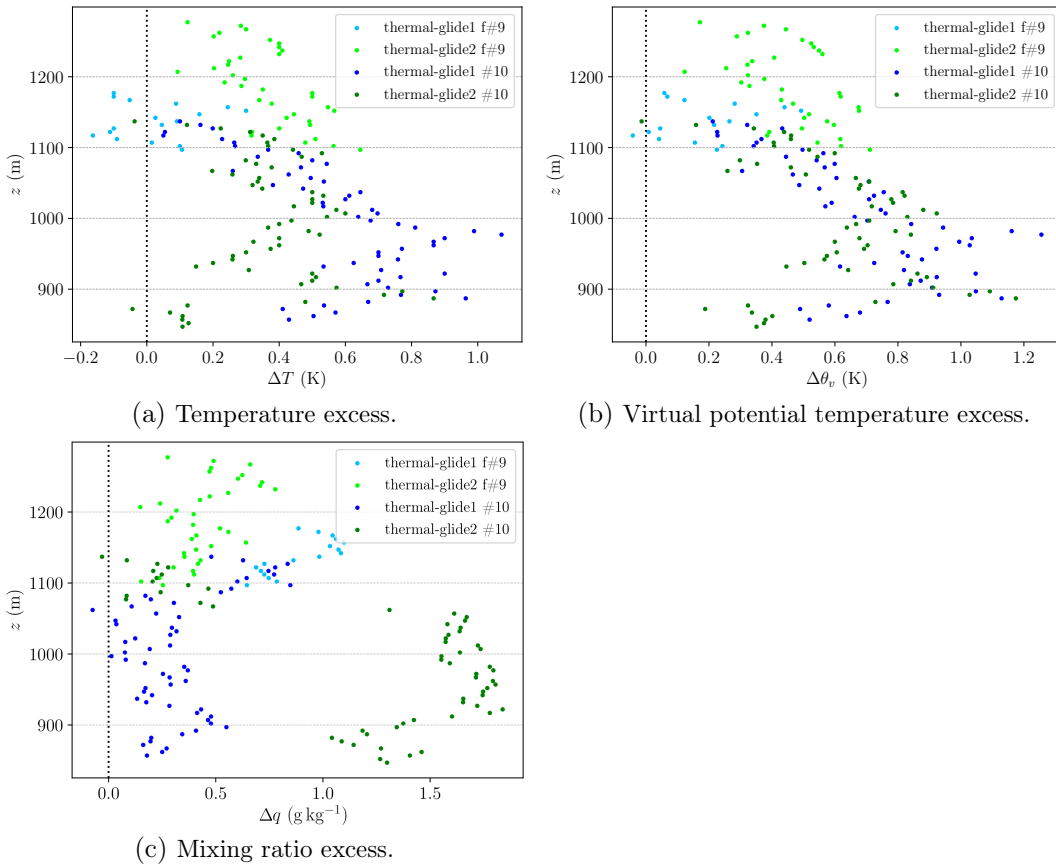
Figure 4.10: Temperature, virtual potential temperature and mixing ratio excess between thermal and glide sections for flights #9 and #10.

As seen in Section 1.2, thermals are expected to display a temperature and humidity excess with respect to environmental air (Lenschow and Stephens, 1980). The differences of T, θ_v and q between the thermal and the glides sections moving window averaged profiles are thus shown in Figure 4.10. It displays the excess of each thermodynamic variable of the thermal section with respect to glide sections 1 (blue)

and 2 (green) for flight #10, and the same for flight #9 with lighter colours. The temperature excess ΔT is computed as the mean difference inside 5 m-altitude bins between the temperature of the thermal section and that of the glide section (1 or 2) inside the same bin, in an altitude interval shared by all the three sections. The considered temperature is the moving window averaged T as before. The same has been done for $\Delta \theta_v$ and Δq.

Temperature and virtual potential temperature excesses for flight #10 (dark colours) show that the thermal section is warmer than the two glides at all heights, excluding a few negative values. This agrees with what observed by Lenschow and Stephens (1980), Arnold (1976), Stull (1988) (Section 1.2).

ΔT between thermal section and glide 1, greater than for glide 2, globally decreases with altitude, from $\Delta T \sim 1.0$ K at $z \sim 890$ m to $\Delta T \sim 0.1$ K at $z \sim 1140$ m. The same behaviour is shown by $\Delta \theta_v$. This suggests that the thermal "strength", that increases with increasing temperature excess with respect to surrounding air, decreases with altitude.

Δq is also positive at all heights, and, for the difference thermal-glide1 of flight #10, sligthly increases with altitude, from $\Delta q \sim 0.2$ g kg^{-1} at $z \sim 850$ m up to $\Delta q \sim 1.0$ g kg^{-1} at $z \sim 1140$ m.

The trend of the excesses for flight #9 is less clear, but it seems, for T and θ_v, to very well agree with that of flight #10, extending the trend at higher altitudes, especially for the thermal-glide1 difference. This could suggest that the ascending air mass encountered at lower altitudes by the pilot of flight #10 and at higher altitudes by that of flight #9 is probably part of the same thermal structure. The analysis of horizontal and vertical maps (Section 4.2.4) gives further evidence.

4.2.3   Skew-T Log-P diagrams

Temperature vertical profiles of flights #9 and #10 are also depicted in the Skew-T Log-P diagrams of Figure 4.11. Flight data averaged with the 60 points (1 min) moving average, soundings and surface stations data are represented as before. ARPAV stations (Monte Avena and Feltre) are missing since pressure measurements are not collected there, thus preventing the computation of θ_v and q. Dry adiabats, moist adiabats and mixing ratio lines are displayed as red, blue and green dashed lines respectively.

The diagrams confirm what already observed in temperature vertical profiles: the different sections of the flight – glides and thermals – can be clearly distinguished and the agreement with soundings is good. Again, the difference between Festisei and flight data can be explained by the influence of the surface on the measurements collected there. Also, different T values between Festisei and the two soundings can

be related to differences in land covers and surface local features between the foot of Monte Avena and the airports in Rivolto and Milano.

Red thermal sections, especially for flight #10, look rather parallel to dry adiabats, suggesting that the acting phenomenon, that is probably a thermal structure, can be considered as a dry adiabatic process – dry as condensation never occurred at altitudes covered during both flights (modest cumulus clouds developed only above the top of the mountain level, about 1450 m).
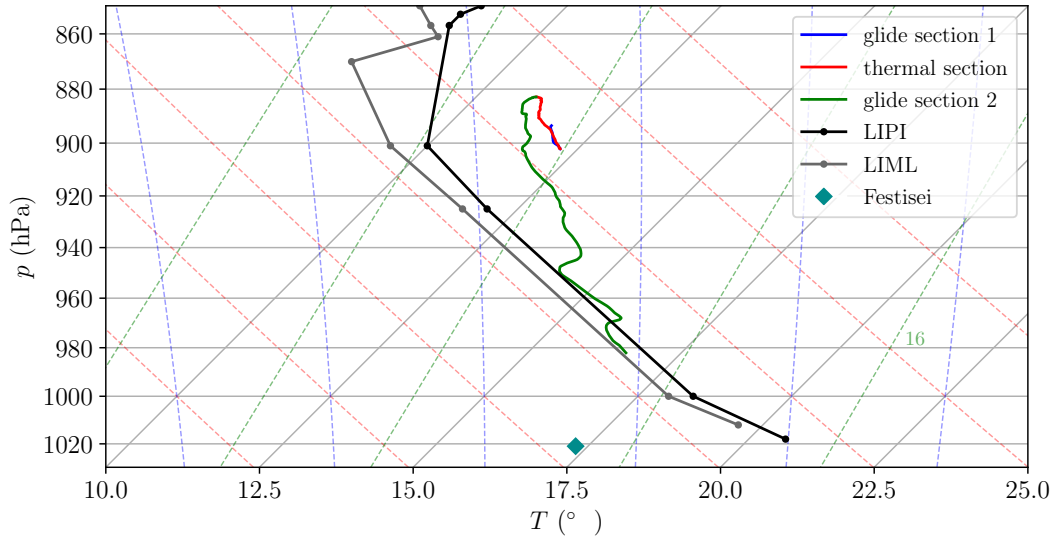
(a) Skew-T log-P diagram for flight #9.
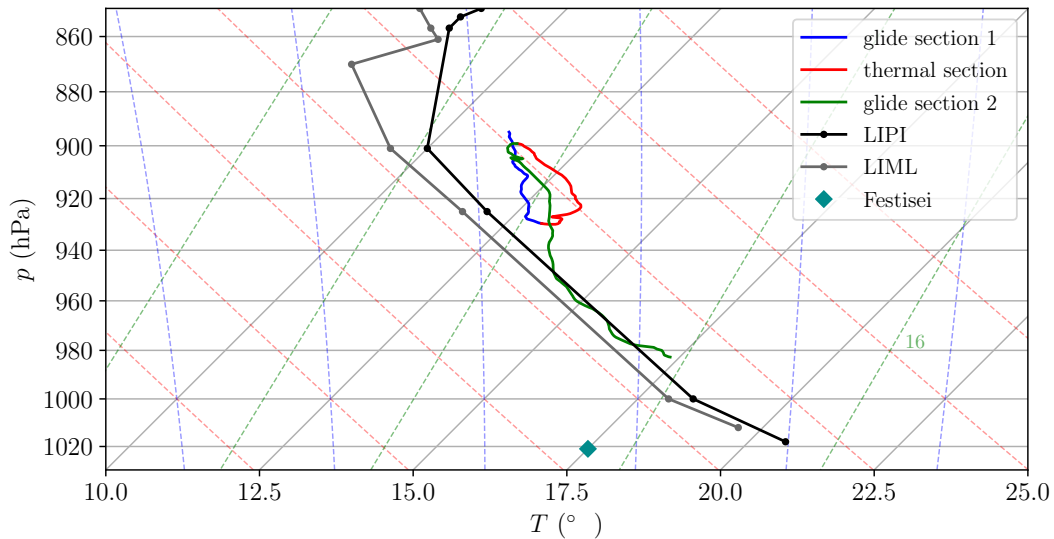
(b) Skew-T log-P diagram for flight #10.

Figure 4.11: Skew-T log-P diagrams for flights #9 and #10 (21 September), with soundings data and Festisei station data.

4.2.4   Maps

In the following figures, horizontal and vertical maps of the flight area of 21 September are presented (Figure 4.12, Figure 4.13, Figure 4.14, Figure 4.15). Each map contains both the trajectories followed by the two pilots, coloured according to the values of T, θ_v, q and w_z, in order to show the spatial distribution of the considered variables. T, θ_v and q values are the original data measurements (not averaged), while w_z is the 10 points moving window averaged as explained in Section 3.3.7.

The trajectory points are projected respectively onto the 2-D x-y, x-z and y-z planes of the standard meteorological coordinate system (see Section 3.3.1). The flight sections between the first data point (that coincides with the beginning of the valid temperature data – see Section 3.2.1) and the vertical green line are represented respectively in Figure 4.2a for flight #9 and in Figure 4.2b for flight #10. The choice of the green line has been made to obtain horizontal maps showing a portion of the slope between the position of the first data points and approximately the boundary between slope and valley (see Figure 2.16, where the complete trajectories are shown). The flight sections thermal, glide 1 and glide 2 are indicated in the plot respectively by "th", "g1" and "g2", followed by "f9" for flight #9 or "f10" for flight #10.

In the vertical sections, some portions of height are not covered by either trajectory – see for example the lower right corner of Figure 4.12c, where g2 f9 stops at about 950 m. The reason is that the second part of the flight, filling the lower altitudes, moves rapidly away from the slope, reaching low heights only near the landing site (Figure 2.16). Therefore it is not considered, as the interest of the work is focused on the slope.

For horizontal maps, the DTM elevation contour lines are displayed each 20 m. Notice that in vertical maps, the scales respectively of the x- and y- axes are different.

The horizontal and vertical maps give an idea of how the variables values are distributed along the flight paths. In the horizontal ones, trajectories are travelled from left (higher elevation values) to right (lower elevation values), with the exception of spiral trajectories, corresponding to thermal section (th 9 and th 10), during which the pilots climbed the slope and gained height. Black arrows indicate the direction along which the trajectories are followed.

The distribution of T in Figure 4.12 follows the temperature vertical gradient already seen in the vertical profiles. As already observed, the thermal sections appear warmer than glide sections at the same altitude, as visibile in the vertical maps (Figure 4.12b and Figure 4.12c). The same is valid also for virtual potential temperature (Figure 4.13).
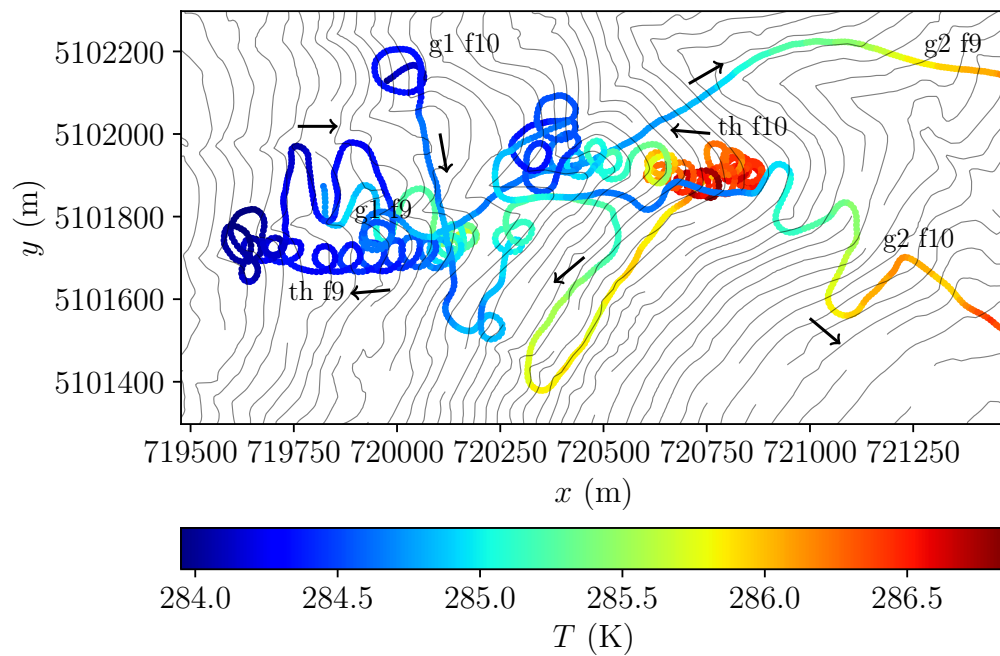
(a) Horizontal map.
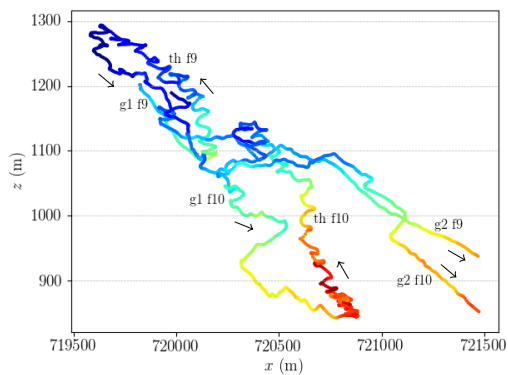
(b) Vertical map (x-z plane).
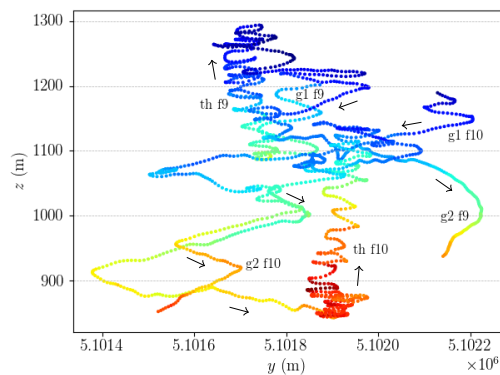
(c) Vertical map (y-z plane).

Figure 4.12: Temperature maps of flight #9 and #10 (21 September).
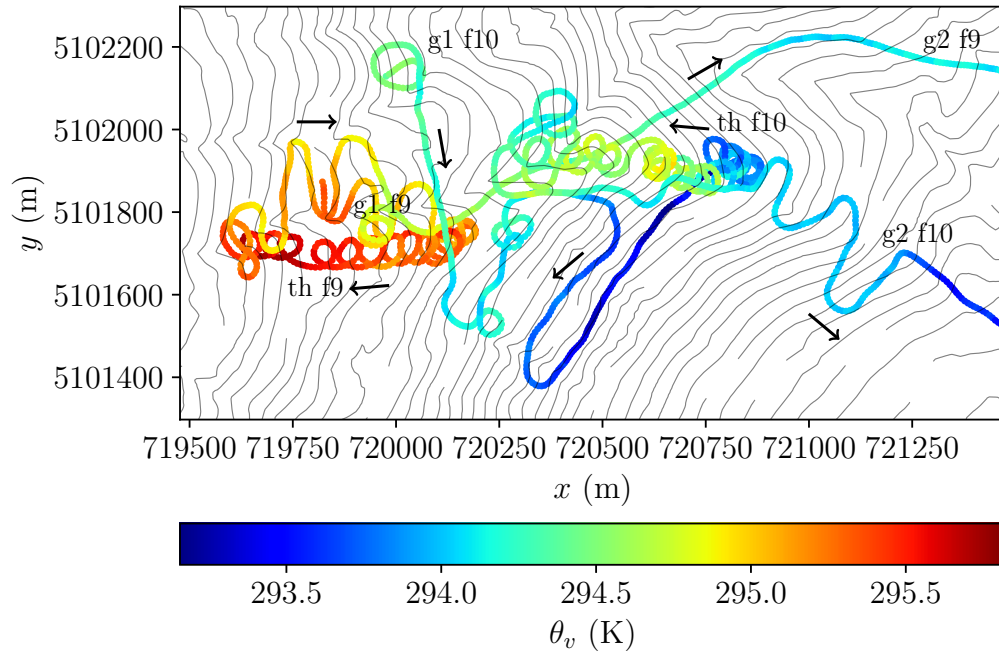
(a) Horizontal map.
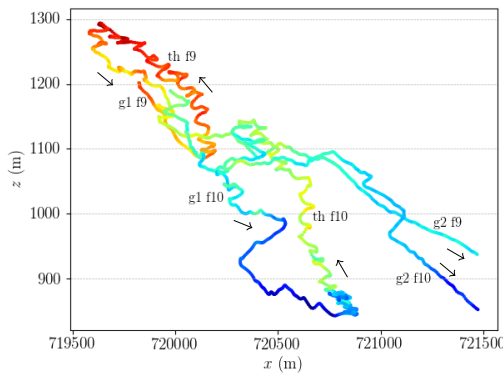
(b) Vertical map (x-z plane).
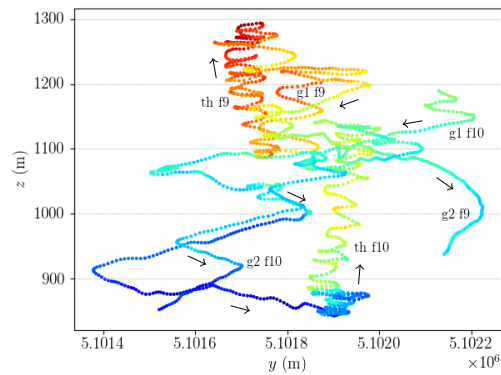
(c) Vertical map (y-z plane).

Figure 4.13: Virtual potential temperature maps of flight #9 and #10 (21 September).

q horizontal map (Figure 4.14a) shows that air outside the region occupied by thermals is drier (dark blue), even if at the same altitude, as clearly visible in the vertical maps (Figure 4.14b and Figure 4.14c), where the two glide sections of flight #10 (g1 f10, yellow-red and g2 f10, dark blue) have a q difference of about $1.2\,\mathrm{g\,kg^{-1}}$: the ascending air mass encountered by the pilot of flight #10 had probably moved away by the time he reached the dark blue region of the horizontal map, suggesting the upslope movement of the thermal structure.
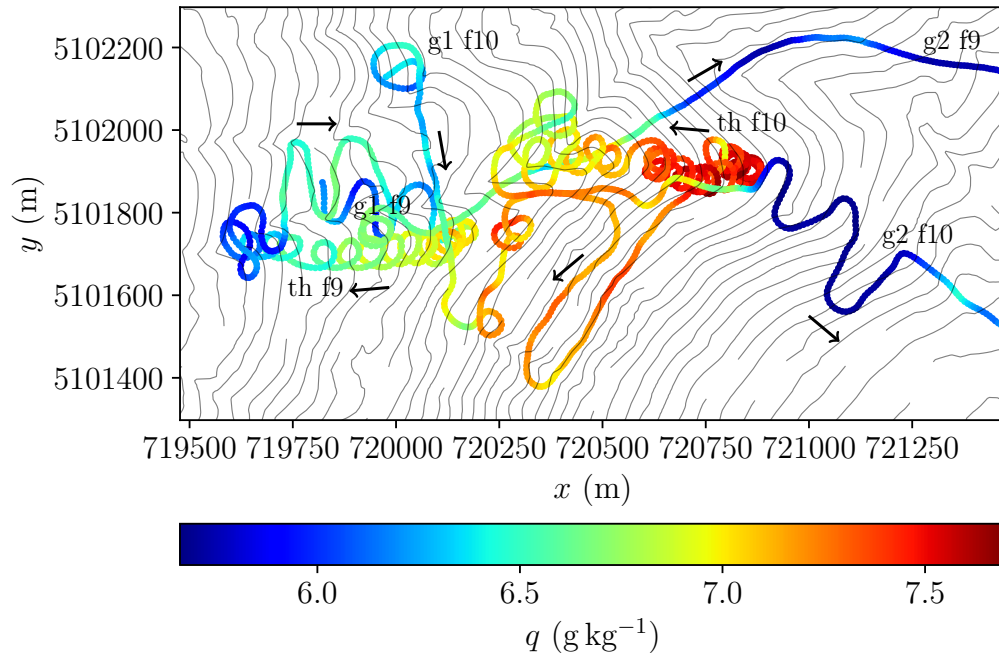
(a) Horizontal map.
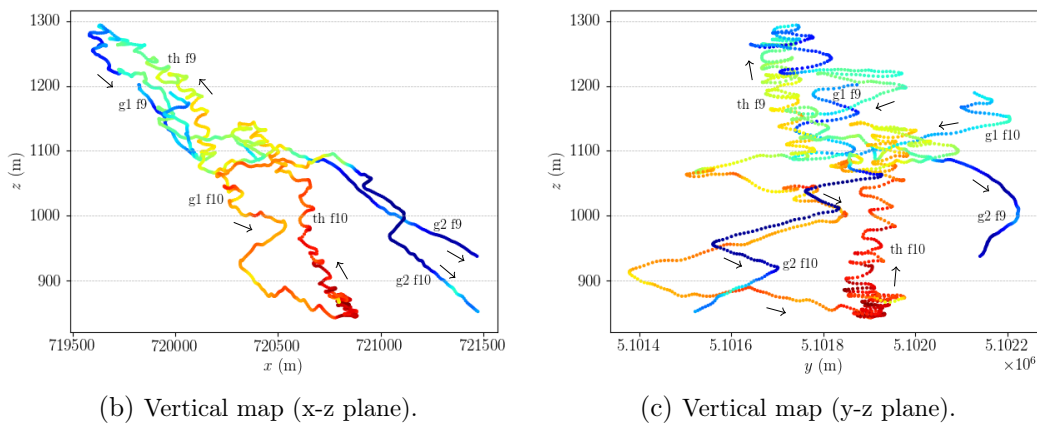
(b) Vertical map (x-z plane).

(c) Vertical map (y-z plane).

Figure 4.14: Mixing ratio maps of flight #9 and #10 (21 September).

The distribution of vertical wind (Figure 4.15) seems to confirm the accurate identification of the thermal sections: th f9 and th f10 clearly show higher w_z intensities than the surrounding points, both in the horizontal and in the vertical directions. They have comparable mean w_z intensities ($1.9\,\mathrm{m\,s^{-1}}$), with higher peaks reached by th f10 ($3.5\,\mathrm{m\,s^{-1}}$). After leaving the ascending air mass of th f9, the pilot encountered again ascending air (short red segment), in the region where about 6 min later (see Table 4.1) the pilot of flight #10 was spiralling up. The same is valid vice versa: the pilot of flight #10, during its first glide section, crossed without spiralling the th f9 region.

110

(a) Horizontal map.

(b) Vertical map (x-z plane).

(c) Vertical map (y-z plane).
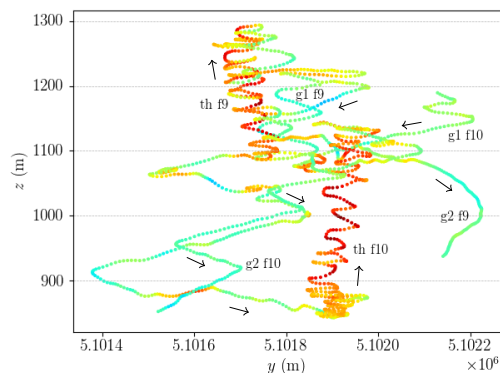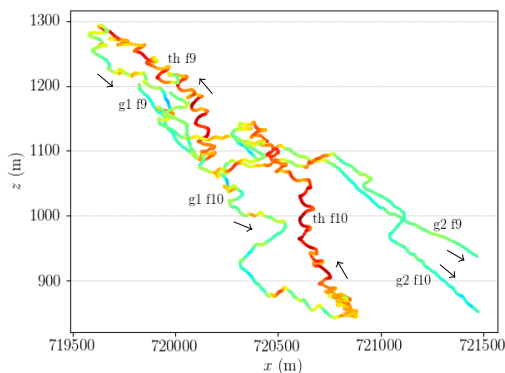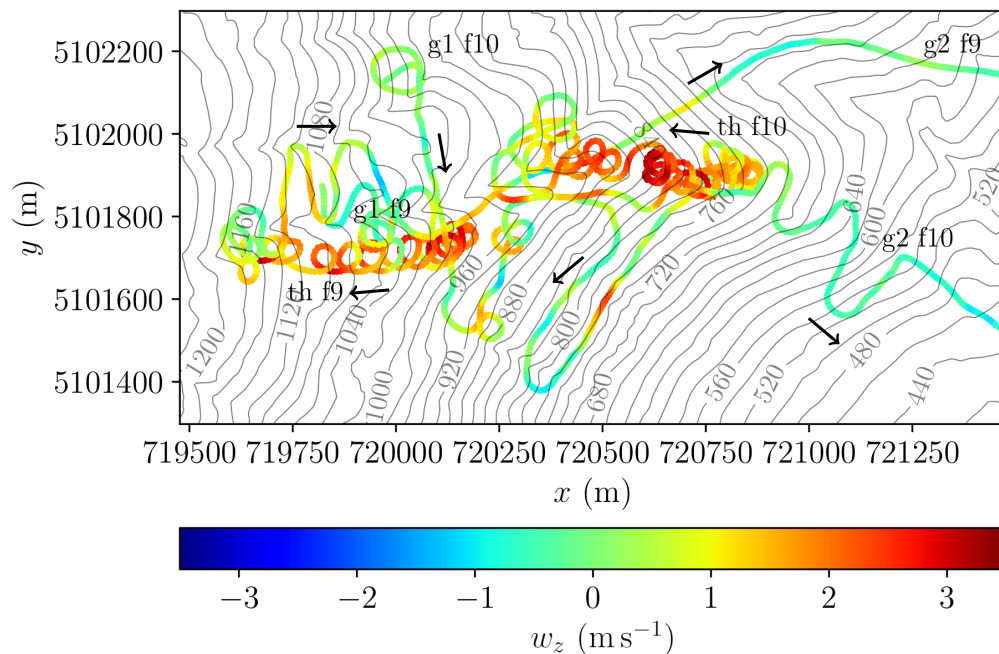
Figure 4.15: Vertical wind maps of flight #9 and #10 (21 September).

The proximity in time and space, the comparable vertical wind intensities and the fact that the two identified thermal sections followed the maximum slope of the hillside, as shown by the elevation contour curves, suggest that a single thermal structure, sounded at different positions and times by the two pilots, developed in the area. Further evidence is provided observing the agreement between the slope of the thermal sections in vertical x-z maps. Also, the average of the height over ground is similar between the two thermal sections (see Table 4.1), even if during

flight #10 the pilot progressively moved away from the slope, from approximately 70 m to 270 m rather than staying nearly at the same altitude over the mountain as the pilot of flight #9.

Considering the topography of the area, the thermal structure could have developed from the hot spot represented by the town of Pedavena, which land cover, occupied by buildings and cemented areas, clearly differs from the surroundings lawns and forested areas (see Figure 2.16). The buoyant plume was then probably orographically lifted by south-easterly winds along the maximum slope of the hillside, as suggested by the DTM contour lines that are perpendicular to the spiral trajectories.

4.3   20 September

Thermal sections #1, #2 of flight #5, and #3, #4, #5 of flight #7 on 20 September are analysed here, in the same way as done for 21 September. In this case, the two flights are not simultaneous (see Section 2.6.2 for a general description of the flights), thus the vertical profiles and the following results are not expected to give values as comparable as they were between the two flights on 21 September. Also, the two pilots followed quite different trajectories, as visibile in Figure 4.16 and as already explained in Section 2.6.2.

Figure 4.17 shows the identification of the thermal sections in the GPS altitude time series of flights #5 and #7, along with the corresponding height over ground time series. The pilot of flight #5 stayed within the upward flow for rather short time intervals (under 5 min for both the thermal sections, see Table 4.1) and height gains of approximately 86 m and 219 m respectively. Also, the maximum altitude of thermal sections in flight #5 is about 270 m lower than for flight #7. In the mid afternoon (flight #7), stronger updrafts have been found and the pilot flew inside them respectively for about 3 min, 5.5 min and 9.5 min and with altitude gains of 96 m, 374 m and 488 m. These differences may be attributed to the progressively stronger solar heating of the surface, as the weather changed from mainly cloudy in the morning to sunny in the afternoon (Section 2.6.2), enhancing thermal activity.

For both the flights, the second and third thermal sections started at lower altitudes with respect to the previous ones, but the pilots stayed inside them for a longer time.

The maximum height reached at the end of thermals #4 (1535 m) is comparable to that of thermal #5 (1495 m). It is probable that the pilot left the updraft at its top, even if it cannot be excluded that he decided not to completely taking advantage of it, maybe in order to head towards a different area. If the first alternative is valid, then an average between the two peaks could indicate the level of a temperature inversion, which prevented further air motion to upper levels. The sounding launched at Rivolto airport supports this consideration, as the lowest temperature inversion is detected above 1570 m (see Section 2.6.2). A higher level (2000 m) is suggested by the sounding in Milano, but this is located at a greater distance from Monte Avena than Rivolto (Figure 2.6).
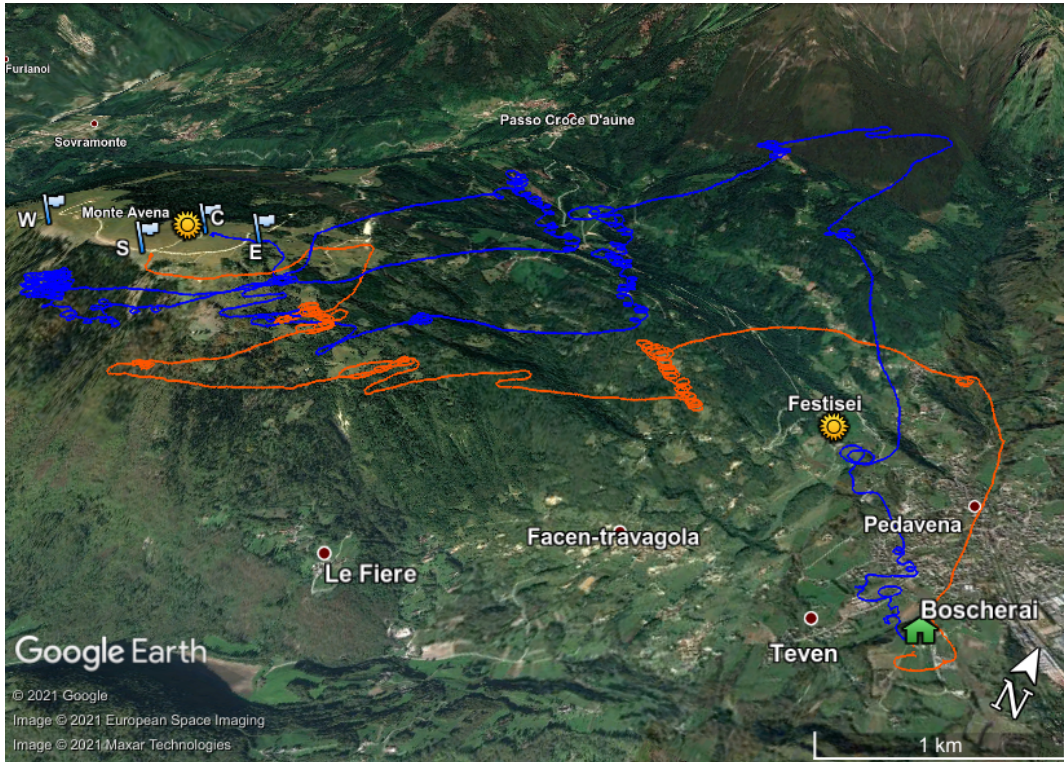
Figure 4.16: Google Earth image of the trajectories of flights #5 (orange) and #7 (blue) performed at different times on 20 September.
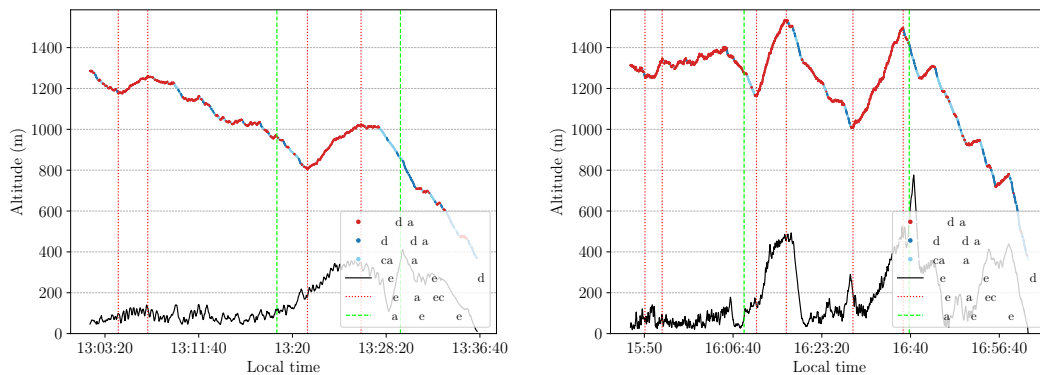
(a) GPS altitude time series of flight #5, with the identification of updraft, downdraft and calm air points and the thermal sections #1 and #2.

(b) GPS altitude time series of flight #7, with the identification of updraft, downdraft and calm air points and the thermal sections #3, #4, #5.

Figure 4.17: Identification of thermal sections of flights #5 and #7 on 20 September.

4.3.1   Vertical profiles

Vertical profiles of temperature, virtual potential temperature and water vapour mixing ratio are shown for flight #5 in Figure 4.18, Figure 4.20, Figure 4.22 and for flight #7 in Figure 4.19, Figure 4.21, Figure 4.23.
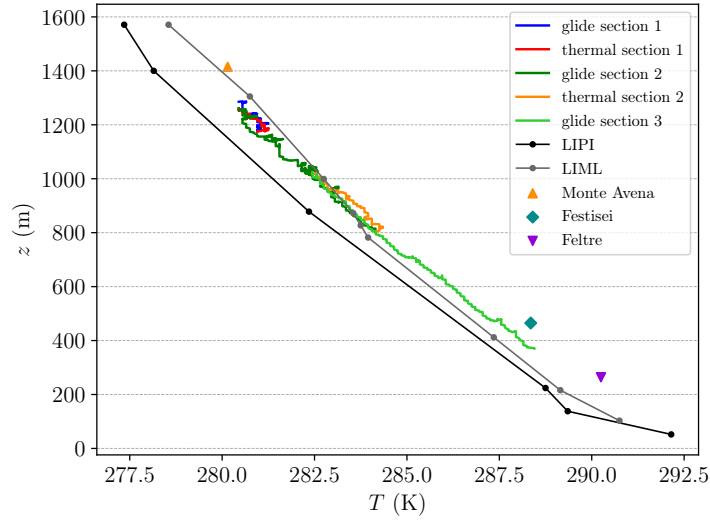
(a) Temperature vertical profile with soundings and surface weather stations data.
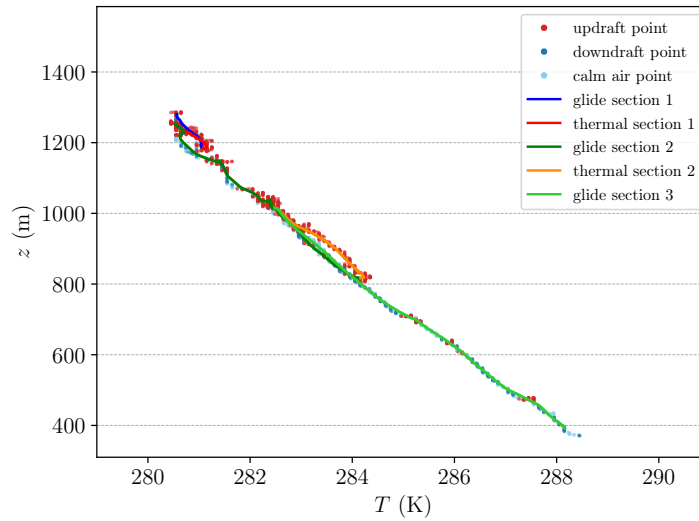
(b) Temperature vertical profile with a moving window (60 s) average.
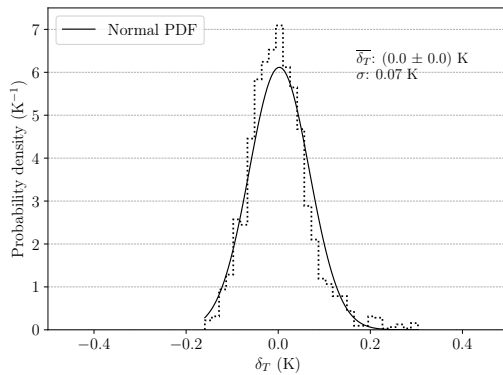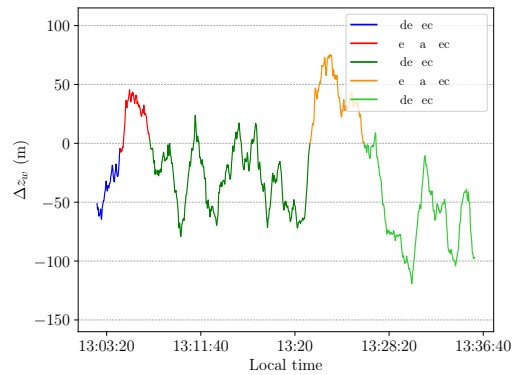
(c) Distribution of the residuals of temperature (d) Time series of the altitude intervals covered
     from the moving window average.   by the moving window average.

Figure 4.18: Temperature vertical profile of flight #5 (20 September).

115
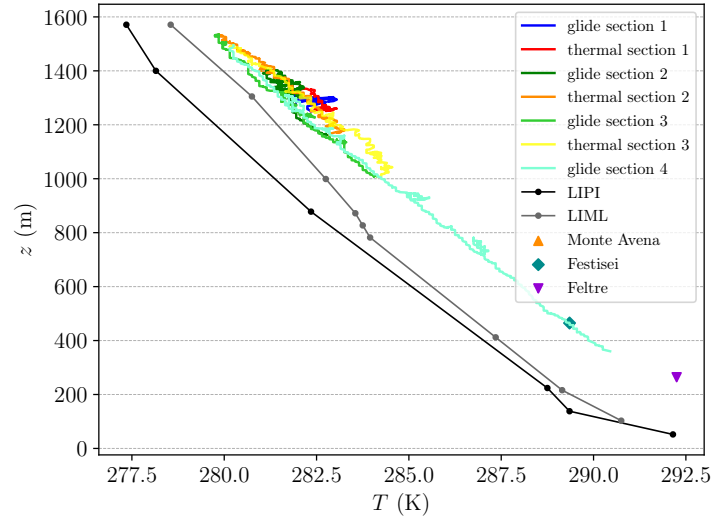
(a) Temperature vertical profile with soundings and surface weather stations data. The value of T measured at Monte Avena (1415 m), covered by the flight data, is 281.05 K.
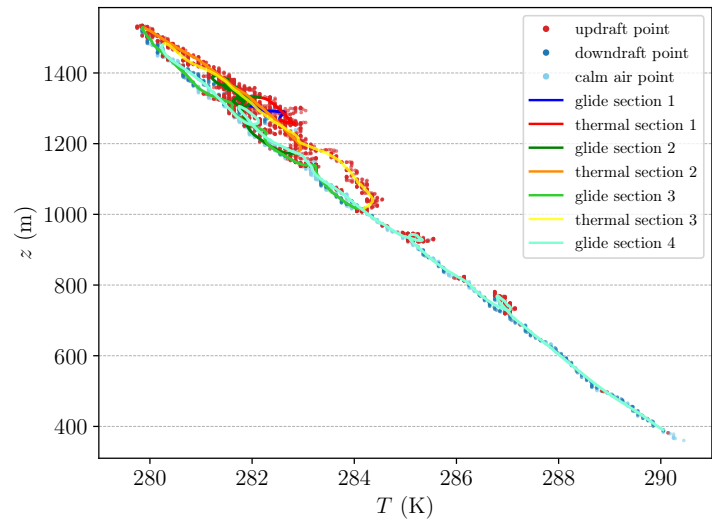
(b) Temperature vertical profile with a moving window (60 s) average.
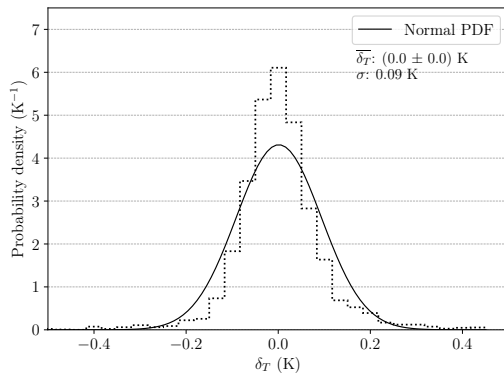
(c) Distribution of the residuals of temperature from the moving window average.
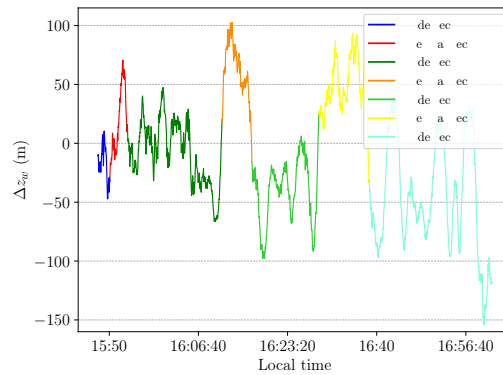
(d) Time series of the altitude intervals covered by the moving window average.

Figure 4.19: Temperature vertical profile of flight #7 (20 September).

The flight sections are identified with different colours as before: warm colours for thermal sections, and cold colours for glide sections at the beginning and ending of the flight, and between each thermal section. Three and four glide sections result for flight #5 and #7 respectively. Differently from 21 September, for flight #7 the thermal and the glide sections are not easily distinguishable, especially during the first part of the flight, due to the fact that the different sections share the same range of altitude values, approximately between 1000 m and 1500 m. Also, many updraft points are found not only in thermal sections, but also during most of glide sections 1 ans 2.

As for 21 September, also in the case of 20 September flight measurements, soundings and surface weather stations data show similar vertical profiles of T, θ_v and q (the latter to a lesser extent than for temperature).

Also in this case, the moving window average filters out local anomalies of T, θ_v and q, producing normally distributed residuals. Both the averaged temperature profiles appear linear with altitude, with a total temperature gradient, computed considering the highest/coldest and the lowest/warmest data points, that results $8.8 \, \mathrm{K \, km^{-1}}$ for flight #5, and $9.2 \, \mathrm{K \, km^{-1}}$ for flight #7. The temperature profile of flight #7 (Figure 4.19b) results shifted to higher temperatures than that of flight #5, as the former is measured in the mid afternoon.

The virtual potential temperature profile suggests a well mixed layer below about 800 m for flight #5 and 1000 m for flight #7. Above these levels, the boundary layer seems stable, with a gradient of approximately $3 \, \mathrm{K \, km^{-1}}$ (flight #5) and $2 \, \mathrm{K \, km^{-1}}$ (flight #7).

No dependence on altitude of the excess of T, θ_v and q between thermal and corresponding glide sections has been observed here, differently from the flights on 21 September. Indeed, in this case, the glide sections preceding and following the thermal sections were flown in different regions with respect to the supposed thermal structure (Figure 4.16), extending for several hundreds metres in different directions. This would invalidate the results, as not only the dependence on the altitude, but also the information derived by the horizontal structure of T, θ_v and q field would be present. This effect may affect also what has been presented for flights on 21 September, but to a lesser extent since the trajectories during glide sections are located at a closer distance from the thermal ones.
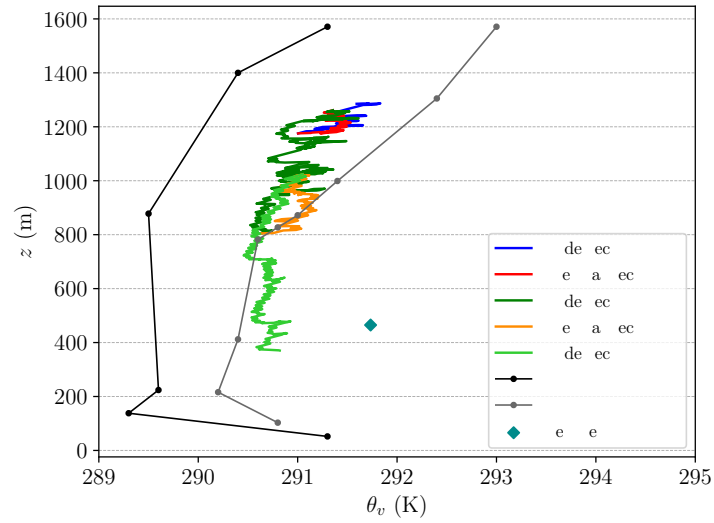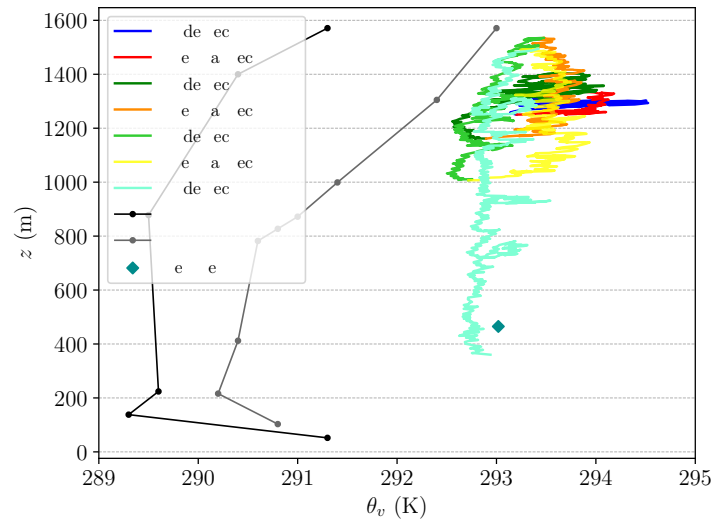
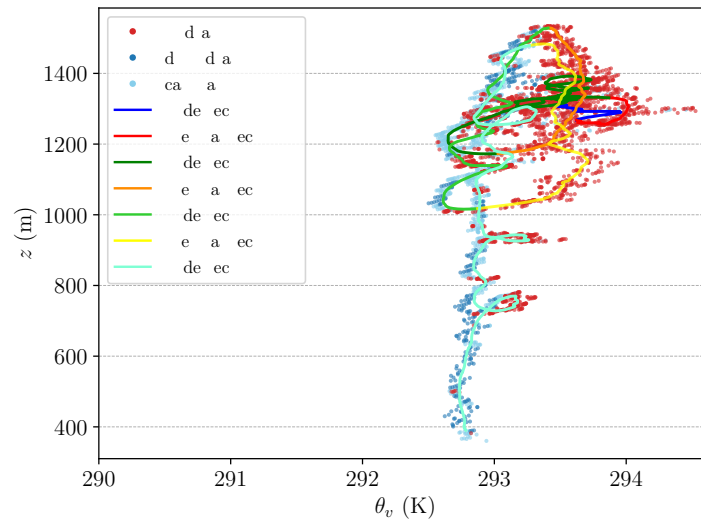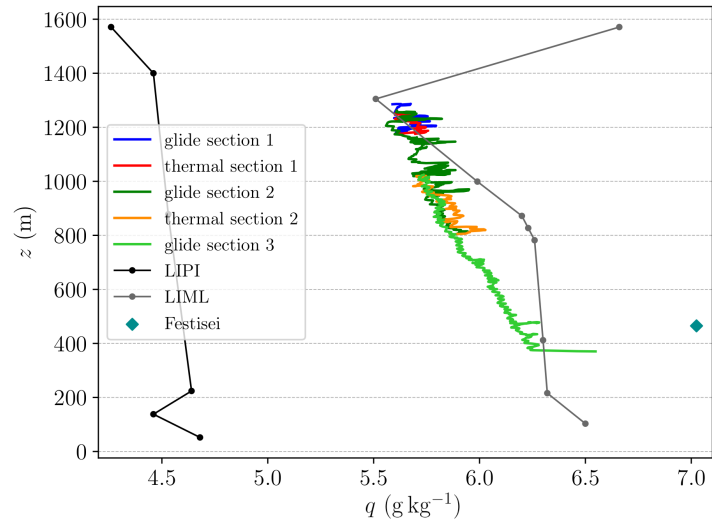(a) Virtual potential temperature vertical profile with soundings and surface weather stations data.
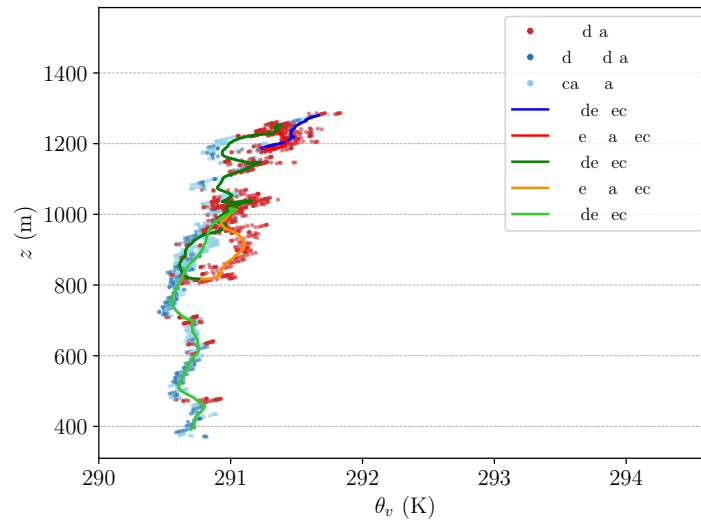
(b) Virtual potential temperature vertical profile with a moving window (60 s) average.

Figure 4.20: Virtual potential temperature vertical profile of flight #5 (20 September).

(a) Virtual potential temperature vertical profile with soundings and surface weather stations data.
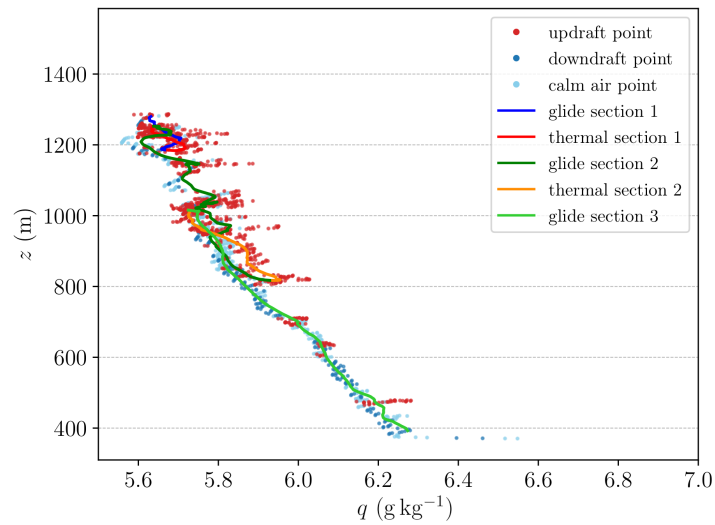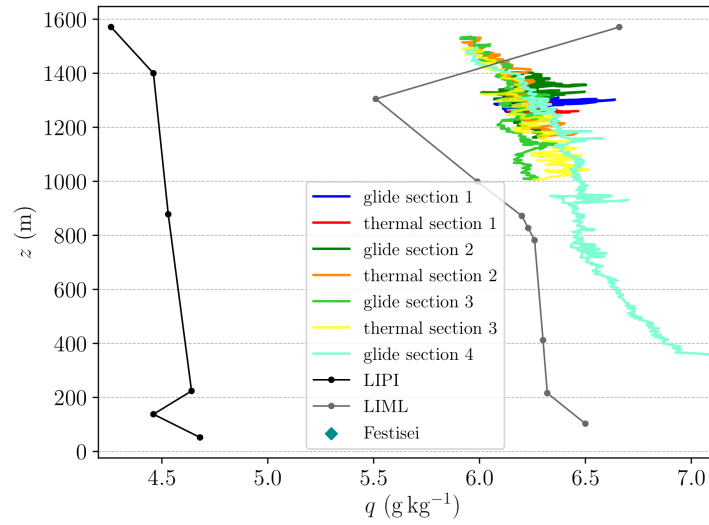

(b) Virtual potential temperature vertical profile with a moving window (60 s) average.

Figure 4.21: Virtual potential temperature vertical profile of flight #7 (20 September).

(a) Mixing ratio vertical profile with soundings and surface weather stations data.

(b) Mixing ratio vertical profile with a moving window (60 s) average.

Figure 4.22: Water vapour mixing ratio vertical profile of flight #5 (20 September).

(a) Mixing ratio vertical profile with soundings and surface weather stations data.
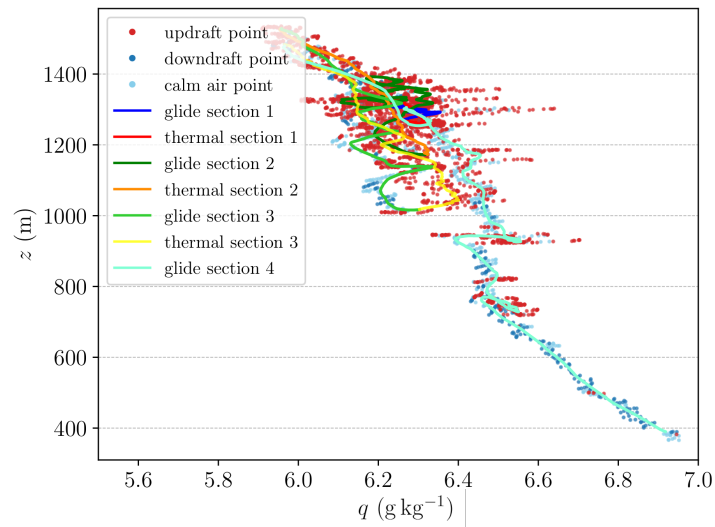
(b) Mixing ratio vertical profile with a moving window (60 s) average.

Figure 4.23: Water vapour mixing ratio vertical profile of flight #7 (20 September).

4.3.2   Skew-T Log-P diagrams

Skew-T Log-P diagrams are presented in Figure 4.24. As already observed from vertical profiles, the degree of agreement between flight data and soundings data is satisfactory, and other considerations are similar to those discussed for 21 September.
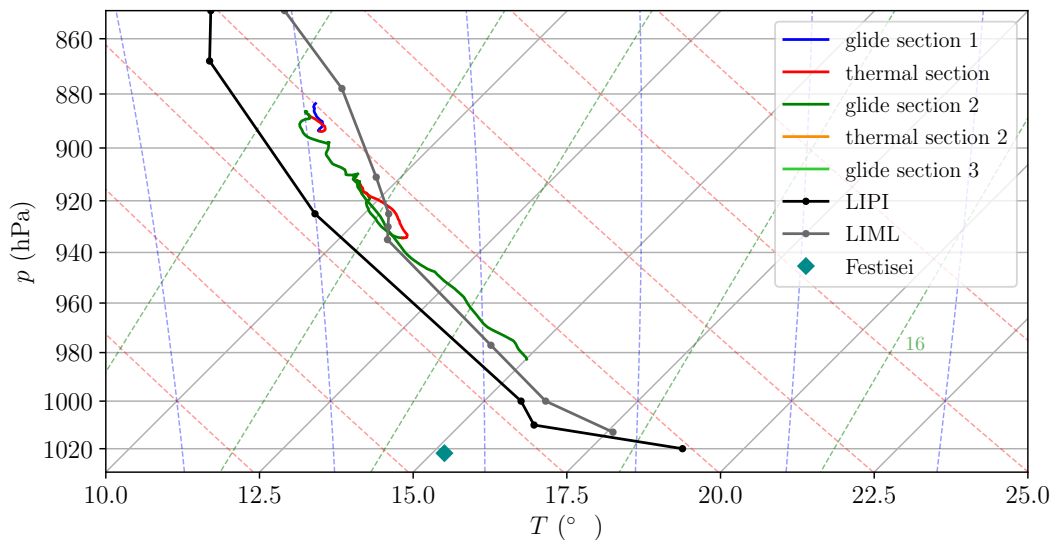
(a) Skew-T log-P diagram for flight #5.
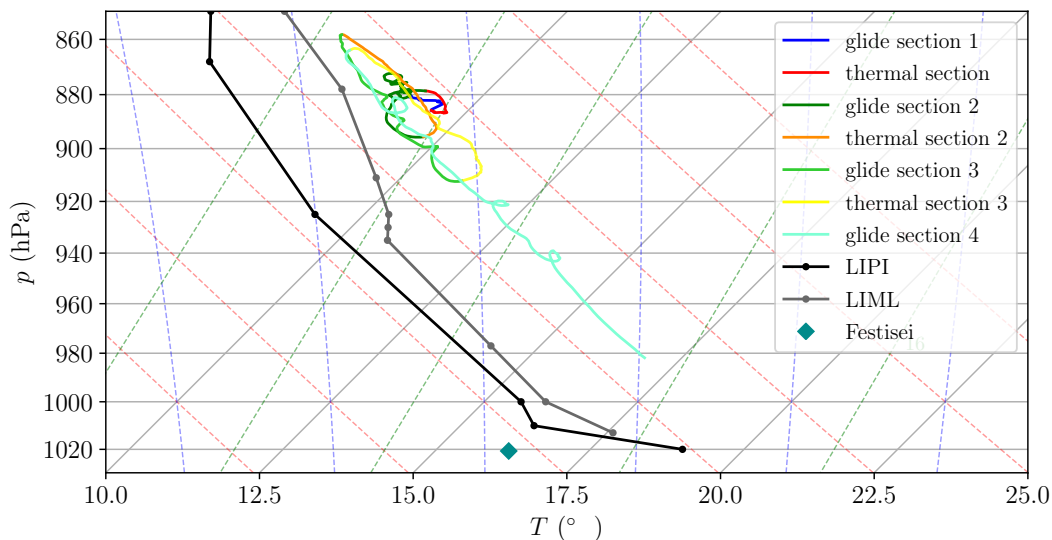
(b) Skew-T log-P diagram for flight #7.

Figure 4.24: Skew-T log-P diagrams for flights #5 and #7 (20 September), with soundings data and Festisei station data.

4.3.3   Maps

Maps that show the spatial distribution of T, θ_v, q and w_z along the trajectories of both flights in a limited region of the mountain are shown in Figure 4.26, Figure 4.27, Figure 4.28 and Figure 4.29. They have been realized as for the flights on 21 September. Even though the two flights are not simultaneous, they are shown together, in the same area of space, which contains the three most interesting thermal sections of 20 September (#2, #4 and #5), as they present the strongest updrafts, as underlined before. The section of each flight displayed in the maps is the portion of the time series limited by the two vertical green lines in Figure 4.17, and the number (#) of the thermal sections is indicated in the plots, along with black arrows pointing in the direction of the trajectory.

The same region and the flight trajectories are shown in a Google Earth view in Figure 4.25. The area corresponding to the three thermal sections, corresponding to spiral trajectories, is a hill close to Monte Avena and called Col Melon, where typically pilots can find ascending plumes of air. This was not the first slope identified as location for the measurements of the field campaign, but the supposed thermals encountered there have been considered interesting.

Indeed, they suggest that convection along the slope of Col Melon that overlooks the valley (thermal section #2) and over its top (thermal section #4 and #5) is likely to occur at different times: around 13:25 (#2) and 16:20 (#4 and #5), local times (see Table 4.1). They look like thermal structures that developed from a hot spot in the valley, were orographically lifted by south-easterly winds along the maximum slope of the hillside (see the DTM contour lines, perpendicular to the direction of the spirals), or a mix of the two, and then grew over the top of the mountain, as demonstrated by thermal sections #4 and #5. Height over ground of the three sections, as visible in Figure 4.17, increase going from the lower section (#2) to the upper ones: if the thermal structure formed in the area was a single structure, it detached from the slope at a certain point.

Figure 4.26 confirms that temperature in the afternoon is greater than at 1 pm, as higher altitudes of thermal section #5 present values of T similar to those at lower (and earlier) altitudes of thermal section #2. Also Figure 4.27 indicates a clear distinction between late morning and mid afternoon θ_v values.

Mixing ratio assumes higher values, again, for the thermals detected in the afternoon: in particular, in the lower part of thermal section #5. q at corresponding altitude levels outside the thermal section is found smaller, as expected.

Vertical velocity seems to confirm that the identification of thermals works effectively. The region surrounding the buoyant plumes seems characterized by weak downdrafts and rather calm air (cyan-green colours, about $-0.5\,\mathrm{m\,s^{-1}}$), while inside

thermal sections w_z reaches about $4\,\mathrm{m\,s^{-1}}$. It has to be mentioned that local anomalies of w_z might have been removed by the moving window average applied to it (see Section 3.3.7).
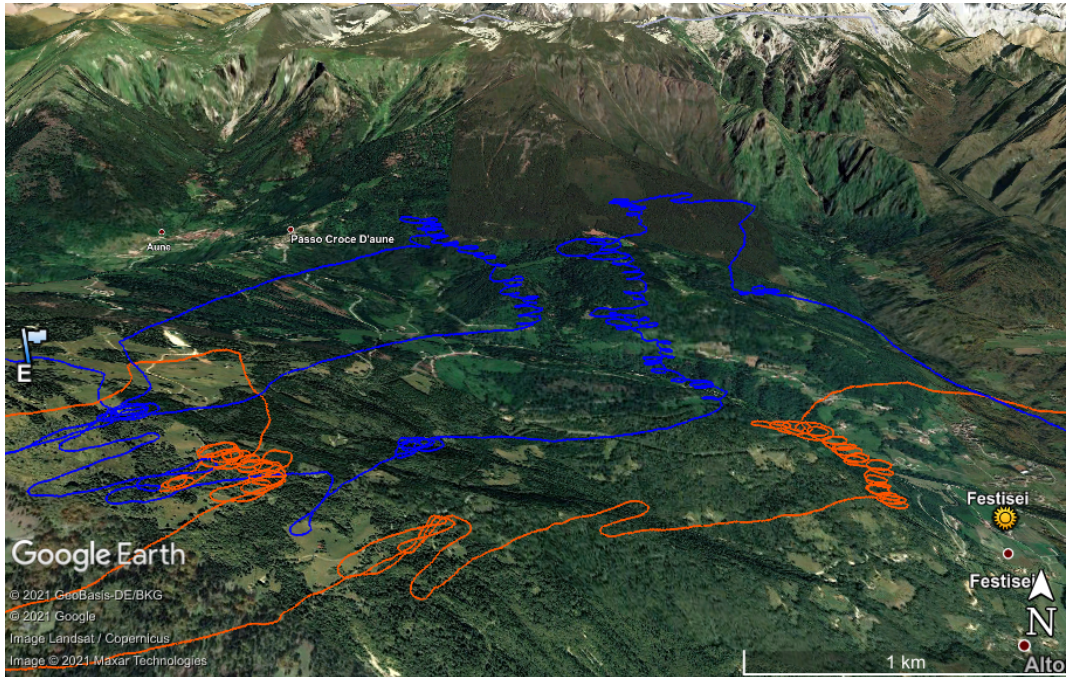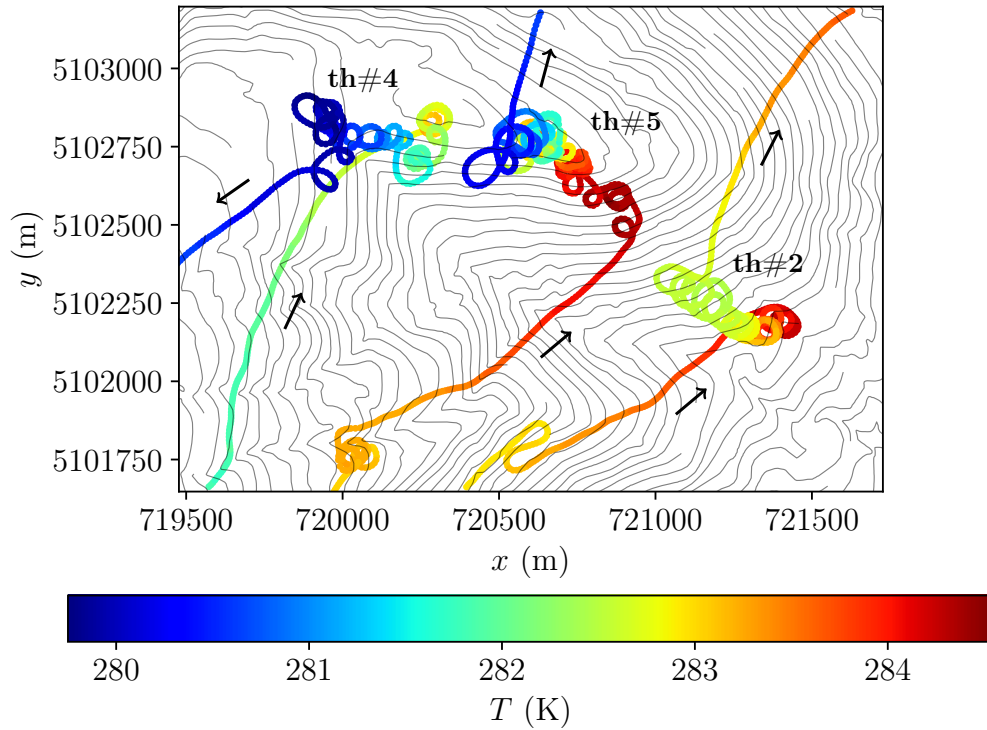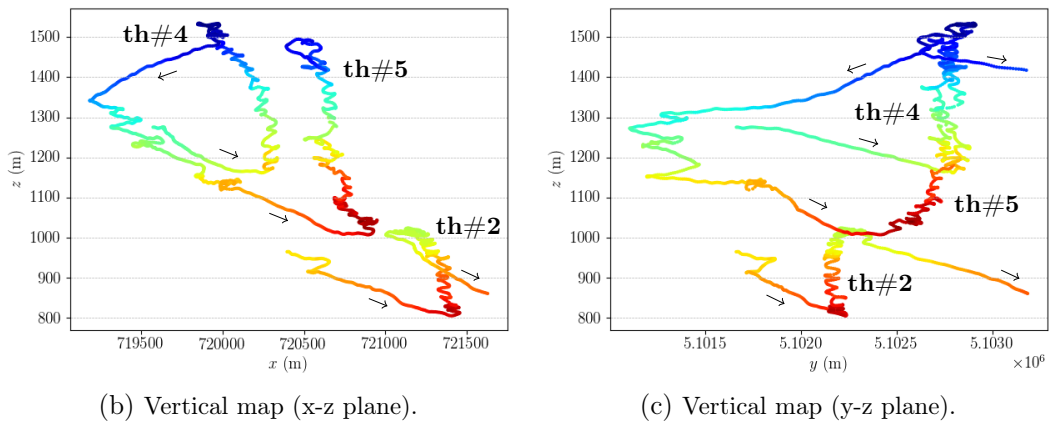

Figure 4.25: Google Earth image of the section of trajectories of flights #5 (orange) and #7 (blue) performed at different times on 20 September, shown in the maps below.
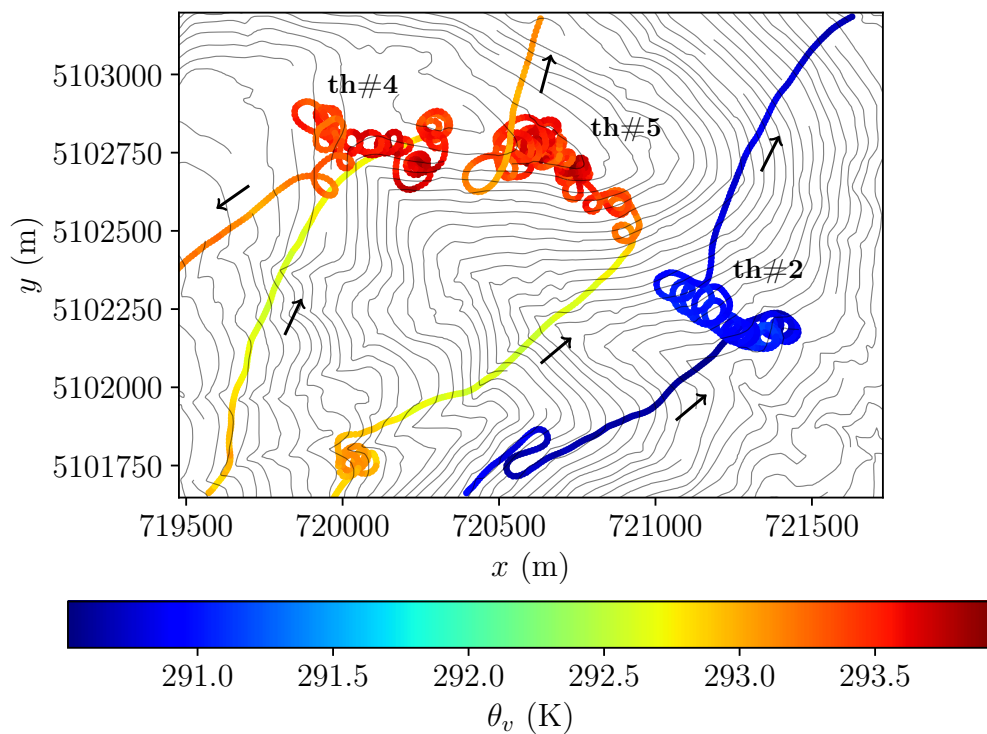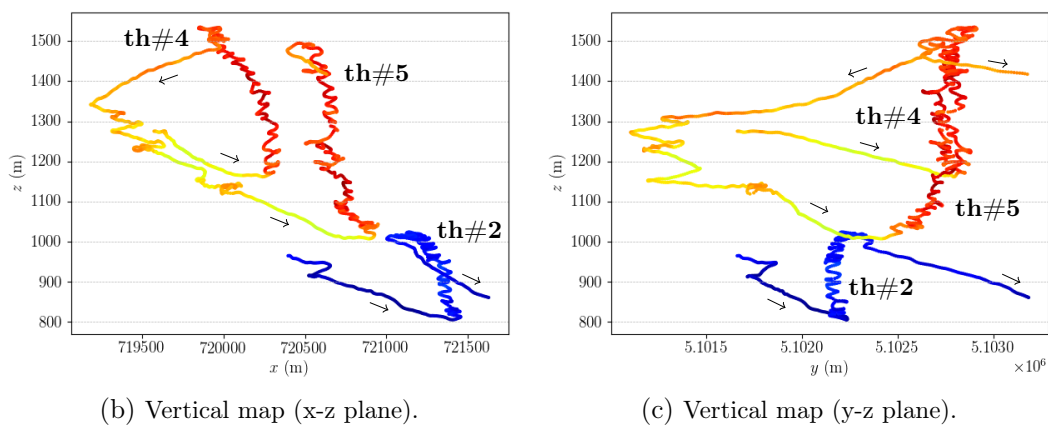
(a) Horizontal map.

(b) Vertical map (x-z plane).

(c) Vertical map (y-z plane).

Figure 4.26: Temperature maps of a section of flights #5 and #7 (20 September).

(a) Horizontal map.

(b) Vertical map (x-z plane).

(c) Vertical map (y-z plane).

Figure 4.27: Virtual potential temperature maps of a section of flights #5 and #7 (20 September).
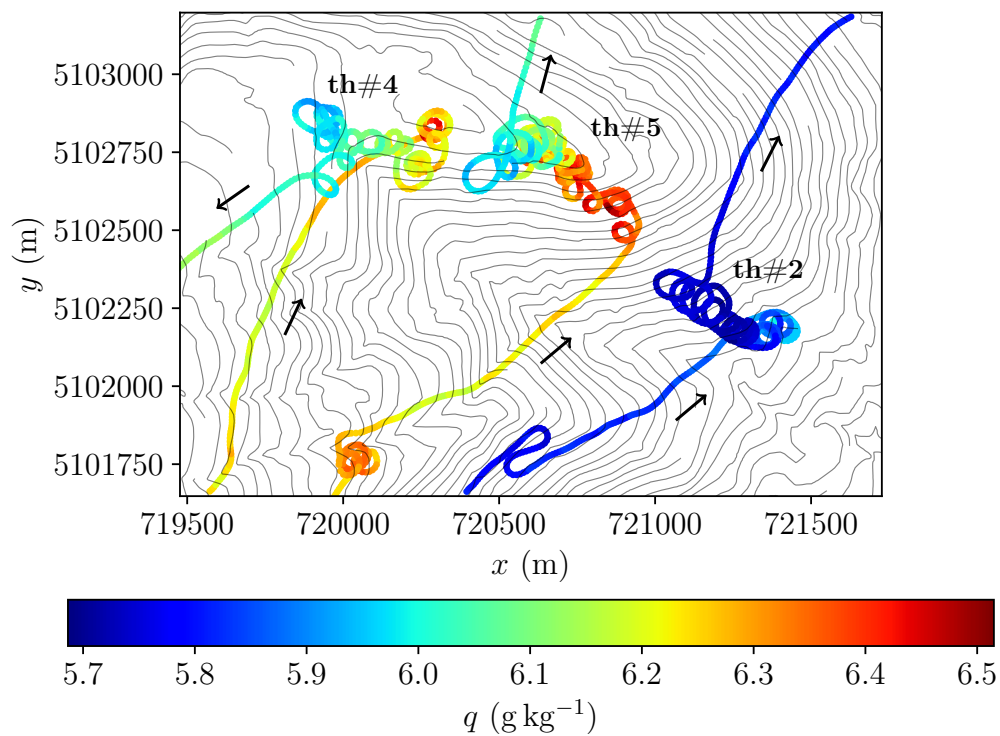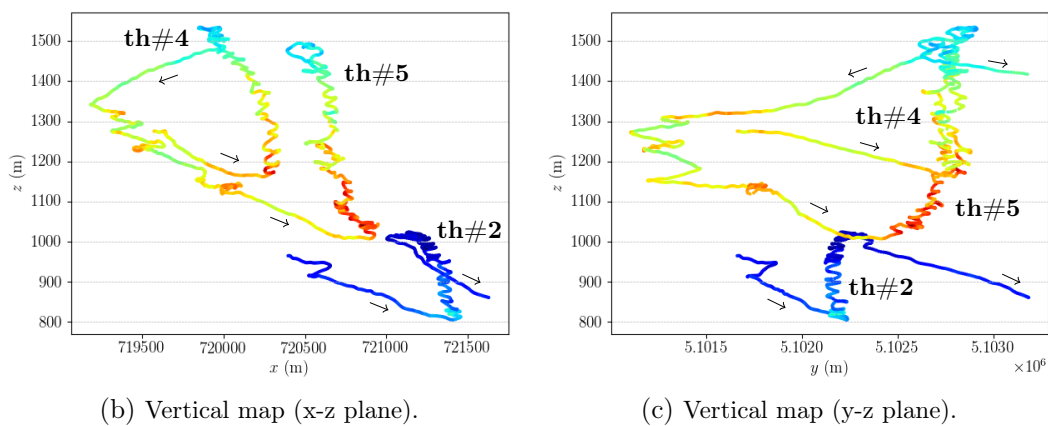
(a) Horizontal map.

(b) Vertical map (x-z plane).   (c) Vertical map (y-z plane).

Figure 4.28: Mixing ratio maps of a section of flights #5 and #7 (20 September).
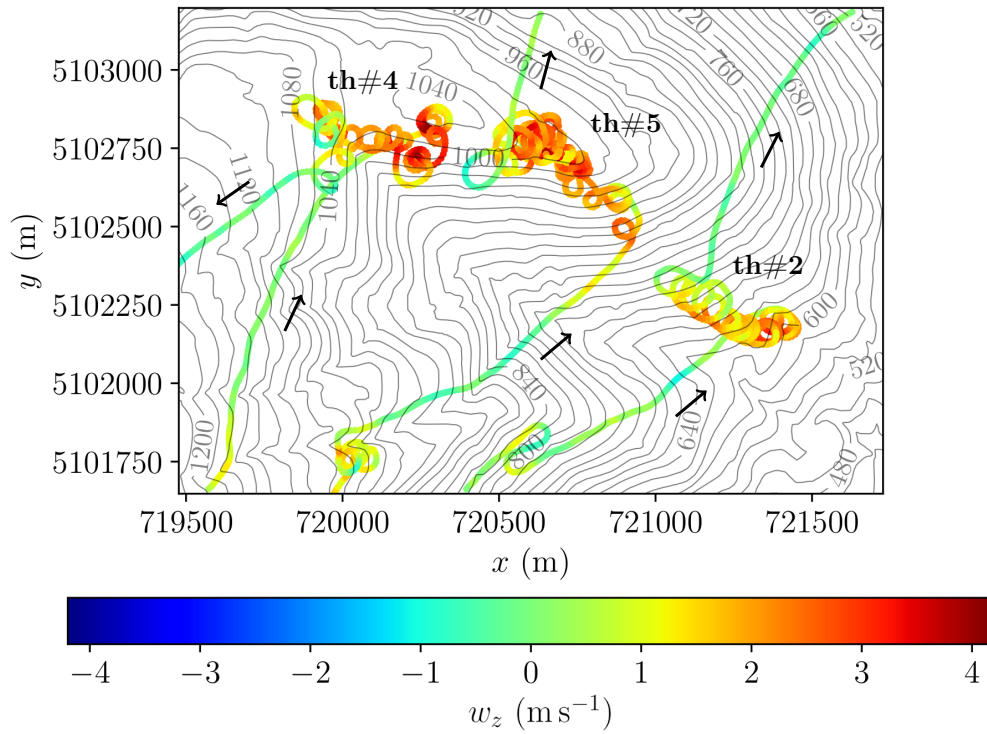
(a) Horizontal map.
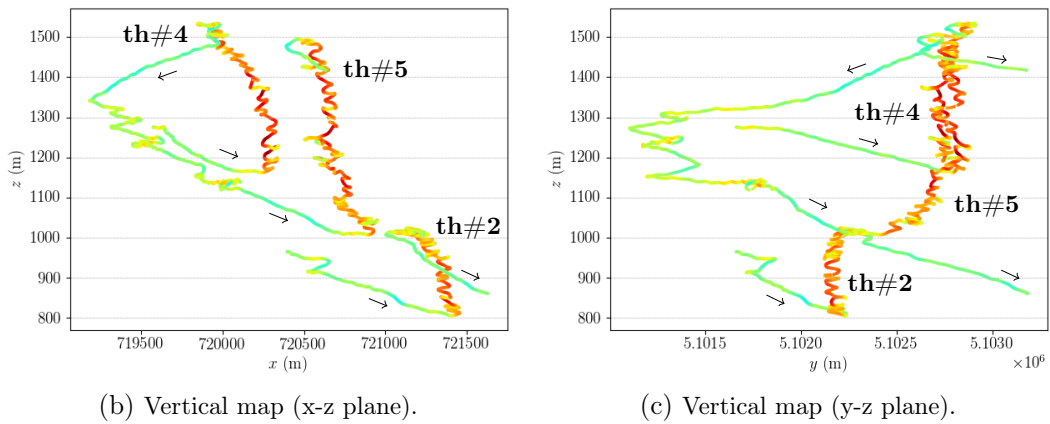
(b) Vertical map (x-z plane).

(c) Vertical map (y-z plane).

Figure 4.29: Vertical wind maps of a section of flights #5 and #7 (20 September).

4.4   30 September

The same graphical results have been realized for flight #19, performed in the early afternoon of 30 September, along the eastern side of Monte Avena (see Figure 2.29 for the Google Earth view of the trajectory). Figure 4.30 shows the GPS altitude time series with the identification of the three thermal sections. Again, the identification method seems to work properly, as the three thermal sections contain only updraft (red) points.

The meteorological conditions of the day (see Section 2.6.7) allowed to find only three modest ascent air areas, which lasted approximately between 2.5 min and 3.5 min, with an average height gain of 125 m. The pilot stayed progressively more far away from the slope, as visible from the height over ground time series of Figure 4.30.

Also in this case, vertical profiles, Skew-T Log-P diagrams have been realized and are presented below. They show similar behaviours with respect to other flights, thus horizontal and vertical maps of T, θ_v, q and w_z are not shown.
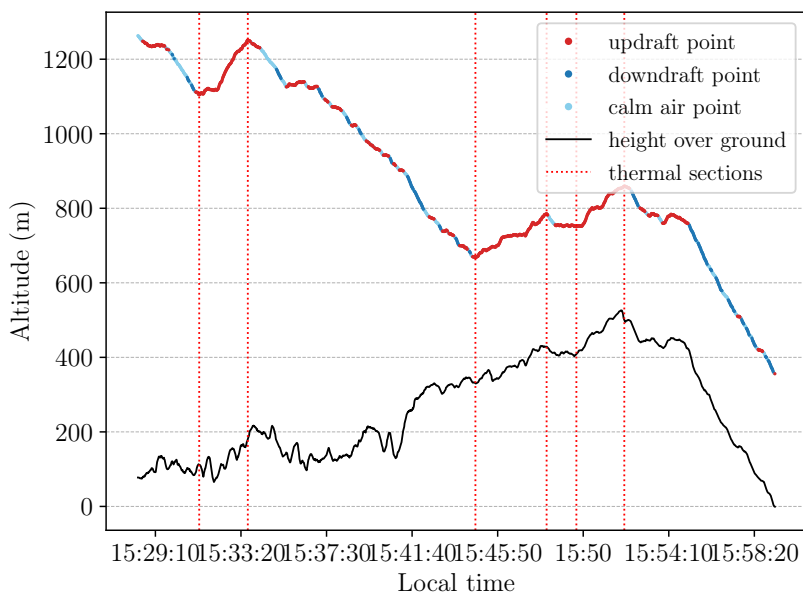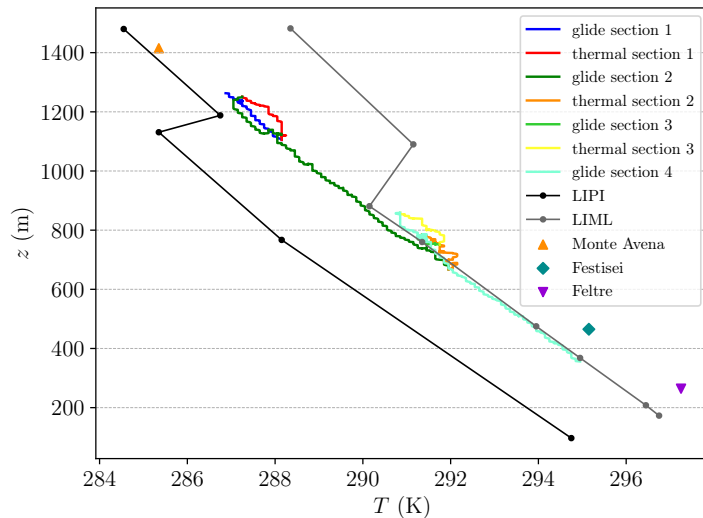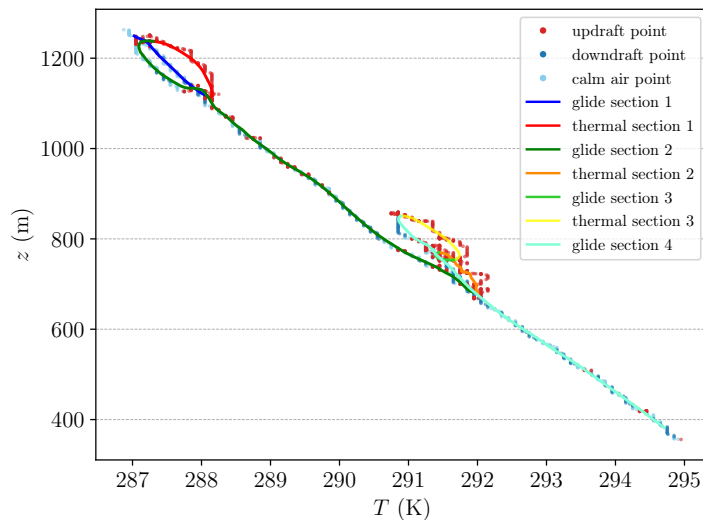

Figure 4.30: Identification of thermal sections #8, #9 and #10 of flights #19 on 30 September.
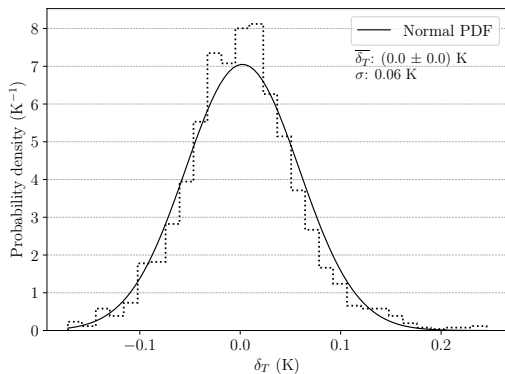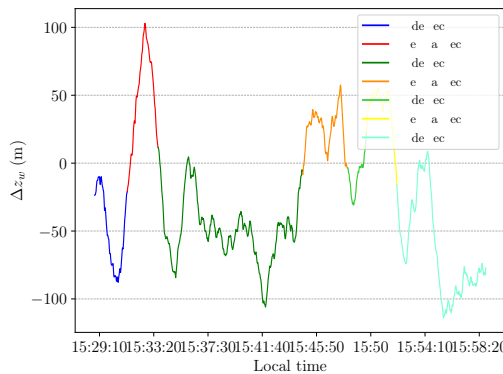
4.4.1   Vertical profiles

(a) Temperature vertical profile with soundings and surface weather stations data.

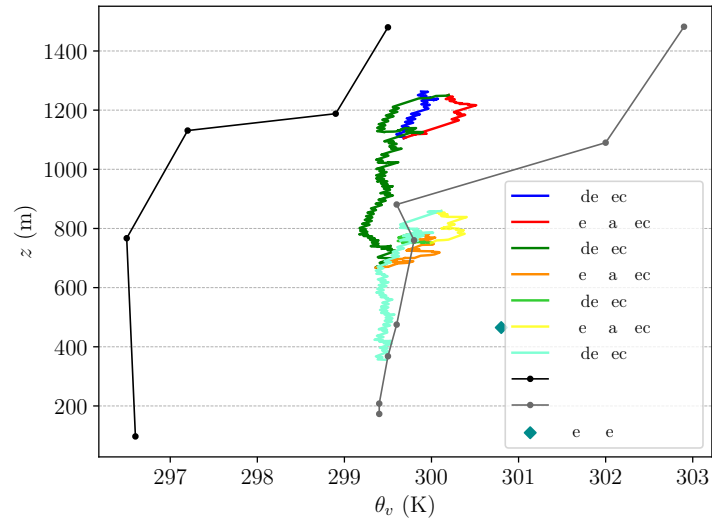(b) Temperature vertical profile with a moving window (60 s) average.

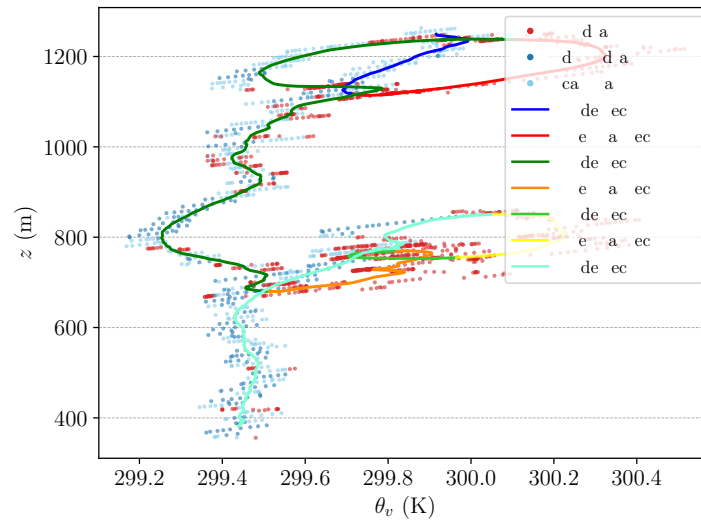(c) Distribution of the residuals of temperature from the moving window average.

(d) Time series of the altitude intervals covered by the moving window average.

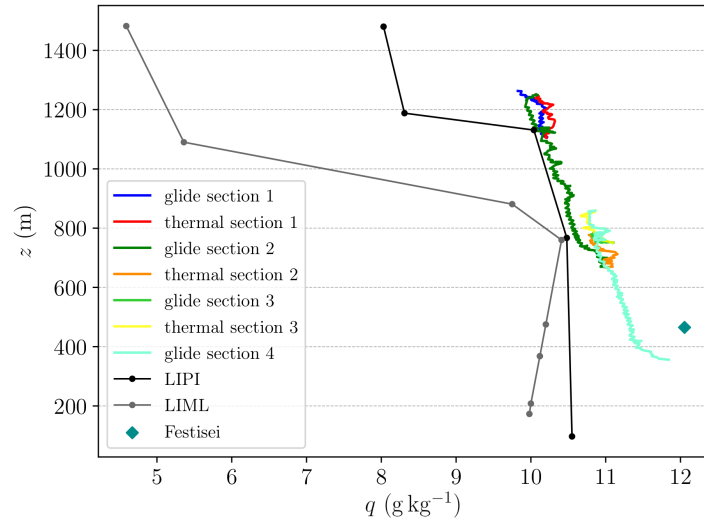Figure 4.31: Temperature vertical profile of flight #19 (30 September).

(a) Virtual potential temperature vertical profile with soundings and surface weather stations data.
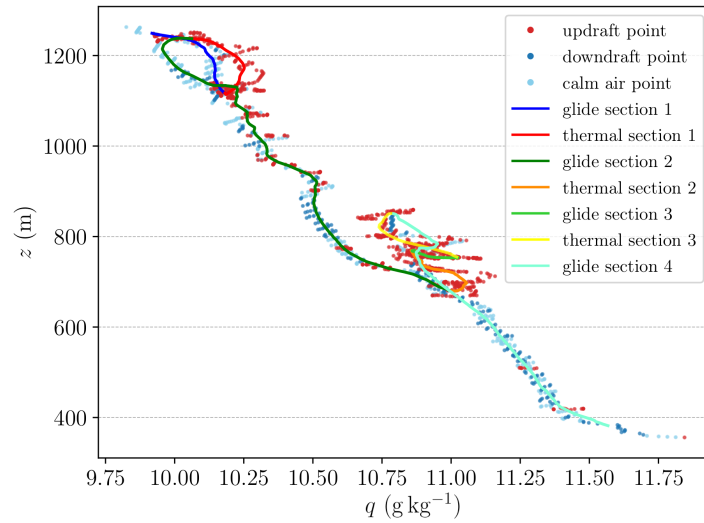

(b) Virtual potential temperature vertical profile with a moving window (60 s) average.

Figure 4.32: Virtual potential temperature vertical profile of flight #19 (30 September).

(a) Mixing ratio vertical profile with soundings and surface weather stations data.

(b) Mixing ratio vertical profile with a moving window (60 s) average.

Figure 4.33: Water vapour mixing ratio vertical profile of flight #19 (30 September).
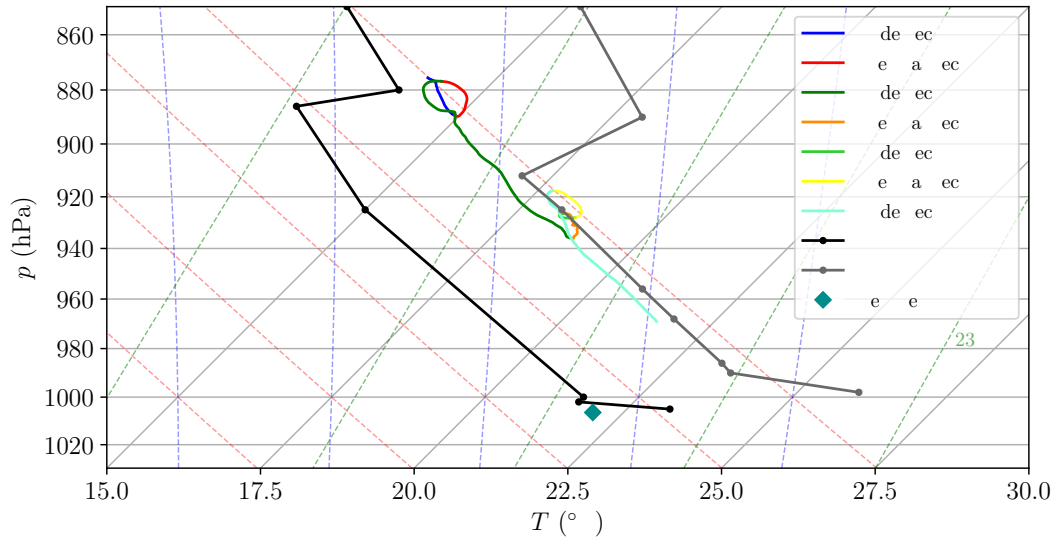
4.4.2 Skew-T Log-P diagrams

Figure 4.34: Skew-T log-P diagram for flights #19 (30 September), with soundings data and Festisei station data.

4.5   Correlation between w_z and θ_v

A preliminary investigation into the relationship between the vertical component of the wind w_z and the virtual potential temperature θ_v has been conducted. Indeed, it can be generally expected that updrafts and downdrafts occur in presence of relative high and low virtual temperature values respectively, since the latter can represent a direct measurement of the buoyancy of air parcels (Williams and Hacker, 1992). Thus, the potential correlation between the two variables has been tested here by means of scatterplots.

The scattered data points are those of the flights performed on 21, 20 and 30 September. The colour division is the same adopted in vertical profiles for distinguishing the thermal sections (warm colours) from the glide sections (cold colours), with the same tones correspondence as before.

As before, θ_v are the original (not averaged) data points, while w_z is the 10 points moving window averaged as explained in Section 3.3.7. Updraft ($w_z > 0.4\,\mathrm{m\,s^{-1}}$), calm air ($-0.4\,\mathrm{m\,s^{-1}} \leq w_z \leq 0.4\,\mathrm{m\,s^{-1}}$) and downdraft ($w_z < -0.4\,\mathrm{m\,s^{-1}}$) points, as defined in Section 4.1, are simply indicated by the corresponding y-axis values.

To evaluate the degree of correlation between the two variables, the Pearson's linear correlation coefficient and the Spearman's rank-order correlation coefficient, along with corresponding p-values, have been computed and are shown in the plots panels (respectively as r and s). The first measures the degree of linear correlation between the two variables, while the second generally measures the extent to which the function describing the relationship is motonic. The lower the p-value, that results always many orders of magnitudes smaller than zero, the higher the coefficients significance.

The values of the coefficients and the pattern of scattered data points may suggest a moderate correlation between w_z and θ_v. This seems to be valid for points belonging not only to thermal sections, but also to glide ones, as expected. Further investigations would be necessary to better understand the nature of the potential correlation between these two variables, for example looking for a suitable scaling operation to be applied to them.
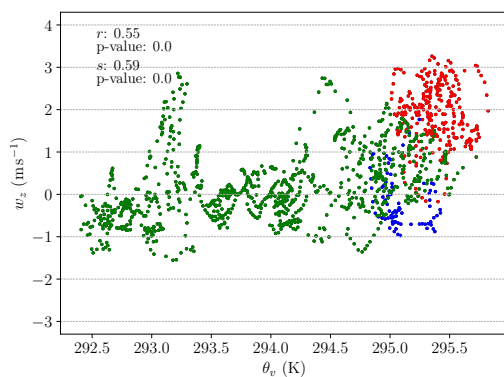
(a) Scatterplot for flight #9 (21 September).
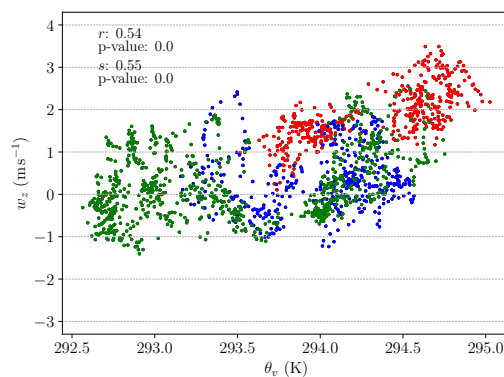
(b) Scatterplot for flight #10 (21 September).
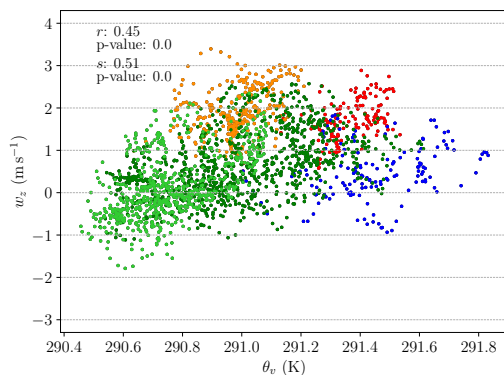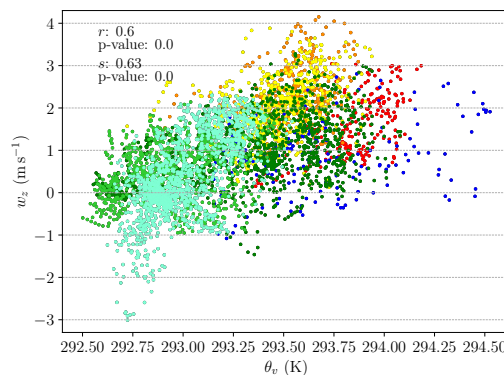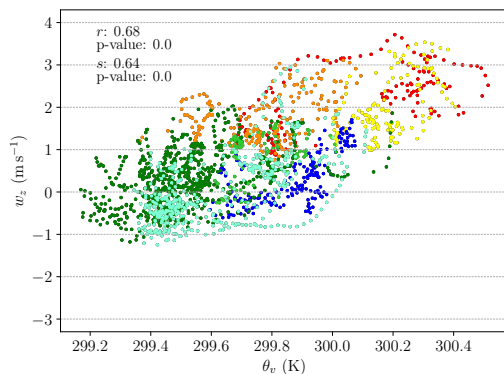
(c) Scatterplot for flight #5 (20 September).

(d) Scatterplot for flight #7 (20 September).

(e) Scatterplot for flight #19 (30 September).

Figure 4.35: Scatterplots between vertical wind and virtual potential temperature for the flights containing thermal sections (21, 20, 30 September, ordered as presented in this chapter). The colours are the same as in the vertical profiles.

4.6   Summary

The method proposed in Section 4.1 and used throughout Chapter 4 for the identification of thermals, based on the paraglider key-property of being engine-free, has proved to effectively work, as it is able to recognise flight sections with vertical air velocity above a certain threshold, here set to $0.4\,\mathrm{m\,s^{-1}}$. The identified thermal sections correspond to spiral trajectories.

Vertical profiles of T, θ_v and q have been analysed and compared to soundings and surface weather stations data. The agreement with the latter has found to be good, and the moving window averaged profiles are able to filter out the variability of the original measurements, showing the dominant vertical structure of the boundary layer. The mean vertical temperature gradients seem comparable with those expected on average, and virtual potential temperature vertical profiles have resulted to be useful to roughly identify the depth of the mixed layer. To this extent, the paragliders instrumented with the chosen instruments seem a promising technique to measure atmospheric variables and extract interesting information.

The difference between the different sections of the flights, classified as glide or thermal sections, is clearly visible in the vertical profiles. In addition, the thermal sections on 21 September have shown that the ΔT, $\Delta\theta_v$ and Δq excesses between air inside thermals and environmental air are positive and tend to decrease with altitude, suggesting a corresponding decreasing strength of the thermals. Further comparisons between glide and thermal sections have been made observing horizontal and vertical maps of T, θ_v, q and w_z. From the conducted analysis, the two thermal sections on 21 September seem to belong to the same thermal structure, while on 20 September the development of thermal activity above the hillside has been observed at two different times of the day (late morning and mid afternoon).

Table 4.1 shows the properties of duration, altitude gain and height over ground presented by the analysed thermal sections, while the vertical wind intensity is displayed in the horizontal and vertical wind maps. To compare thermal sections belonging to different days, a suitable scaling should be performed and would represent an interesting development of the work. This would be useful also for a comparison with thermals analysed in previous works, that generally present results involving scaled variables.

A further development of the analysis could be the characterisation of the horizontal dimensions of thermals (i.e. their radius), that would be possible starting from the analysis of the shape of spiral trajectories in thermals (i.e. open circles), as done in Ultsch (2012) and Allen and Lin (2007). This would allow also a study on the fine structure of thermals and the derivation of wind drift (see Section 1.4).

Conclusions

Since the present study is based on measurements of atmospheric variables collected with non-convential instruments mounted on board paragliders, several aspects concerning the paragliding technique and materials had to be taken into consideration to plan the field campaign, to choose a suitable location and the proper experimental set-up. Future studies could benefit from what have been done in this sense.

The field campaign successfully resulted in 19 flights performed on seven days between 17 and 30 September on Monte Avena. On three of these days, thermal structures have been detected and analysed.

The non-conventional adopted instruments have shown several issues in measuring the atmospheric variables, both in terms of expected values, of elevated adjustment time after take-off and of calibration problems. However, an explanation or a solution have been proposed for each of the problems. Instruments resolution and sensitivity to small oscillations of the measured quantities suggest that, once solved the above problems, they could represent a valid choice for airborne measurements from paragliders. This could be better assessed by further analysing their quality and reliability, maybe with ad-hoc laboratory experiments or wind-tunnel controlled conditions.

A new method for identifying thermals has been applied and considered rather reliable. The visualisation of the trajectories recorded by the GPS receivers, the analysis of vertical profiles of the atmosphere and the variability of the atmospheric variables in the three space dimensions have produced interesting results. The measurements of T, θ_v and q have been found to be in good agreement with the vertical profiles from the sounding stations in Rivolto and in Milano, and with data collected by three surface weather stations. The flight data appear useful to populate the lower part of the soundings, and would have interested also upper atmospheric layers, if proper synoptic and local conditions had allowed to reach higher altitudes. Flight data have turned out to properly measure both the steady state of the atmosphere, giving gradients values compatible with those expected on average, and the thermal structures characterising the convective boundary layer over complex terrain during

the daytime. The next step could be to collect a greater number of simultaneous data above the slope, in order to apply a space interpolation of the measured quantities, maybe with residual kriging techniques. The GPS recorded trajectories and horizontal and vertical maps analysed have been useful for evaluating the evolution in time and space of the thermal structures, the interesting thermodynamic variables and the vertical wind. The detected thermals have presented mean vertical wind intensities about $2\,\mathrm{m\,s^{-1}}$, with peaks at $4\,\mathrm{m\,s^{-1}}$, and temperature excess with respect to environmental air decreasing from $1.0\,\mathrm{K}$ to $0.1\,\mathrm{K}$ with altitude. Further analysis on the fine structure of thermals and the computation of wind drift would help to complete the picture.

From the analysis of the results, the new method constiting in collecting atmospheric data by means of an instrumented paraglider has turned out to be promising, both for the identification and characterisation of thermal structures in the mountain boundary layer, and for the study of the basic state of the atmosphere.

However, the work has to be considered as a starting point for further investigations into the validity of the proposed technique and the study of thermal structures. The work would also benefit from comparisons with numerical simulations and meteorological models adapted to the area of interest.

Improvements for future field campaigns on thermal structures could be given by additional data recorded by ground-based instruments at different altitudes along the slope, maybe adopting sonic anemometers for turbulence measurements. Tethered balloons, ceilometers and lidars could also complement the measurements collected by paragliders. The latter could also represent a new method for exploratory field campaigns at new sites of interest for studies on thermals: as the paraglider is a portable and relatively inexpensive flying vehicle, and for the advantages related to its engine-free nature, it could be easily used to preliminarly probe hillsides not previously analysed, in order to identify the most interesting slopes in terms of upslope currents. A complete and more expensive field campaign with the other instruments could then be conducted, benefiting from the previous inspection made by paragliders.

Acknowledgements

Bibliography

Alken, P., Thébault, E., Beggan, C. D., and Zhou, B. (2021). International Geomagnetic Reference Field: the thirteenth generation. *Earth, Planets and Space*, 73(49). doi:10.1186/s40623-020-01288-x.

Allen, M. J. and Lin, V. (2007). Guidance and Control of an Autonomous Soaring UAV. *Tech. Rep. TM-2007-214611, NASA Dryden Flight Research Center*.

Ambaum, M. H. P. (2020). Accurate, simple equation for saturated vapour pressure over water and ice. *Quarterly Journal of the Royal Meteorological Society*, 2020:1–7. doi:10.1002/qj.3899.

Arnold, A. (1976). A Lapse Rate Depiction for Clear-Air Convection. *Journal of Applied Meteorology and Climatology*, 15(11):1189–1192. doi:10.1175/1520-0450(1976)015<1189:ALRDFC>2.0.CO;2.

Betke, K. (2001). The NMEA 0183 Protocol. `https://www.tronico.fi/OH6NT/docs/NMEA0183.pdf`. Accessed: 16-04-2021.

Caughey, S. J. and Palmer, S. G. (1979). Some aspects of turbulence structure through the depth of the convective boundary layer. *Quarterly Journal of the Royal Meteorological Society*, 105(446):811–827. doi:10.1002/qj.49710544606.

Chernov, Y. V. (1965). Study of ascending air flows by gliders. *Trudy TsAO (Proc. Central Aerological Observatory)*, 63:70–76. in Russian.

Cho, A., Kim, J., Lee, S., and Kee, C. (2011). Wind Estimation and Airspeed Calibration using a UAV with a Single-Antenna GPS Receiver and Pitot Tube. *IEEE Transactions on Aerospace and Electronic Systems*, 47(1):109–117. doi:10.1109/TAES.2011.5705663.

Crawford, T. L., Dobosy, R. J., and Dumas, E. J. (1996). Aircraft wind measurement considering lift-induced upwash. *Boundary-Layer Meteorology*, 80:79–94. doi:10.1007/BF00119012.

Crum, T. D., Stull, R. B., and Eloranta, E. W. (1987). Coincident lidar and aircraft observations of entrainment into thermals and mixed layers. *Journal of Applied Meteorology and Climatology*, 26(7):774–788. doi:10.1175/1520-0450(1987)026<0774:CLAAOO>2.0.CO;2.

De Marco, A. and Coiro, D. P. (2017). Elementi di Dinamica e simulazioni di volo. Quaderno 3 – Quaternione dell'orientamento di un velivolo. `http://wpage.unina.it/agodemar/DSV-DQV/DSV-DQV_Quaderno_3.pdf`. Accessed: 23-04-2021.

Deardorff, J. W., Willis, G. E., and Lilly, D. K. (1969). Laboratory Investigation of Non-steady Penetrative Convection. *Journal of Fluid Mechanics*, 35:7–31. doi:10.5065/D6JW8BSB.

Free Aero (2016). Instruments. *Free Aero – Worldwide Paragliding and Paramotoring Magazine*.

Fédération Aéronautique Internationale – International Gliding Commission (2020). Technical Specification For IGC-Approved GNSS Flight Recoders. `https://www.fai.org/sites/default/files/igc_fr_specification_2020-11-25_with_al6.pdf`. Accessed: 17-04-2021.

Garman, K. E., Wyss, P., Carlsen, M., Zimmerman, J. R., Stirm, B. H., Carney, T. Q., R., S., and B., S. P. (2008). The Contribution of Variability of Lift-induced Upwash to the Uncertainty in Vertical Winds Determined from an Aircraft Platform. *Boundary-Layer Meteorology*, 126:461–476. doi:10.1007/s10546-007-9237-y.

Grossman, R. L. (1984). Bivariate conditional sampling of moisture flux over the tropical ocean. *Journal of Atmospheric Sciences*, 41:3238–3253.

Hocut, C. M., Liberzon, D., and Fernando, H. J. S. (2015). Separation of upslope flow over a uniform slope. *Journal of Fluid Mechanics*, 775:266–287. doi:10.1017/jfm.2015.298.

Hodgson, M. E. (2020). On the accuracy of low-cost dual-frequency GNSS network receivers and reference data. *GIScience & Remote Sensing*, 57(7):907–923. doi:10.1080/15481603.2020.1822588.

Hooper, W. P. and Eloranta, E. W. (1985). Lidar Measurements of Wind in the Planetary Boundary Layer: The Method, Accuracy and Results from Joint Measurements with Radiosonde and Kytoon. *Journal of Climate and Applied Meteorology*, 27(7):990–1001.

Hunt, J. C. R., Fernando, H. J. S., and Princevac, M. (2003). Unsteady Thermally Driven Flows on Gentle Slopes. *Journal of the Atmospheric Sciences*, 60(17):2169–2182. doi:10.1175/1520-0469(2003)060<2169:UTDFOG>2.0.CO;2.

International Virtual Aviation Organisation (2021). Airspeed Definition. `https://mediawiki.ivao.aero/index.php?title=Airspeed_definition`. Accessed: 23-04-2021.

Khalsa, S. J. S. and Greenhut, G. K. (1985). Conditional Sampling of Updrafts and Downdrafts in the Marine Atmospheric Boundary Layer. *Journal of Atmospheric Sciences*, 42(23):2550–2562. doi:10.1175/1520-0469(1985)042<2550:CSOUAD>2.0.CO;2.

Konovalov, D. A. (1970). On the structure of Thermals. *OSTIV Publication XI*.

Laiti, L. (2013). *An investigation of the Ora del Garda wind by means of airborne and surface measurements*. PhD thesis, Department of Civil, Environmental and Mechanical Engineering, University of Trento.

Laiti, L., Zardi, D., de Franceschi, M., and Rampanelli, G. (2013). Residual kriging analysis of airborne measurements: application to the mapping of atmospheric boundary-layer thermal structures in a mountain valley. *Atmospheric Science Letters*, 14(2):79–85. doi:10.1002/asl2.420.

Lenschow, D. H. and Stephens, P. L. (1980). The Role of Thermals in the Convective Boundary Layer. *Boundary-Layer Meteorology*, 19(4):509–532. doi:10.1007/BF00122351.

Liu, B., Duan, X., and Yan, L. (2018). A Novel Bayesian Method for Calculating Circular Error Probability with Systematic-Biased Prior Information. *Mathematical Problems in Engineering*, 2018. doi:10.1155/2018/5930109.

Manton, M. J. (1977). On the structure of convection. *Boundary-Layer Meteorology*, 12:491–503. doi:10.1007/BF00123194.

Metzger, S., Junkermann, W., Butterbach-Bahl, K., Schmid, H. P., and Foken, T. (2011). Corrigendum to "Measuring the 3-D wind vector with a weight-shift microlight aircraft" published in Atmos. Meas. Tech., 4, 1421–1444, 2011. *Atmospheric Measurement Techniques*, 4(7):1515–1539. doi:10.5194/amt-4-1515-2011.

Oke, T. (1987). *Boundary Layer Climates*. Routledge, London.

Oney, S. and Aslan, Z. (1987). Theoretical investigations and measurements of thermals. Presented at the XX OSTIV Congress, Benalla, Australia.

Raymond, E. S. (2021). NMEA Revealed. `https://gpsd.gitlab.io/gpsd/NMEA.html`. Accessed: 16-04-2021.

Saha, S., Moorthi, S., Wu, X., Wang, J., Nadiga, S., Tripp, P., Behringer, D., Hou, Y., Chuang, H., Iredell, M., Ek, M., Meng, J., Yang, R., Mendez, M. P., van den Dool, H., Zhang, Q., Wang, W., Chen, M., and Becker, E. (2014). The NCEP Climate Forecast System Version 2. *Journal of Climate*, 27(6):2185–2208. doi:10.1175/JCLI-D-12-00823.1.

Schumann, U. (1990). Large-eddy simulation of the up-slope boundary layer. *Quarterly Journal of the Royal Meteorological Society*, 116(493):637–670. doi:10.1002/qj.49711649307.

Scorer, R. S. (1957). Experiments on convection of isolated masses of buoyant fluid. *Journal of Fluid Mechanics*, 2(6):583–594. doi:10.1017/S0022112057000397.

Serafin, S. and Zardi, D. (2010). Structure of the Atmospheric Boundary Layer in the Vicinity of a Developing Upslope Flow System: A Numerical Model Study . *Journal of the Atmospheric Sciences*, 67(4):1171–1185. doi:10.1175/2009JAS3231.1.

Sigrist, B. (2006). Use of Topographic Elevation Models to Identify Thermal Hotspots in Alpine Areas. *Technical Soaring*, 30(3):53–60.

Smolarkiewicz, P. and Clark, T. (1985). Numerical Simulation of the Evolution of a Three-Dimensional Field of Cumulus Clouds. Part I: Model Description, Comparison with Observations and Sensitivity Studies. *Journal of the Atmospheric Sciences*, 42(5):502–521. doi:10.1175/1520-0469(1985)042<0502:NSOTEO>2.0.CO;2.

Specht, C., Pawelski, J., Smolarek, L., Specht, M., and Dabrowski, P. (2019). Assessment of the Positioning Accuracy of DGPS and EGNOS Systems in the Bay of Gdansk using Maritime Dynamic Measurements. *The Journal of Navigation*, 72(3):575–587. doi:10.1017/S0373463318000838.

Stull, R. B. (1973). Inversion rise model based on penetrative convection. *Journal of Fluid Mechanics*, 30:1092–1099.

Stull, R. B. (1988). *An Introduction to Boundary Layer Meteorology*. Kluwer Academic Publishers.

Taconet, O. and Weill, A. (1983). Convective plumes in the atmospheric boundary layer as observed with an acoustic Doppler sodar. *Boundary-Layer Meteorology*, 25:143–158. doi:10.1007/BF00123971.

Teppa, G. (2012). *Parapendio.* Mulatero Editore.

Turner, J. S. (1973). *Buoyancy Effects in Fluids.* Cambridge University Press, London.

Ultsch, A. (2012). Swarm Data Mining for the Fine Structure of Thermals. *Technical Soaring*, 36(4):37–44.

van den Kroonenberg, A., Martin, T., Buschmann, M., Bange, J., and Vörsmann, P. (2008). Measuring the Wind Vector Using the Autonomous Mini Aerial Vehicle M^2AV. *Journal of Atmospheric and Oceanic Technology*, 25(11):1969–1982. doi:10.1175/2008JTECHA1114.1.

von Kaenel, M., Sommer, P., and Wattenhofer, R. (2011). Ikarus: Large-Scale Participatory Sensing at High Altitudes. *HotMobile '11: Proceedings of the 12th Workshop on Mobile Computing Systems and Applications*, pages 63–68. doi:10.1145/2184489.2184503.

Waibel, G. (2013). Modeling Thermals. *Technical Soaring*, 37(4):58–60.

Warner, J. and Telford, J. W. (1967). Convection Below Cloud Base. *Journal of the Atmospheric Sciences*, 24(4):374–382. doi:10.1175/1520-0469(1967)024<0374:CBCB>2.0.CO;2.

Wilczak, J. M. and Tillman, J. E. (1980). The Three-Dimensional Structure of Convection in the Atmospheric Surface Layer . *Journal of the Atmospheric Sciences*, 37(11):2424–2443. doi:10.1175/1520-0469(1980)037<2424:TTDSOC>2.0.CO;2.

Williams, A. G. and Hacker, J. M. (1992). Inside Thermals. *Technical Soaring*, 16(2):57.

Woodcock, A. H. (1940). Convection and Soaring Over the Open Sea. *Journal of Marine Research*, 3:248–253.

Woodcock, A. H. (1975). Thermals over the sea and gull flight behavior. *Boundary-Layer Meteorology*, 9:63–68. doi:10.1007/BF00232254.

Young, G. S. (1988). Convection in the atmospheric boundary layer. *Earth-Science Reviews*, 25(3):179–198. doi:10.1016/0012-8252(88)90020-7.